DNA block copolymers –
from micelles to machines

Dissertation

zur Erlangung des Grades

"Doktor der Naturwissenschaften"

am Fachbereich Chemie, Pharmazie und Geowissenschaften

der Johannes Gutenberg-Universität Mainz

Jie Wang

geb. am 25.04.1982

in Jiangxi (V. R. China)

Mainz – 2008

Abstract

DNA block copolymer, a new class of hybrid material composed of a synthetic polymer and an oligodeoxynucleotide segment, owns unique properties which can not be achieved by only one of the two polymers. Among amphiphilic DNA block copolymers, DNA-*b*-polypropylene oxide (PPO) was chosen as a model system, because PPO is biocompatible and has a $T_g < 0$ °C. Both properties might be essential for future applications in living systems. During my PhD study, I focused on the properties and the structures of DNA-*b*-PPO molecules.

First, DNA-*b*-PPO micelles were studied by scanning force microscopy (SFM) and fluorescence correlation spectroscopy (FCS). In order to control the size of micelles without re-synthesis, micelles were incubated with template-independent DNA polymerase TdT and deoxynucleotide triphosphates in reaction buffer solution. By carrying out ex-situ experiments, the growth of micelles was visualized by imaging in liquid with AFM. Complementary measurements with FCS and polyacrylamide gel electrophoresis (PAGE) confirmed the increase in size. Furthermore, the growing process was studied with AFM in-situ at 37 °C. Hereby the growth of individual micelles could be observed. In contrast to ex-situ reactions, the growth of micelles adsorbed on mica surface for in-situ experiments terminated about one hour after the reaction was initiated. Two reasons were identified for the termination: (i) block of catalytic sites by interaction with the substrate and (ii) reduced exchange of molecules between micelles and the liquid environment. In addition, a geometrical model for AFM imaging was developed which allowed deriving the average number of mononucleotides added to DNA-*b*-PPO molecules in dependence on the enzymatic reaction time (chapter 3).

Second, a prototype of a macroscopic DNA machine made of DNA-*b*-PPO was investigated. As DNA-*b*-PPO molecules were amphiphilic, they could form a monolayer at the air-water interface. Using a Langmuir film balance, the energy released owing to DNA hybridization was converted into macroscopic movements of the barriers in the Langmuir trough. A specially adapted Langmuir trough was build to exchange the subphase without changing the water level significantly. Upon exchanging the subphase with complementary DNA containing buffer solution, an increase of lateral pressure was observed which could be attributed to hybridization of single stranded DNA-*b*-PPO. The pressure versus area/molecule isotherms were recorded before and after hybridization. I also carried out a series of control experiments, in order to identify the best conditions of realizing a DNA machine with DNA-*b*-PPO. To relate the lateral pressure with molecular structures, Langmuir Blodgett (LB) films were transferred to highly ordered pyrolytic graphite (HOPG) and mica substrates at different pressures. These films were then investigated with AFM (chapter 4).

At last, this thesis includes studies of DNA and DNA block copolymer assemblies with AFM, which were performed in cooperation with different group of the Sonderforschungsbereich 625 "From Single Molecules to Nanoscopically Structured Materials". AFM was proven to be an important method to confirm the formation of multiblock copolymers and DNA networks (chapter 5).

List of abbreviations

A	adenine
AFM	atomic force microscopy
bp	base pair
C	cytosine
CMC	critical micelle concentration
comDNA	complementary DNA
DNA	deoxyribonucleic acid
dNTP	deoxynucleotide triphosphate
ds	double stranded
FCS	fluorescence correlation spectroscopy
FCCS	fluorescence cross correlation spectroscopy
G	guanine
HOPG	highly oriented pyrolytic graphite
HPLG	high performance liquid chromatography
LB	Langmuir Blodgett technique
Mw	molecular weight
noncomDNA	noncomplementary DNA
ODN	oligodeoxynucleotide
PAGE	polyacrylamide gel electrophoresis
PCR	polymerase chain reaction
PEG	polyethylene glycol
PPO	polypropylene oxide
SPM	scanning probe microscopy
ss	single stranded
T	thymine
TdT	terminal deoxynucleotidyl transferase

| Tris | tris(hydroxymethyl)aminomethane |
| U | unit |

Table of contents

Chapter 1

Introduction and motivation

Recently, polymer chemistry and molecular biology have converged to create a new type of hybrid material which is made of oligodeoxynucleotides and synthetic polymers. As a combination of two classes of materials in a covalent fashion, DNA block copolymers (DBCs) could exhibit unique properties which can not be achieved by merely the DNA segment or the synthetic polymer segment. For example, DNA-*b*-poly(D,L-lactic-co-glycolic acid) (PLGA) has been used to enhance the cellular uptake in antisense oligonucleotides delivery system by forming micellar aggregates[1, 2]. Due to the biodegradable nature of the organic polymer, these micelles could release the antisense oligonucleotides in a controlled manner. DNA-*b*-poly(N-isopropylacrylamide) (PNIPAM) has been used to purify biomacromolecules with the help of reversible temperature-responsive behaviour of PNIPAM.[3] In such DBCs, the DNA segment was capable of recognizing a sequence of plasmid DNA by triple helix formation, and the complex could be precipitated and separated from the impurities employing small temperature increases above the lower critical solution temperature of PNIPAM.

Besides the applications in the fields of biology and biotechnology, DBCs have also potential applications in the field of nanoscience. Amphiphilic DBCs could form nanoparticles containing a hydrophobic polymeric core and a DNA corona in selective solvents. For example, by tailoring the lengths of the oligonucleotides and molecular weight of polystyrene (PS), the diameters of the DNA-*b*- PS micelles could be adjusted ranging from 8-30 nm.[4] These block copolymer micelles were used to build up sequence specific aggregates with DNA modified gold nanoparticles through DNA hybridization, and these aggregates could be reversibly dissembled by heating

them above the melting temperature of the double stranded DNA.

In order to overcome the hindrance in dissolution of amphiphilc DBCs containing a hydrophobic block with high glass transition temperature (T_g), DNA-*b*- polypropylene oxide (PPO) was synthesized in which the synthetic polymer block had a low T_g (-70 ℃).[5, 6] Micelle aggregations of DNA-*b*-PPO could be easily prepared by just dissolving the DBCs in an aqueous medium. The organic PPO segment has also been proven to be biocompatible with different cell types, which might be of importance in future applications in living systems.[7] The spherical micelles formed by DNA-*b*-PPO were characterized by atomic force microscopy (AFM) in aqueous solution and dynamic light scattering above the critical micelle concentration (cmc) of 5 ng/mL. These nanoparticles were introduced as a novel three-dimensional template for DNA-templated synthesis. They have also been used as highly modular system for chemotherapeutic drug delivery.[8]

So far, the structural properties of DBCs micelles have been changed by tailoring the length of DNA and molecular weight of synthetic polymer, as well as hybridization of complementary sequences. In the above cases, the switching of the morphologies could not been observed in-situ, and DNA segments with different length or DNA templates were required for the alteration. The challenge of **controlling the size of DBC nanoparitcles by enzymatic reaction** attracted our interest.

Terminal deoxynucleotidyl transferase (TdT) is an enzyme which belongs to the family of polymerases called pol X, and is responsible for the generation of the random genetic information that is essential for the efficacious function of the vertebrate adaptive immune system.[9, 10] TdT catalyzes the repetitive addition of deoxyribonucleotides to the 3' hydroxyl ends of DNA in a template-independent manner,[11] elongating the initiator chain and releasing inorganic pyrophosphate.

Nanoparticles formed by DNA-*b*-PPO could be good candidates for increasing the

size by TdT, because the organic polymer was attached to the 5' end and the block copolymers possed free 3'-OH groups. The **increase of the sizes of micelles could be observed after different incubation time by AFM ex-situ** (chapter 3.2). Fluorescence correlation spectroscopy (FCS) and polyacrylamide gel electrophoresis (PAGE) was also used to assess the increase of sizes of micelles (chapter 3.2).[12]

Apart from ex-situ measurements, atomic force microscopy would also enable in-situ observation of enzymatic growth. As reported, AFM allows the direct visualization of DNA molecules, their conformation, interaction and assembly in near-physiological environments,[13, 14] as well as the investigation of single-molecular mechanics.[15] Single enzyme molecules and enzymatic activities have been observed.[16-18] For example, Ellis et al. observed DNA translocation and cleavage by the EcoKI endonuclease using atomic force microscopy (Fig. 1.1). At the beginning, DNA contracted from 0'00" to 3'34" through translocation. The progressive disappearance of the DNA loop was indicated by the large arrow. At 7'08", cleaved DNA began to appear as shown by small arrowheads. Cleavage was continuously observed from 7'08" to 10'42". At 14'43", DNA fragments were found to be migrated away from the EcoKI complex. During this period, EcoKI (the highest structure in the images) remained almost stationary. Inspired by this ability of AFM, we wondered if it was possible to **follow the growth of DNA-*b*-PPO micelles in-situ with AFM** (chapter 3.3), and if we could **trigger the enzymatic reaction by temperature or by adding mononucleotides** (chapter 3.3.1 and 3.3.2).[19]
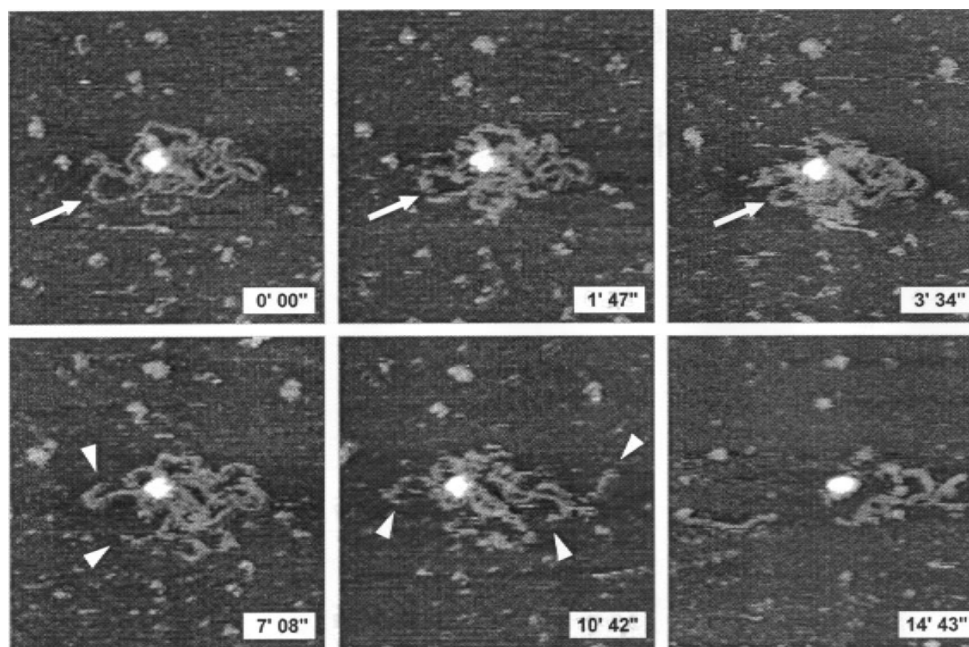
Figure 1.1 *Translocation and cleavage of pRH3 plasmid DNA by EcoKI enzyme. The sample was prepared in the absence of ATP, and a plasmid with bound EcoKI was identified by AFM. While the tip was still engaged, ATP (100 mM) was gently added to the imaging buffer, and successive images were captured. Scan size: 720 nm. Height scale (dark–light): 0–15 nm.*[18]

Another special feature of DNA that is important for DBCs is the hybridization of complementary sequences leading to the formation of a helical, semiflexible double stranded (ds) polymer. The average free-energy change associated with the hybridization of a complementary base pair is -78 meV (-1.8 kcal mol^{-1}) at 20 °C.[20] Apart from altering the molecular morphologies, can we transfer this energy to drive a macroscopic object? In other words, can we **build a DNA machine based on the hybridization of DBCs and complementary sequences** (chapter 4.2.3)?

Since the beginning of this millennium, the progress in this area, from DNA tweezers,[21, 22] rotary DNA device,[23] to DNA walkers,[24-28] has attracted great attention. In 2000, Yurke et al. reported the construction of a DNA-fuelled molecular machine. The machine, made from three strands of DNA, has the form of a pair of tweezers. It

may be closed and opened by addition of complementary strands of "fuel" DNA (Fig. 1.2)[21]. Hybridization between the closing and removal fuel strands is expected to occur first at the exposed overhang and to proceed by branch migration, a random walk of the junction between the region of F newly hybridized to the removal stand and the region still hybridized to the tweezer. Dye quenching is used to titrate the closing and removal strands and to determine the state of the machine. The DNA machines can be repeatedly closed and opened by successively adding fuel and removal strands to the solution.
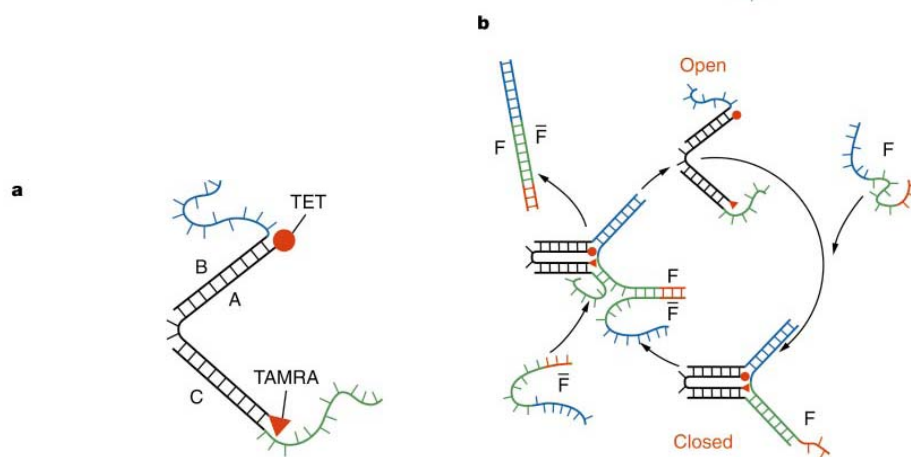
Figure 1.2 *Construction and operation of the molecular tweezers. (a) Molecular tweezer structure formed by hybridization of oligonucleotide strands* A*,* B *and* C*. (b) Closing and opening the molecular tweezers. Closing strand* F *hybridizes with the dangling ends of strands* B *and* C *(shown in blue and green) to pull the tweezers closed. Hybridization with the overhang section of* F *(red) allows* F̄ *strand to remove F from the tweezers forming a double-stranded waste product and allowing the tweezers to open.[21]*

The above mentioned DNA machines were fabricated in solution and authors motivated their work by powering devices like nanorobots and nanomechanical computers. They are not designed to drive macroscopic objects.

As DNA-*b*-PPO molecules are amphiphilic, they might form a monomolecular layer

at the air-water interface and could be controlled by a Langmuir film balance. If the hybridization of DNA-*b*-PPO with complementary sequences could induce a change in surface pressure, the barriers might be moved (Fig. 1.3). In this way, the energy released during the process of hybridization can be converted to a macroscopic mechanical motion.
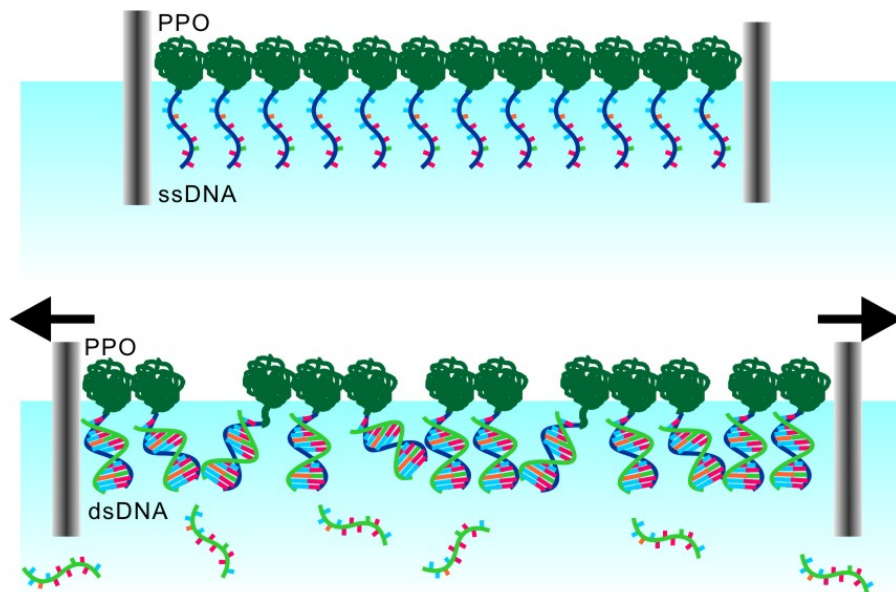
Figure 1.3 *Cartoon of the setup of a Langmuir film balance for in-situ hybridization and the principle of a DNA machine based on hybridization.*

Over the last two decades, researchers have used Langmuir film balance to study biological species and fabricate monolayers and multilayers with the Langmuir Blodgett technique for a wide range of purposes, owing to the special properties of air-water interface and well-controlled deposition to solid substrates. In the case of DNA, as it was negatively charged, it could form complexes with charged cationic lipid-like monolayer at the air-water interface (Fig. 1.4), while the conformation of DNA in the monolayer was still under debate.[29-32]
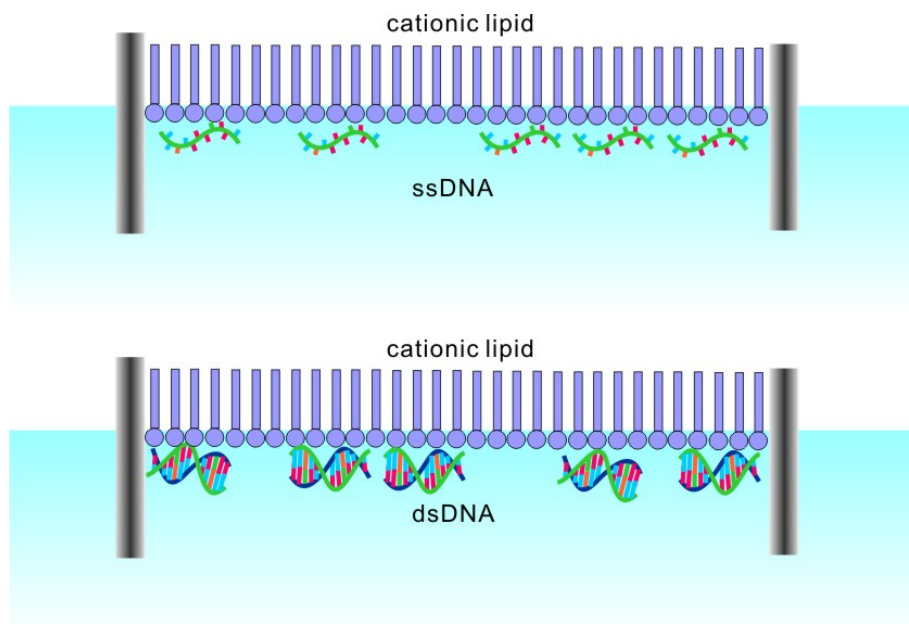
Figure 1.4 *Model of the cationic lipid-ssDNA and cationic lipid-dsDNA complex monolayers at the air-water interface.*

With amphiphilic DNA-*b*-PPO molecules, a monolayer containing DNA could be directly deposited on the air-water interface without coupling with charged lipids. The density of DNA in the monolayer could be well controlled, and ssDNA segments remained in the native conformation, which made in-situ hybridization possible. Apart from being a nice prototype of a DNA machine, DNA-*b*-PPO was a novel type of monolayer forming material and could **form thin films on solid substrates by Langmuir Blodgett (LB) technique** (chapter 4.3). These thin films might have potential application for biosensors, DNA chips or bioactive interfaces.

Chapter 2

Methods and materials

2.1 Atomic force microscopy

2.1.1 Theory and instrument

After the development of optical microscope in 17th century and the breakthrough in the world of microscopy, the development of scanning electron microscope in the 1930s, a very different type of microscope, the scanning tunnelling microscope (STM), was created at IBM's research centre in Zurich by Binnig, Rohrer, Gerber and Weibel.[33] The principle behind the STM is that the electrons are capable of tunnelling between two conductors provided they are in sufficiently close proximity, which limits the application in nonconductive biological samples. In 1986, the atomic force microscopy (AFM) was invented by Binnig, Quate and Gerber.[34] It has no requirments for a conducting sample thus openning possibilities in new fields such as polymer and biological sciences. The AFM images are a result of a multitude of forces interacting between the tip and the sample, e.g., van der Waals and electrostatic forces. AFM is now one of the foremost tools for imaging topography of solid surfaces and manipulating matter at the nanoscale. It has the advantages such as, providing three dimentional surface profile at high resolution, working in both ambient and liquid environments, requiring no special treatment that would destroy the sample or prevent reuse.

In the AFM (Fig. 2.1) the sample surface is scanned by a tip, which is integrated into a cantilever spring. The cantilever and tip are often made out of silicon or silicon nitride. The back face of the cantilever is usually coated with a metallic thin film, e.g., gold and aluminum, to enhance reflectivity. While scanning, the tip is brought into close proximity of the sample surface and the force between the tip and the sample leads to a deflection of the cantilever according to Hooke's Law:

$$F = -kx \qquad\qquad (2.1)$$

in which F is the force, k is the spring constant (usually ranges from 0.01 to 1.0 N/m, resulting in forces ranging from nN to µN in an ambient atomsphere), and x is the cantilever deflection. Typically the sample is mounted on a piezoelectric scanner which can move precisely in x, y, and z directions, and the deflection is measured using a laser spot reflected from the top of the cantilever to the photodiode. As the force between the tip and the sample surface is a function of tip-sample separation, the signal of laser deflection can be translated to topographic information by the data processor. In order to avoid the risk of damaging surface features with the tip, feedback electronics can be employed to adjust the tip-sample distance to keep the tip-sample interaction constant. The vertical position of the piezoelectric scanner at each (x, y) point is stored to give the topographic image of the sample surface. This mode of operation is the so-called constant force mode. Both the constant force mode and constant height mode are classified as the contact mode.
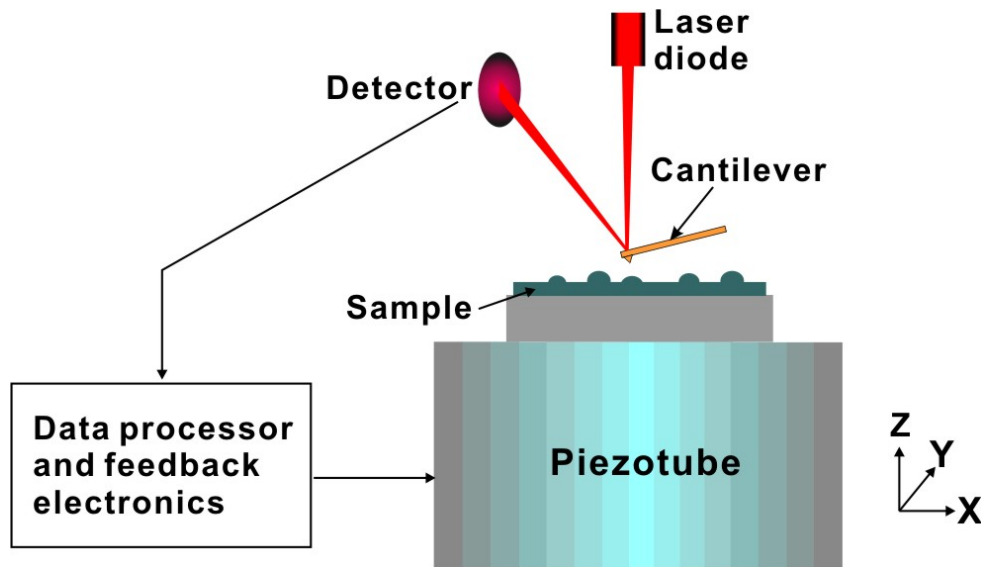
Figure 2.1 *Schematic illustration of how the AFM works.*

Another mode of operation often used to obtain tophograpic image is tapping mode. In tapping mode, the cantilever is oscillated at or near its resonance frequency with an amplitude typically ranging from 5 nm to 100 nm. During scanning the tip "taps" on the sample surface, and the force between the tip and the sample changes resonance frequency and oscillation amplitude. The feedback loop drives the piezoscanner to move vertically in order to keep constant oscillation amplitude, i.e., constant tip-sample interaction. Then the position of the scanner is plotted to give the surface topography, as in contact mode.

2.1.2 AFM imaging in liquid

A major advantage of the AFM is its ability to image specimens in aqueous environments. By imaging in liquid, the sample does not have to be dried. In addition, some soluble impurities, for example, salts in buffer solution, would not crystallize and therefore influence the original morphology.

There are two classical approaches: the easiest way is simply placing a drop of the relevant solution on the sample. It requires no special sample containers, only a tip holder that is suitable for operating in liquids. Alternatively, liquid cells provide a closed system reducing evaporation for imaging in liquid. They also make it possible to exchange the liquid during imaging. A liquid cell consists of a glass assembly with a wire clip for holding a cantilever. It has also an inlet and an outlet for injecting liquid and exchange of liquid. The volume of the liquid in the cell is usually 30-50 μL.
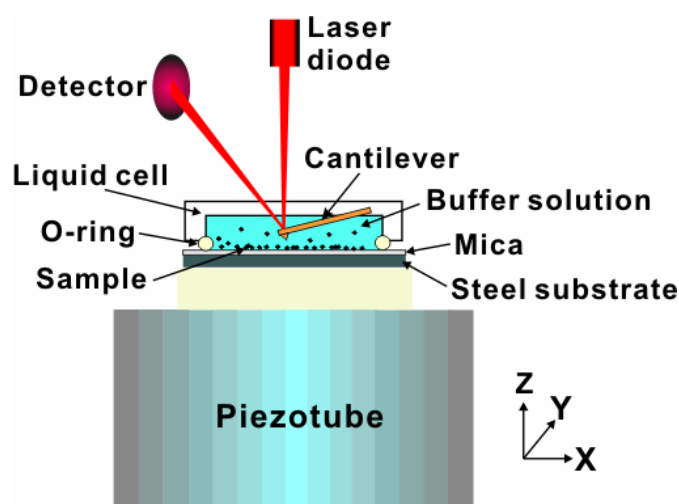
Figure 2.2 *Cartoon of the setup for AFM imaging with a liquid cell. The cantilever is fixed on the bottom of a quartz liquid cell. The liquid cell is sealed by an O ring on the mica substrate which is glued onto a steel substrate.*

In addition to imaging in liquid, many AFM systems make it possible to operate at a temperature above room temperature. This is particularly useful for in-situ observation of biological processes at a resolution unattainable by other techniques. In our temperature-controlled experiments, I used a piezoelectric J-scanner (Veeco Instruments, California), which was equipped with a thermal application controller (Veeco Instruments, California). Basically, the temperature setup consists of a resistor placed between the scanner and the sample that transmits the heat to the sample from

underneath. The temperature can be increased to 250 °C at a rate of 1.6 °C/min with a resolution of 0.1 °C. The piezo is always kept under its Curie temperature by a cooler fluid circuit. The applied temperature is the temperature that the thermal application controller displays. As the distance between the heating element and the sample itself (inside the droplet) is typically some millimetres, and there is a temperature gradient between the displayed and the real temperature, I used a thermocouple to calibrate the temperature in the droplet.

2.1.3 Image interpretation

There are four primary sources which might influence the resolution and accuracy of AFM images or even lead to artefacts: tips, scanners, imaging process, and vibrations.

Images measured with AFM are always a convolution of the tip geometry and the shape of the features being images. If the tip is much smaller than the features of the images being imaged, the tip-generated artifacts could be negligible. In the contrast, if the tip is blunt, the profile of the feature is broadened by the shape of the tip and the edges are smeared (Fig. 2.3). However, the height of the feature should still be correct.
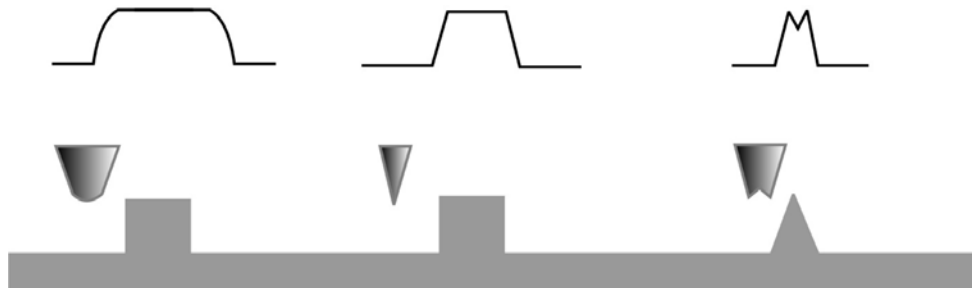

Figure 2.3 *Schematic illustration of tip convolution. The geometry of the tip determines the shape of the recorded prophile.*

Another problem can be encountered with the tip during scanning is the so called double tip, as shown in Fig. 2.4A. This kind of tip leads to features being repeated regularly over the image (Fig. 2.4B). This is a tip artefact and of course not the surface topography.
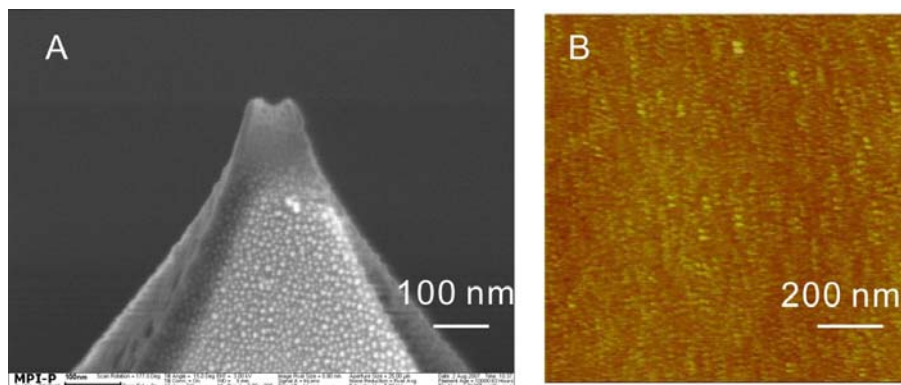
Figure 2.4 *Scanning electron microscopy (SEM) image of a double tip (A), and the AFM image of DNA-b-PPO micelles obtained by this double tip (B). The height scale of the AFM image is 30 nm.*

Scanner that moves the sample in the x, y, and z directions in AFM are typically made of piezoelectric materials. When a linear voltage ramp is applied to this piezoelectric material, it moves in a nonlinear motion. Before our measurements, the scanner was calibrated with different templates.

2.1.4 Sample preparation and experimental details for AFM imaging in liquid

For imaging in liquid, the DNA block copolymer samples should be attached to the surface. As DNA is negatively charged, transition metal cations such as Ni^{2+}, Co^{2+}, and Zn^{2+} have been found to bind DNA to negatively charged mica effectively.[35] I prepared the samples and carried out imaging in liquid with AFM as follows.

Twenty microliters of the sample solution in imaging buffer (10 mM Tris PH 7.4, 1 mM NiCl$_2$) were deposited onto freshly cleaved mica (Plano GmbH, Germany). After 5 min incubation the samples were rinsed with 200 µl of buffer solution. The mica sheet was then mounted in the AFM keeping the surface always covered by buffer solution.

AFM images were recorded using a commercial AFM (Multimode, Nanoscope IIIa, Veeco Instruments, California USA) in soft tapping mode in liquid. Oxide-sharpened silicon nitride cantilevers (NP-S, Veeco Instruments, California; 115 µm long, 17 µm wide, 0.6 µnm thick) with an integrated tip (a spring constant of 0.32 N/m and a resonance frequency of 56 kHz in air) were used. The height of the tip was 2.5 to 3.5 µm. The tip radius was confirmed by scanning electron microscopy after having performed the AFM measurements. I found tip radii of curvatures < 20 nm in all cases. A piezoelectric E-scanner (Veeco Instruments, California) was used, which supplies a maximum x-, y-scan of 12.5 µm and a z-extension of 2.5 µm. The scanner was calibrated by imaging a rectangular grid of 1 µm × 1 µm mesh size.

In liquids, I selected a driving frequency between 8 – 10 kHz and an amplitude setpoint around 0.4 V for imaging. AFM images (512 × 512 pixels) were recorded at a scan rate of 1 Hz. Without specific notification, AFM images were captured while ensuring all parameters were kept constant. Images were processed by flattening to remove the background slope. The maximum height of individual micelle was calculated by means of local roughness analysis.

2.2 Fluorescence correlation spectroscopy

2.2.1 Theory and instrument

Fluorescence correlation spectroscopy (FCS) was first introduced in 1972 by Magde, Elson, and Webb to measure the diffusion and binding of ethidium bromide onto double-stranded DNA.[36] This technique has been undergoing a renaissance since 1993 with the implementation of confocal microscopy FCS. Now, it has become a powerful single-molecule detection technique that measures and correlates fluctuations in fluorescence intensity within a very small detection volume.[37]

Fig. 2.5 A shows the basic setup of FCS. A laser beam is first expanded by two lenses, reflected by a dichroic mirror, and then focused by a high-numerical aperture objective lens onto a fluorescent sample. Fluorescent particles illuminated by the laser emit fluorescence. The fluorescence is collected by the same objective, filtered, focused by a tube lens, and passed through a confocal aperture onto the detector, typically an avalanche photodiode detector. A computer with a digital correlator card computes the autocorrelation function from the fluorescence intensity signal and stores the result.

The orange ellipse in Fig. 2.5 B represents the observation volume in FCS. Within this volume, the fluorescent molecules can be excited, and the emit fluorescence can be detected. The dashed curve shows how a sample particle diffuses through the observation volume. The movement of small particles in solution is a random process known as Brownian motion. The diffusing in and out of fluorescent particles results in a fluctuation of fluorescence signal. As an example, a typical fluorescence signal as a function of time is shown in Fig. 2.5 C. A pulse of this signal can be assumed to be resulted from the diffusion of the sample particle in Fig. 2.5 B. The pulse duration can be obtained by autocorrelation analysis (Fig. 2.5 D).
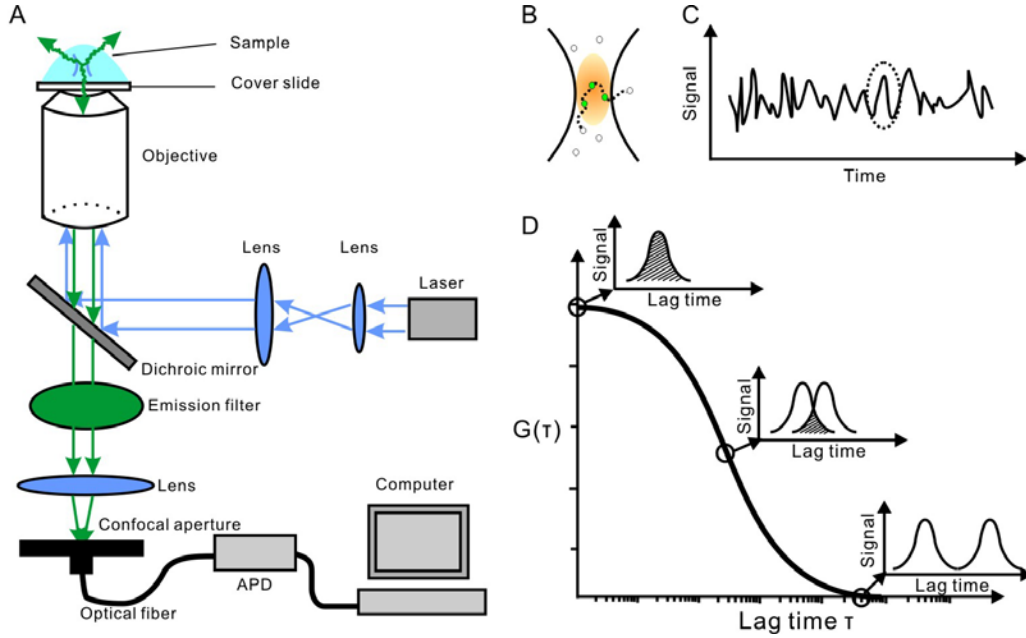
Figure 2.5 *Schematic illustration of the set up of a fluorescence correlation microscope and basic correlation principle.* (A) Experimental setup for FCS. (B) Magnified observation volume. (C) A typical fluorescence signal, as a function of time. (D) The signal *F(t)* at time *t* is correlated with itself at a later time *(t+τ)* to produce the autocorrelation *G(τ)*.

In order to illustrate the basic principle of data processing, the signal *F(t)* at time *t* is correlated with itself at a later time *(t+τ)* to produce the autocorrelation *G(τ)*. If there is no time-shift, both data traces are identical, and the correlation is high. If the shift is large, the two traces are different, and the correlation is low. Mathematically, the autocorrelation function is defined as:

$$G(\tau) = \frac{< F(t)F(t + \tau) >}{< F >^2} \qquad (2.2)$$

where *F(t)* is the fluorescence intensity at time *t*, *τ* is a time separation, and the angle brackets denote a time average.

$G(\tau)$ can be fitted to extract information about molecular concentration, diffusion, and chemical kinetics. For example, the rate of decay of the correlation over time, the so-called correlation time τ_D, describes the physical phenomenon, such as diffusion, that is causing the correlation. The longer the correlation persists, the slower the diffusion. Correlation persists longer for slowly diffusing particles and decays quickly for rapidly diffusing particles. Correlation time can be related to the diffusion coefficient D by the following relation:

$$\tau_D = \frac{\omega^2}{4D} \tag{2.3}$$

where ω is the radius of the confocal detection volume.

The diffusion coefficient D is then a function of the viscosity of the solvent, η, and the hydrodynamic radius of the particle, R_h, as described by the Einstein equation:

$$D = \frac{k_B T}{6\pi\eta R_h} \tag{2.4}$$

where k_B is the Boltzmann constant (1.38×10^{-23} J/K) and T is the temperature.

For nonspherical molecules equation 2.4 does not apply. If the molecule can be approximated as a rod or as an ellipsoid the diffusion coefficient can be calculated from[38, 39]

$$D_{rod} = \frac{k_B T}{3\pi\eta L}\ln(x + 0.312 + \frac{0.565}{x} + \frac{0.1}{x^2}) \tag{2.5}$$

where x is the ratio of the molecular length to its diameter.

2.2.2 Fluorescence cross correlation spectroscopy

Fluorescence cross correlation spectroscopy (FCCS) extends the ability of FCS in detecting molecular complexing.[40] It uses two species which are independently labeled with two spectrally separated fluorescent probes. These fluorescent probes are excited and detected by two different laser sources and detectors respectively (Fig. 2.6 A). These two laser beams are focused on the sample and overlap to have the same observation volume.

If these two species do not interact with each other, the movements of the targets are independent, and no cross-correlation of the two signals is observed. In contrast, if the two species could combine with each other (Fig. 2.6 B); the two signals are cross-correlated (Fig. 2.6 C and D). In analogy with autocorrelation, the fluorescence signals at two distinct wavelength bands (F_1 and F_2) are compared to determine whether the two signals are correlated (they fluctuate in concert) or not correlated (they fluctuate independently).

The normalized cross-correlation function is defined as follows:

$$G_{12}(\tau) = \frac{<F_1(t)F_2(t+\tau)>}{<F_1(t)><F_2(t)>} \tag{2.6}$$

where $F_1(t)$ at a specific time t, $F_2(t+\tau)$ at a delay time τ later is correlated with each other.
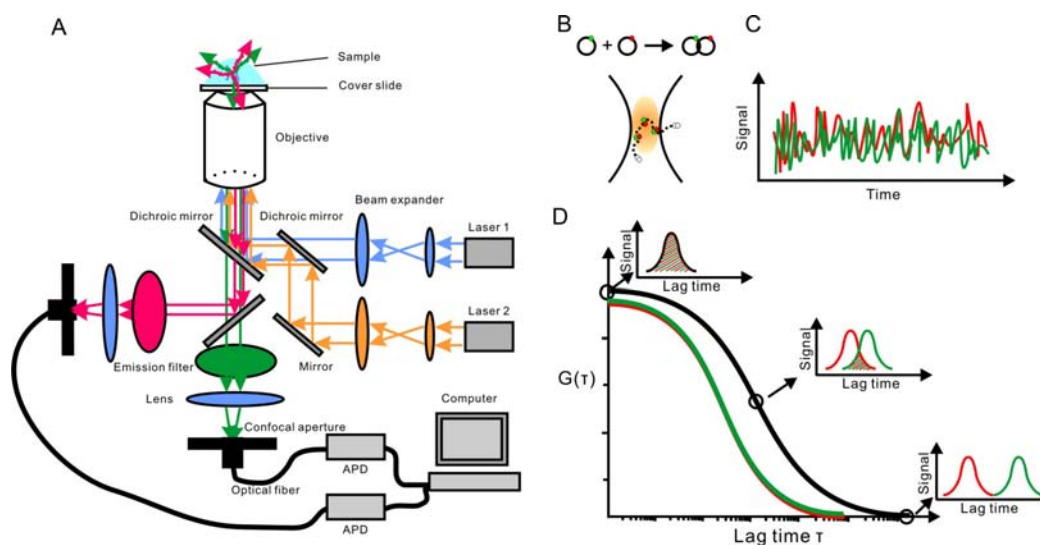
Figure 2.6 Schematic of how fluorescence cross correlation spectroscopy works.

2.2.3 Sample preparation and experimental details for FCS measurements

General hybridization procedure for fluorescent labelling:

The hybridization was carried out by dissolving ssDNA-*b*-PPO block copolymer and the complementary strand with the fluorophore (Alexa488, Invitrogen, USA) attached at the 5' end in TAE buffer (20 mM tris(hydroxymethyl)aminomethane-HCl, pH 8.0; 10 mM acetic acid, 0,5 mM EDTA) containing Na^+ (100 mM) and Mg^{2+} (60 mM). The mixture was heated to 95°C and was slowly cooled to room temperature over the course of 3 days (1 degree per hour) by using a Biometra polymerase chain reaction (PCR) thermocycler (Biometra GmbH, Germany). The final concentration of DNA was between 5-8 μM.

FCS was performed on a custom-built confocal microscope based on an Olympus IX71. An Argon ion laser (Spectra Physics) was used to excite the micelle solutions at 488 nm with 20 μW or 50 μW, respectively. In epi-fluorescence configuration,

diffraction-limited excitation and fluorescence collection was achieved through a water immersion objective (UPlanSapo 60xW, 1.2 n.a., Olympus, Hamburg). A 50 μm pinhole blocked the out-of-focus fluorescence. Fluorescence in the spectral range between 500 and 570 nm was separated from scattered light by an interference filter (HQ 532/70, AHF, Tübingen) and split in two channels by a polarizing beam splitter. The signals of the two single photon counting avalanche photodiodes (SPCM AQR-14, Perkin-Elmer) were fed into the autocorrelator card (ALV-5000/E, ALV, Langen) in cross-correlation configuration and in parallel to a set of synchronized, fast counter cards (SPC-152, Becker&Hickl, Berlin) for software-based autocorrelation.[41] A diluted Rhodamine-110 solution in pure water was used as the reference to yield the optical parameters of the confocal detection volume.

The addition of the nucleotides by TdT to the single stranded DNA of the preformed DNA-b-PPO micelles was monitored by FCS. For spherical micelles the diffusion time, τ_D, can be directly related to the hydrodynamic radius, R_h (equation 2.7):

$$R_h = kT(4\tau_D)/6\pi\eta\omega^2 \tag{2.7}$$

where k is the Boltzmann constant, T is the temperature, η is the viscosity of the solution, and ω is the approximated axial $1/e^2$ radius of the confocal volume.

Fitting the autocorrelation function of rhodamine 110 in water yielded the axial radius $\omega = 220$ nm of confocal volume using a diffusion coefficient $D = 2.8 \times 10^{-6}$ cm^2/s.[42] The corresponding effective hydrodynamic radius of 0.77 nm for rhodamine 110 is similar as reported previously.[43] Accordingly, the diffusion times of the micelles were used to calculate the respective radii.

2.3 Langmuir film balance

2.3.1 Theory and instrument

The history of Langmuir films starts with Benjamin Franklin, who in 1774 reported the "pour oil on water" phenomenon to the British Royal Society.[44] After about one century, Lord Rayleigh suspected that the maximum extension of an oil film on water represents a layer one molecule thick. At the same time, Agnes Pockles established the foundation of characterizing monolayers on an air-water interface by developing a rudimentary surface balance in her kitchen sink.[45, 46] Later, Irving Langmuir performed systematic studies on floating monolayers on water in the late 1910's and early 1920's,[47] and gained the Nobel Prize in 1932. Katherine Blodgett, who collaborated with Irving Langmuir, first described the details of sequential monolayer transferring to solid substrates.[48] These monolayer assemblies are therefore call as Langmuir-Blodgett (LB-) films, and the term "Langmuir film" is normally reserved for a floating monolayer.

The Langmuir films are usually formed by amphiphilic molecules consist of a hydrophilic part and a hydrophobic part. When amphiphilic molecules come in contact with water, they accumulate at the air-water interface causing a decrease in the surface tension of water, so that the free energy of the system can be reduced.
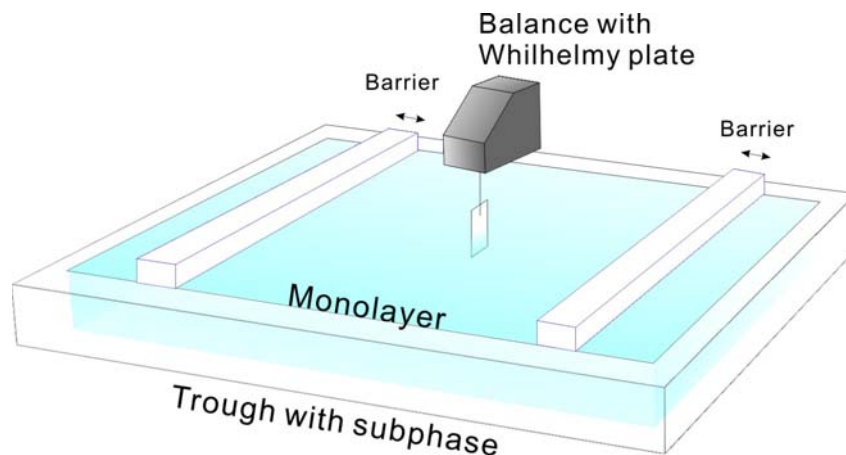
Figure 2.7 *Schematic illustration of a Langmuir film balance with a Wilhelmy plate electrobalance measuring the surface pressure, and barriers for reducing the available surface area.*

A modern version of a Langmuir trough consists of a temperature-controlled trough which contains the liquid (Fig. 2.7). The liquid is called "subphase". Usually the trough is made of Teflon and water is used as the subphase. The amphiphilic molecules are dissolved in a solvent (often chloroform) which is volatile and not miscible with the subphase. Drops of the solution are placed on the subphase surface and after evaporation of the solvent a monolayer of amphiphilic molecules remains. This process is called "spreading". Via movable barriers the Langmuir trough allows to manipulate the density of molecules on the liquid surface by compression or expansion of the film.

When the available area for the monolayer is large, the distance between adjacent molecules is large and their interactions are weak. The monolayer can then be regarded as a two-dimensional gas. Under these conditions the monolayer has little effect on the surface tension of water. If the available surface area of the monolayer is reduced by a barrier system to a certain extent, the molecules start to exert a repulsive effect on each other. This two-dimensional analogue of a pressure is called lateral pressure, and is defined by the following relationship:

$$\pi \equiv \gamma_0 - \gamma \tag{2.8}$$

where γ is the surface tension of the bare subphase and γ_0 is the surface tension of the subphase covered with the monolayer.

The lateral pressure can be measured by the Wilhelmy plate method, in which the force on a plate partially immersed in the subphase due to surface tension is measured.[44]
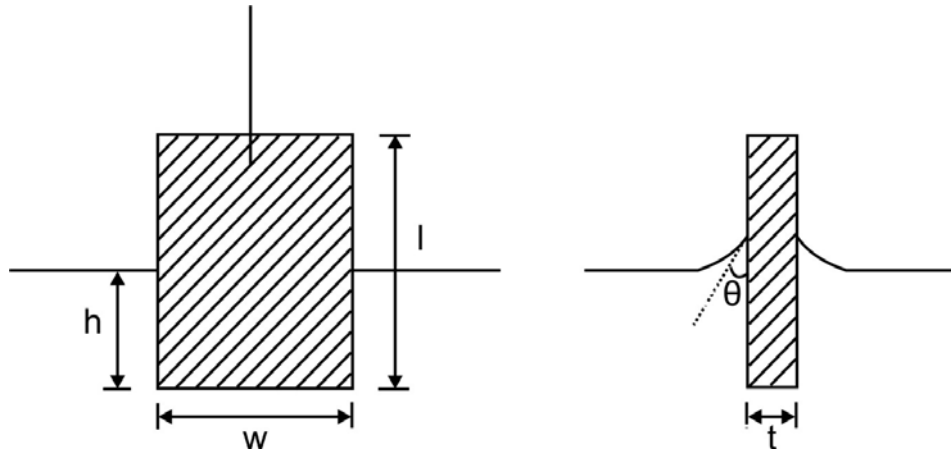

Figure 2.8 *A Wilhelmy plate immersed into the subphase.*

The forces acting on the plate are: the gravity and surface tension downward, and the buoyancy upward. If the rectangular plate has a density of ρ, and has a length of l, width of w and thickness of t, when it is immersed to a depth h in the subphase of density ρ_s, the net downward force is given by the following equation:

$$F = \rho glwt + 2\gamma(t + w)(\cos\theta) - \rho_s gtwh \tag{2.9}$$

where γ is the surface tension of the liquid, θ is the contact angle and g is the

gravitational constant.

As the lateral pressure is defined as the difference of surface tension between bare subphase and subphase covered by the monolayer, it can be determined by measuring the change in F. If the Wilhelmy plate hanging in the subphase is completely wetted (i.e. $\cos \theta = 1$, usually the plate is a piece of absorbent paper) and very thin, the lateral pressure can be calculated from the following equation:

$$\pi = -\Delta\gamma = -\left[\Delta F / 2(t + w)\right] = -F / 2w , \quad \text{if } w \gg t. \qquad (2.10)$$

Practically, the change in force is determined by measuring the changes in the mass of the plate, which is coupled to an electrobalance. By employing a computer controlled feedback system between the electrobalance and the motor responsible for the movements of the barriers, the monolayer can be held at a constant lateral pressure. In this way, LB films can be transferred to solid substrates at constant lateral presures.

Most commonly, researchers study the properties of a monolayer of amphiphilic molecules by measuring the lateral pressure as a function of the area per molecule. As the measurement is carried out at constant temperature, it is known as a pressure - area isotherm (π-versus-σ_A isotherm). By compressing the film at a constant rate while continuously monitoring the lateral pressure, an isotherm can be recorded. An ideal isotherm with all phases is shown in Fig. 2.9.[49]
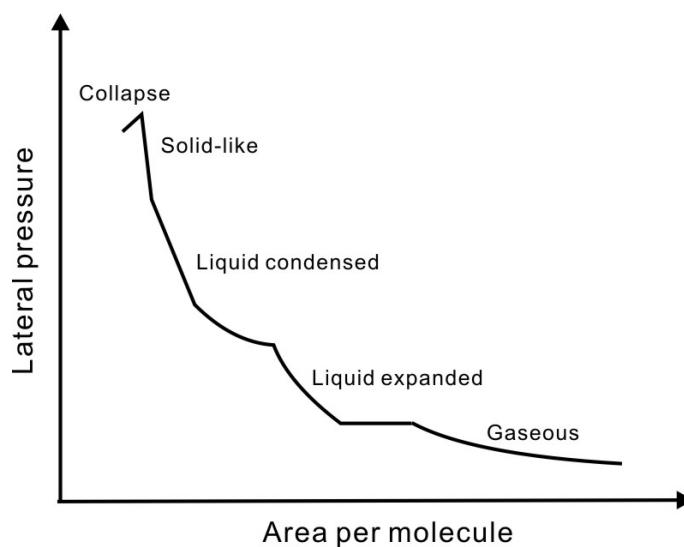
Figure 2.9 *Schematic graph of film pressure versus surface area per molecule. The indicated phases can occur, but most amphiphiles do not show all phases.*

The phases can be indicated as different regions in the isotherm. For very large molecular areas, films are in the gaseous state. The average area per molecule at the interface is much larger than the size of the molecule, and the film pressure is very low. Upon compression, the monolayer can undergo a phase transition to the liquid state, which is characterized by significant lateral interaction between the molecules. The liquid state can be composed of the liquid expanded and liquid condensed phases. For the liquid expanded phase, the molecules are touching each other, but there is no lateral order. For the liquid condensed phase, the molecules are tilted. The film is relative stiff, but there is still some water present between the headgroups. At even higher densities, the monolayer could reach the solid state, when the headgroups are highly dehydrated. As appeared in the isotherm, the curve is linear in the solid state. If the monolayer is further compressed after reaching the solid state, the monolayer will collapse into three-dimensional structures.

In addition to study monolayers, the Langmuir film balance can also be used to transfer amphiphilic molecules to substrates. It even makes the building up of highly

organised multilayers of amphiphilic molecules possible. These multilayer structures are usually called Langmuir-Blodgett (LB) films. They can be prepared by successively dipping a solid substrate through the monolayer and withdrawing it while the surface pressure is kept constant. In this way, the floating monolayer is adsorbed to the solid substrate. By varying the procedures of dipping, the properities of substrates, and the lateral pressure, formation of different LB films could be enabled. As an example, the deposition of LB films to a hydrophobic substrate is shown in Fig. 2.10.[49]
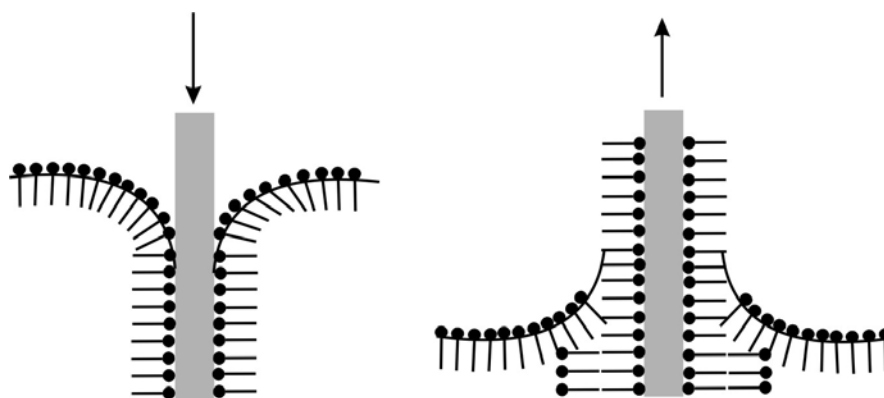

Figure 2.10 *The process of transferring Langmuir-Blodgett films to a hydrophobic substrate.*

2.3.2 Subphase exchange system

In order to carry out in-situ hybridization, I built a subphase exchange system, so that the subphase could be exchanged gradually and homogenously without significant change of the water level (Fig. 2. 11). With the help of this system, complementary DNA strands can be introduced to the subphase without disturbing the existing DNA-*b*-PPO monomolecular layer in the trough. It also allows studying the properties of the monomolecular layer in different subphases.
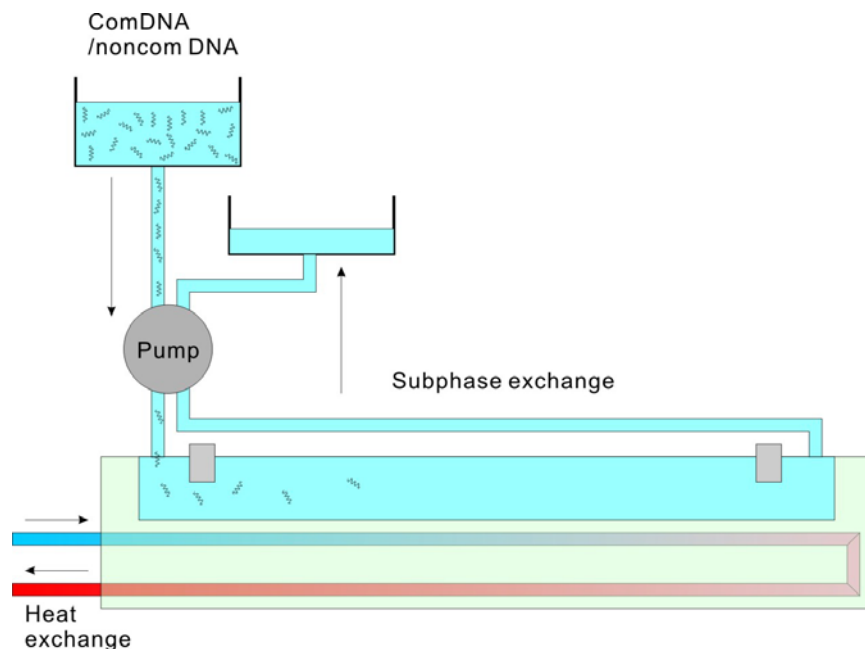
Figure 2.11 Schematic cartoon of the subphase exchange system coupled with a temperature controlled Langmuir trough.

On one side of the trough, there are three inlets for liquid. On the other side, there are three outlets. They are connected to an external peristaltic pump by tubes. The flowing in speed and the flowing out speed can be adjusted, so that the final volume of the flowing in liquid and flowing out liquid is equal, and thus the water level in the trough is constant. I tested the efficiency of the subphase exchange system by using $KMnO_4$ solution owing to its violet color (Fig. 2.12). The volume of the trough is 100 mL. It takes about 40 min to exchange the subphase. In the experiments, I run the exchange process for 45 min, and the volume of the exchanged liquid is 200 mL.
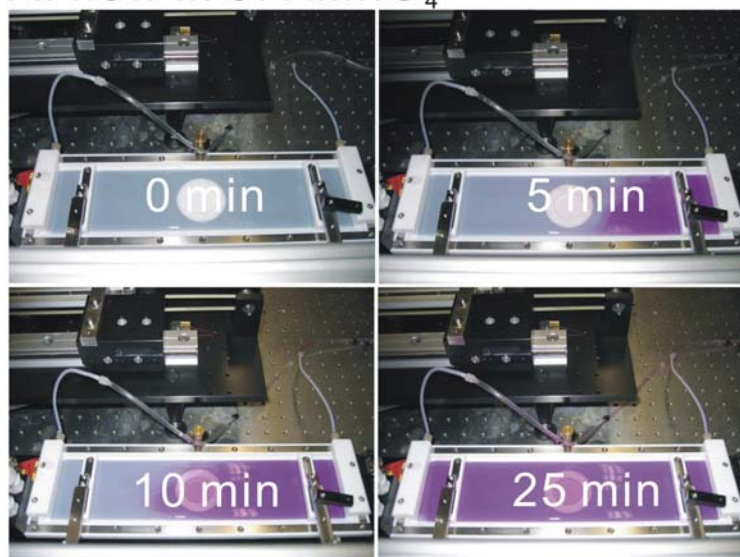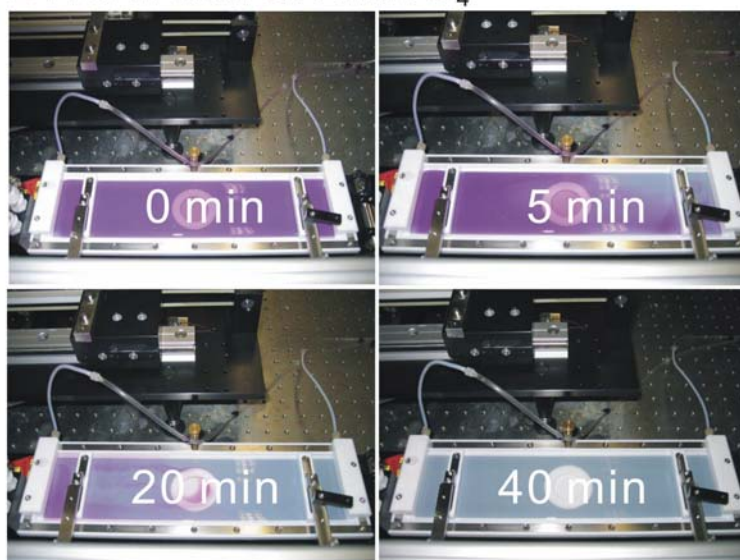
Figure 2.12 *Subphase exchange processes shown by KMnO₄ solution. (a) Flowing in process. (b) Flowing out process. This system was used for introducing complementary DNA strands into the subphase while DNA-b-PPO monolayer already existed on the interface.*

2.3.3 Materials and parameters used in Langmuir balance measurements

SsDNA(3'-TTCTATAGAAA)–*b*-polypropylene oxide (PPO) (Mw: 6800 g/mol) molecules were synthesized by Fikri E. Alemdaroglu and Minseok Kwak in Prof. Dr. Andreas Herrmann's group and used to form a monolayer in the Langmuir trough. 0.5 nmol DNA-*b*-PPO was dissolved in 2.5 mL dichloromethane (0.2 μM) for spreading on the interface and form a monolayer. The subphase was saline sodium citrate buffer (0.03 M sodium citrate, 0.3 M sodium chloride, pH~7.0, Sigma-Aldrich) for hybridization at 20 °C. The sequence of the complementary DNA (comDNA) was 5'-AAGATATCTTT, and the sequence of the noncomplementary DNA (noncomDNA) was 5'-TACACGTAGCA. They were purchased from Sigma-Aldrich and dissolved in saline sodium citrate buffer solution (2.5 μM) for subphase exchange. The volume of the exchanged subphase was 200 mL in total (500 nmol DNA strands inside).

Monolayer experiments were carried out in a rectangular Teflon trough (265 mm×68 mm) held at 20.0 °C. Isotherms were recorded 15 min after spreading of the solution for solvent evaporation. The compressing/expanding rate was 17.5 cm^2/min unless otherwise noted. The Wilhelmy system for measuring lateral pressure was calibrated with arachidic acid before all the measurements. A kink at a pressure of 25.6 mN/m should appear. If not, the pressure has to be calibrated in the following way. I set the "Soll" pressure to the kink and then stopped the barriers when the pressure came to the kink. I turned the calibration potentiometer with a screw-driver until the pressure showns 25.6 mN/m. The monolayer was expanded completely and compressed for a second time. I repeated above procedures until the kink showed up at 25.6 mN/m. Fig. 2.13 shows an example of the calibration curve of arachidic acid.
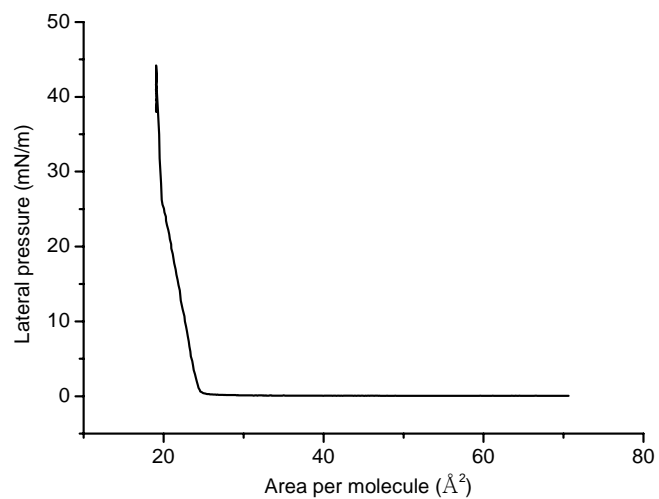
Figure 2.13 An isotherm of arachidic acid measured at 20 °C for the purpose of calibration.

2.4 Synthesis of DNA -*b*-PPO

DNA-*b*-PPO was synthesized in the group of Prof. Dr. Andreas Herrmann by Fikri E. Alemdaroglu and Minseok Kwak in MPIP Mainz in a single process using an Oligopilot DNA synthesizer (Amersham biosciences, Sweden).
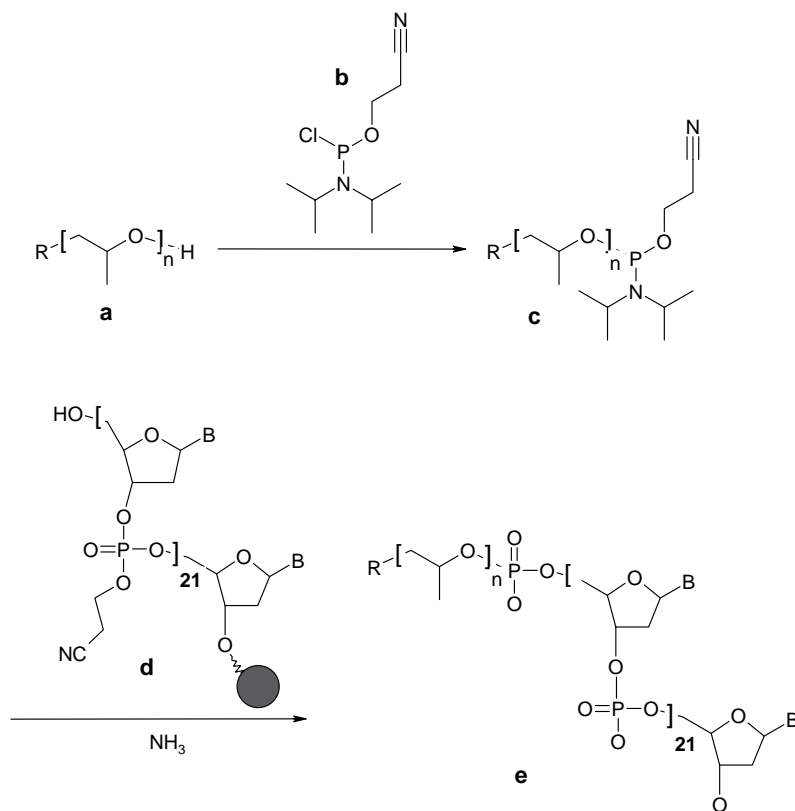
Figure 2.14 *Synthesis of ssDNA-b-PPO. a: hydroxy-group-terminated PPO. b: phosphoramidite chloride. c: phosphoramidite-PPO derivatives. d: the solid support and e: product of ss-DNA-b-PPO.*

The synthesis procedure of DNA-*b*-PPO is illustrated in Fig. 2.14.The synthesis starts with hydroxy-group-terminated PPOs (6800 g/mol) dissolving in dry THF. It was reacted with phosphoramidite chloride in the presence of diisopropylethylamine at room temperature under argon atmosphere for 3 h. Then the crude product was dried and dissolved in ethylacetate and extracted with Na_2CO_3 solution, water and brine. The solution was dried over $MgSO_4$. After evaporation of the solvent the phosphoramidite-PPO derivatives were dried under high vacuum. It was then dissolved in dry dichloromethane and attached to the 5' end of an ODN (22mer, 6670 g/mol, sequence: 5'-CCTCGCTCTGCTAATCCTGTTA-3', or 11mer, 3339 g/mol, sequence: 5'-AAAGATATCTT-3') on a solid support. Finally ssDNA-*b*-PPO was recycled through the solid support for 25 min to achieve high coupling efficiency. After that, phosphoramidite-PPO derivatives were liberated from the solid support

using concentrated ammonia for 16 h accompanied by deprotection of the bases. The solid support was removed by filtering and was then washed with ethanol/water mixture. After evaporation of the solvent the conjugate was purified, filtered and desalted.

Chapter 3

Enzymatic growth of DNA-*b*-PPO micelles

In 2005, Chow et al. studied the ability of TdT to catalyze the surface initiated polymerization of DNA.[50] Thereby, the height of self-assembled oligonucleotide monolayers on regular gold patterns was extended vertically. The height increase was confirmed by AFM and recorded in air after the reaction. The dimensions of the square surface pattern were gradually varied from 100 nm to 4 µm. It turned out that the vertical extension with DNA was dependent on the lateral feature size of the underlying gold patterns. The decrease in the vertical extension for smaller feature sizes was attributed to an increase in the conformational mobility of the DNA chains. It was assumed that this reduced the accessibility of TdT or mononucleotides to the 3' ends of the growing single stranded polynucleotides.

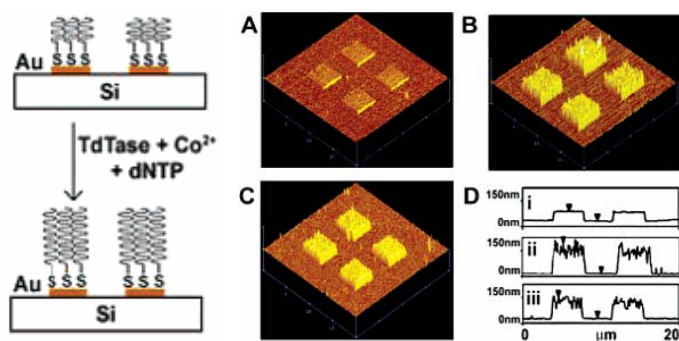**Figure 3.1** *Cartoon of surface-initiated growth of DNA by TdT from gold substrates that present a self assembled monolayer (SAM) of an oligonucleotide-terminated thiol and Tapping mode AFM images in air for the gold arrays with 5'-SH-(CH$_2$)$_6$-T$_{25}$ DNA-SAM, after treated with heat-inactivated TdTase (A), active TdT (B), and active TdT followed by exonuclease1 (C). The line profiles of these figures are shown in D (ref. 14).*

I hypothesized that the micelles formed by amphiphilic DBCs could serve as a substrate for TdT, and their size could be extended with the help of the enzyme. In this way, we could tailor diffusion properties, penetration properties, or reaction activities of the micelles, which might be crucial in future applications of these micelles.

For this purpose I used DNA-b-polypropylene oxide (PPO) which contained a nucleic acid unit consisting of 22 nucleotides (sequence: 5'-CCTCGCTCTGCTAATCCTGTTA-3', $M_w = 6670$ g/mol) and a synthetic polymer block with $M_w = 6800$ g/mol. This amphiphilic block copolymer possesses a free 3'-OH group, as the organic polymer unit is attached to the 5' end.

In order to get an idea of the size of single molecules and micelles first, FCS and FCCS measurements were carried out in cooperation with Dr. Kaloian Koynov in MPIP.

3.1 Size of single molecules and micelles

A solution containing ssDNA-b-PPO molecules at a concentration of 10 μM was prepared. Half of the solution was exposed to complementary DNA which were labeled with Alexa488 (**1**) dye. The other half was exposed to DNA labeled with Alexa633 (**2**) (Fig. 3.2). These two kinds of solutions were mixed and kept at 37°C for 48 hours. Thus, in case dsDNA-b-PPO molecules are exchanged between the micelles and their environment, micelles should exist which contain both type of dye molecules (**3**). The existence of micelles containing dsDNA-b-PPO having both types of dyes was detected by means of fluorescence cross correlation spectroscopy.
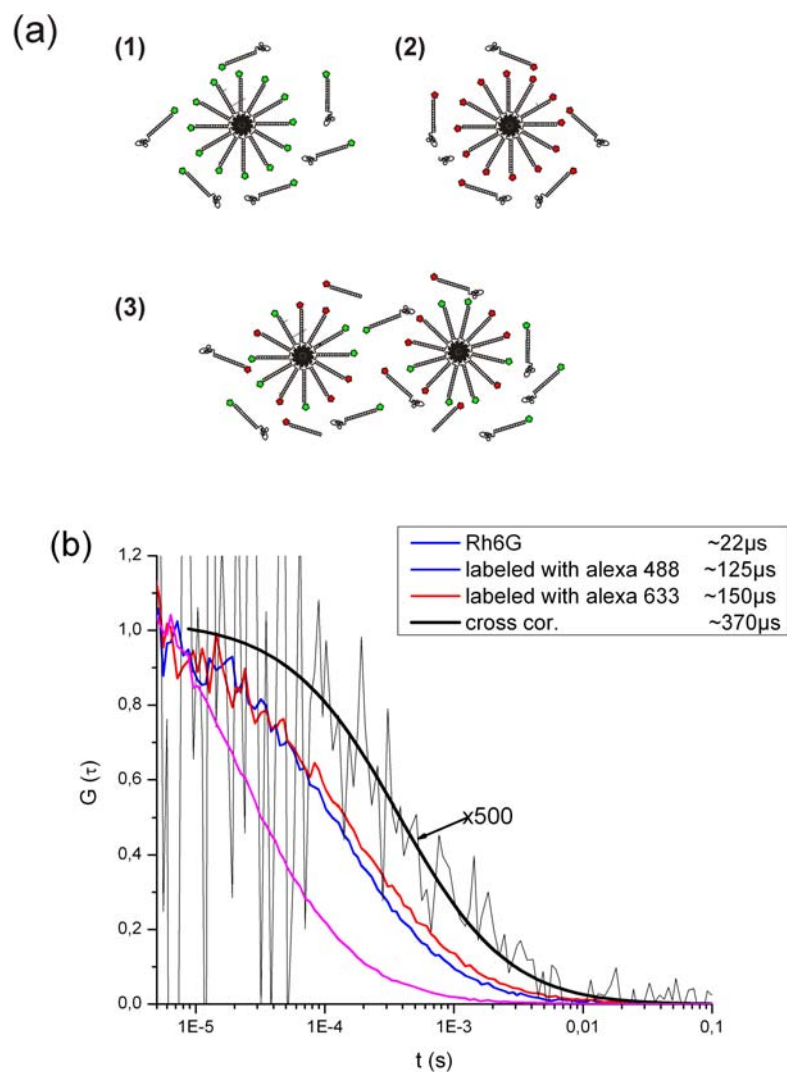
Figure 3.2 *The principle of the molecular exchange detected by FCS and results. (a) ssDNA-b-PPO micelles hybridized with complementary ssDNA labled with Alex 488 (1), ssDNA-b-PPO micelles hybridized with complementary ssDNA labled with Alex 633 (2), and a mixture of these two kinds of micelles. (b) Autocorrelation and cross correlation of two types of labels.*

FCS measurements were carried out with a 1:100 mixture of solution (**3**) and a solution of unlabeled dsDNA-*b*-PPO molecules having a concentration of 10 µM. This mixing resulted in a fluorescence labeled molar concentration appropriate for FCS.

We firstly obtained the autocorrelation from the FCS data recorded from the Alexa 633 dye (red line in Fig. 3.2 b). A diffusion time of t = 150 μs was determined. Then the autocorrelation from the FCS data recorded from the Alexa 488 dye (blue line in Fig. 3.2 b) was obtained. A diffusion time of t = 125 μs was determined which was a little bit lower compared to the measurement above owing to a smaller volume which is probed at this wavelength.

After hybridization with labeled complementary ssDNA, ssDNA-*b*-PPO became dsDNA-*b*-PPO and had a rod-like structure. The length of this molecule could also be predicted by the following equation

$$L = N_{bp} l_{bp} + 2R_{PPO}$$ (3.1)

where N_{bp} was the number of base pairs, l_{bp} was the length per base pair, and R_{PPO} was the gyration radius of PPO. l_{bp} was 0.33 nm for double stranded DNA,[51] and R_{ppo} for a molecular weight of 6800 g/mol was 2.0 nm,[52] so the length of dsDNA-*b*-PPO was 13.3 nm. The diameter of the dsDNA segment was 2.2~2.6 nm,[51] and the diameter of PPO segment was 4.0 nm. According to the diffusion time measured with FCS and equation 2.5, the length of the molecule was determined to be 13.8 nm, and the diameter was 3.4 nm. Therefore, the dimension of the molecules determined by FCS was in good agreement with the prediction.

The cross correlation between the data obtained at 633 nm and 488 nm (black line) was also detected. Here we determined a larger diffusion time of 370 μs, which corresponded to a hydrodynamic radius of 13 nm according to equation 2.4. It implied that the exchange of molecules between the micelles and its environment in fact took place.

3.2 Ex-situ visualization of enzymatic growth

The enzymatic reactions were carried out by mixing reaction buffer, 1 nmol of DNA-*b*-PPO block copolymers, 150 nmol of dTTP and 40-60 units of TdT together. This mixture was incubated for different times at 37°C in a thermoshaker. At certain time intervals (15, 30, 60, 180, 300, 960 min), the reaction was stopped by placing the samples in the freezer at -20 °C and the size of the nanoparticles was analyzed by atomic force microscopy on a mica surface in soft tapping mode (Fig. 3.3). The maximum height of individual micelles was determined by a local roughness analysis.
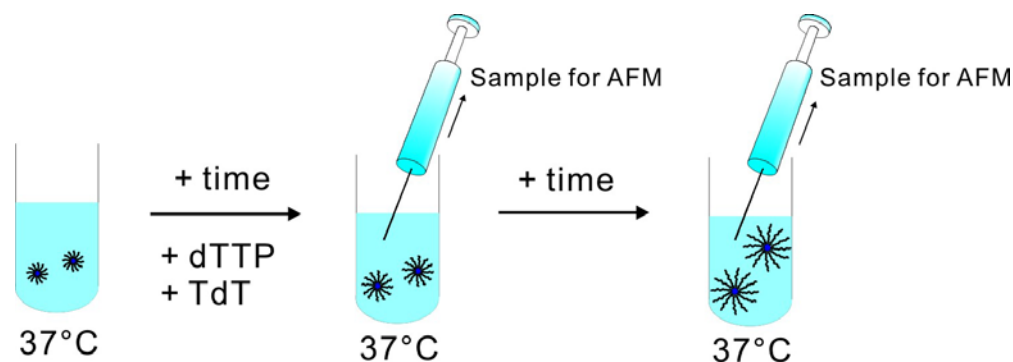
Figure 3.3 *Cartoon of the process of observing the enzymatic growth of DNA-b-PPO micelles by AFM ex-situ.*

AFM analysis revealed spherical nanoparticles after reaction times of 60 min and 16 h (Fig. 3.4). Histograms of the micelle heights were compiled for at least 100 nanoobjects, resulting in h_{max} of 6.6 ± 1.4 nm and 11.2 ± 1.9 nm, respectively. The heights of the micelles increased compared to the height before reaction, which was 4.9 ± 1.2 nm.
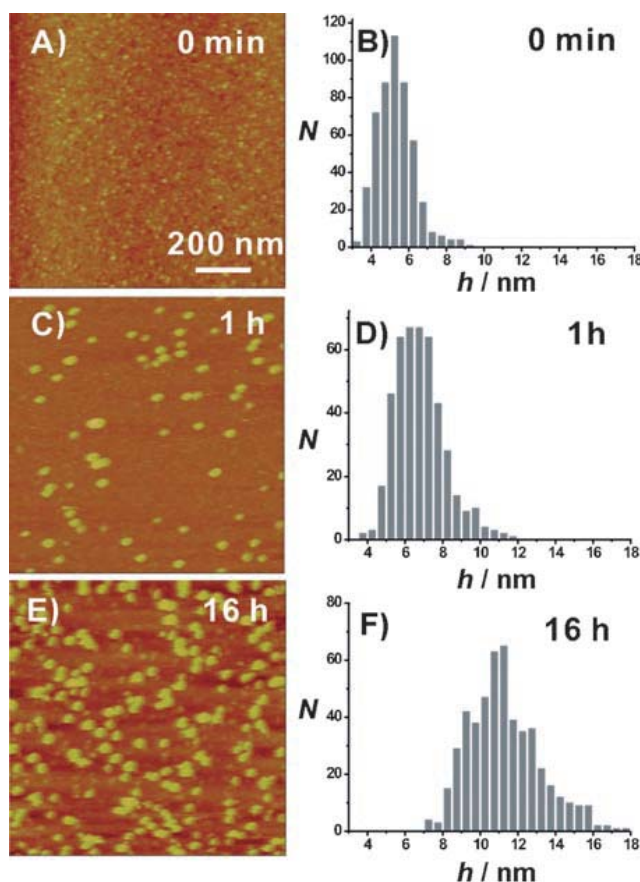
Figure 3.4 *AFM analysis of DNA block copolymer nanoparticles that were extended by adding thymidines using the TdT enzyme. (A), (C), and (E) show representative AFM topographical images at different reaction times, and presented at the same scale. (B), (D), and (F) illustrate the corresponding histograms of the nanostructure heights h.*

In order to test the influence of the ratio of setpoint amplitude A to the free amplitude A_0 on the height of micelles, I imaged DNA-*b*-PPO micelles after enzymatic reaction by AFM (Fig. 3.5). For soft tapping, I normally use a ratio A/A_0 of about 95% (Fig. 3.5 A), and statistical analysis of the measured height of micelles gave a value of 8.3 ± 1.2 nm. For each ratio varied from 93% to 73%, I captured one height image. When A/A_0 was 93%, 87%, 80%, and 73%, the mean height of the micelles was 8.4 ± 1.2 nm, 7.8 ± 1.4 nm, 6.7 ± 1.4 nm, and 6.9 ± 1.6 nm, respectively.
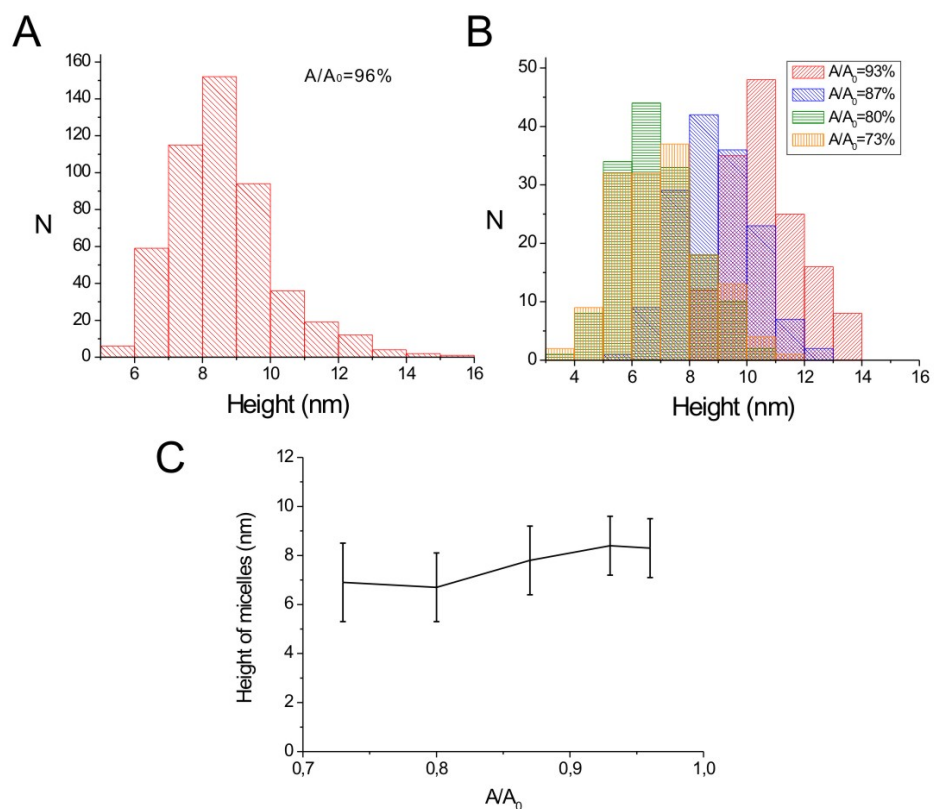
Figure 3.5 (*A*) and (*B*): the histograms of the height of micelles measured from images captured with different ratio of setpoint amplitude A to free amplitude A_0. (*C*): the plot of height of micelles versus ratio of setpoints.

Furthermore, AFM analysis was also performed at t = 15, 30, 180, 300 min, and the determined h_{max} were summarized in Table 1. Clearly, the height of the nanoparticles increased with reaction time. The AFM measurements revealed that the spherical shape of the nanoparticles persisted upon nucleotide addition through TdT.

t (min)	h_{max} [a] (nm)	increase of h_{max} (%)	T segment added[b]	diameter [c] (nm)	increase of diameter(%)
0	4.9 ± 1.1	-	-	9.6 ± 0.9	-
15	5.1 ± 1.4	4.1	6 ± 4	9.9 ± 1.1	3.1
30	5.2 ± 1.3	6.1	11 ± 3	10.8 ± 1.6	12.5
60	6.6 ± 1.4	34.7	22 ± 5	12.4 ± 0.8	29.2
180	7.2 ± 1.5	46.9	35 ± 8	13.7 ± 1.3	42.7
300	8.3 ± 1.6	69.4	43 ± 7	17.5 ± 1.4	82.3
960	11.2 ± 1.9	128.6	62 ± 11	23.0 ± 0.8	140.0

Table 3.1 *Characterization of DNA block copolymer micelles that were enlarged by TdT reaction. [a] derived from AFM measurements, [b] determined by PAGE, [c] based on FCS analysis.*

To determine the number of nucleotides added with increasing enzyme incubation times, DBCs extended with thymidine (T) residues were analyzed by polyacrylamide gel electrophoresis (PAGE) (Fig. 3.6).[53]
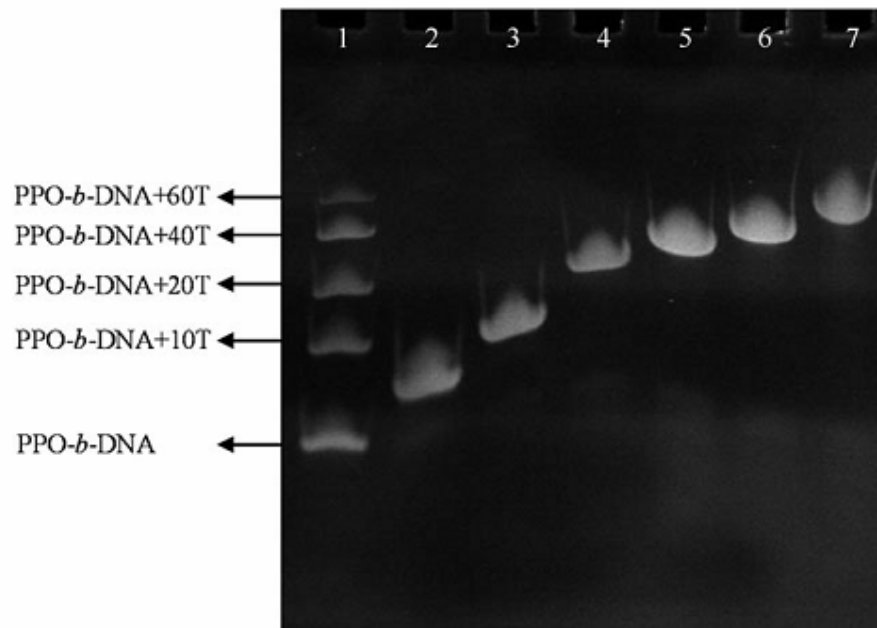
Figure 3.6 *Gel electrophoretic analysis of the DBCs after different reaction times with TdT. Lanes are as follows: DNA-b-PPO molecular weight standards (1), and the products of incubation with TdT for 15 min (2), 30 min (3), 60 min (4), 3 h (5), 5 h (6), and 16 h (7).*

A variety of DNA-*b*-PPO block copolymers were prepared consisting of the 22-mer sequence and additional thymidine segments of variable length attached at the 3' end (0, 10, 20, 40 and 60) T residues as molecular weight standards. From the gel electrophoretic analysis it can be concluded that incubation with TDT for 15, 30, 60, 180, 300, and 960 min resulted in the addition of 6 ± 4, 11 ± 3, 22 ± 5, 35 ± 8, 43 ± 7, and 62 ± 11 T residues, respectively.

Apart from investigating the morphology of micelles adsorbed on the mica surface with AFM, FCS measurements were carried out in cooperation with Dr. Michael Börsch (University of Stuttgart) (Fig. 3.2).
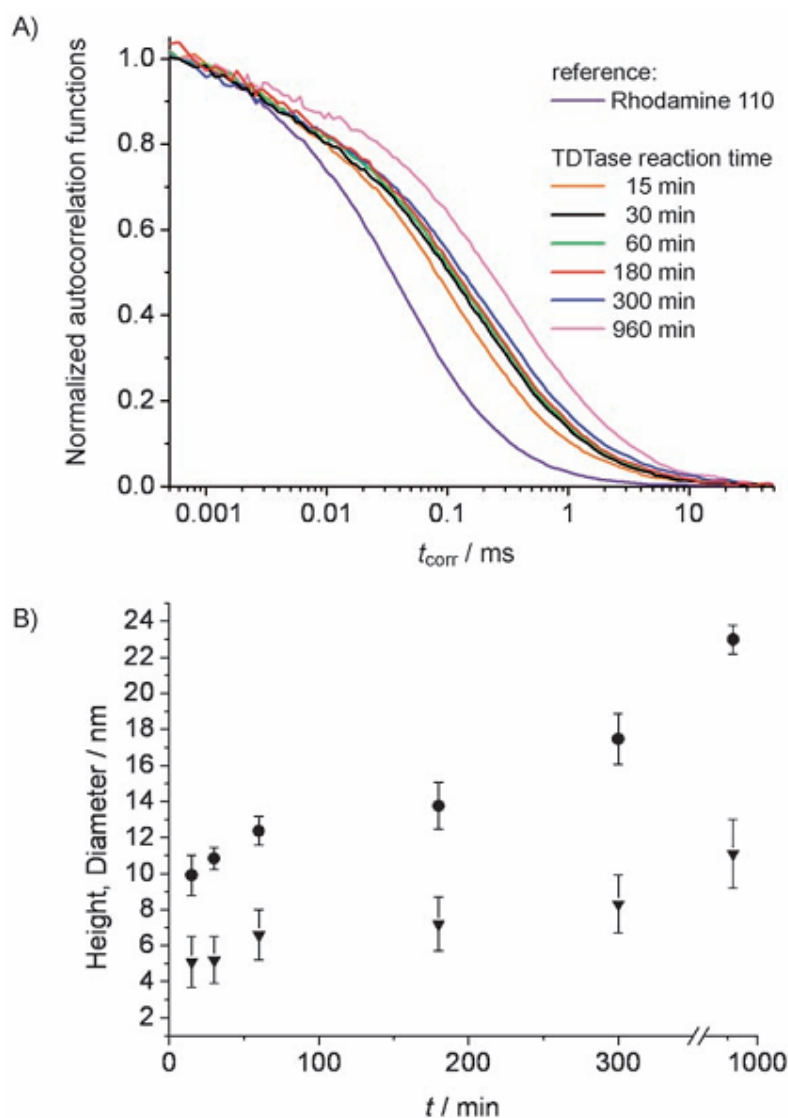
Figure 3.7 *(A) The autocorrelation functions of the DBC molecules and micelles after different incubation times with the TdT enzyme. (B) The diameters obtained by FCS (filled circles) and the mean maximum heights (filled triangles) of the micelles obtained from AFM.*

Mean diameters of 9.9 ± 1.1 nm, 10.8 ± 0.6, and 12.4 ± 0.8 nm were found for the mixture of DBC molecules and micelles after 15 min, 30 min, and 60 min of incubation with TdT, respectively. With increasing reaction time, the diameter increased to 13.7 ± 1.3 nm (3 h) and 17.5 ± 1.4 nm (5 h). Extension with TdT for 16 h resulted in a diameter of 23.0 ± 0.8 nm (Fig. 3.7 A and Table 3.1). Although these

values were not exactly the diameter of the micelles or molecules, they could still reflect the extension of molecules or growth of micelles. In fact, these values are in good agreement with trends established from the AFM in the growth of the micelles (Fig. 3.7 B and table 3.1).

3.3 In-situ visualization of enzymatic growth of DNA-*b*-PPO micelles

As atomic force microscopy allows the direct visualization of DNA molecules in near-physiological environments, the enzymatic growth of DNA-*b*-PPO micelles can be studied in-situ. The formation of these nanoparticles can also be utilized as a patterning method not relying on lithography based on the phase separation of block copolymers. It allows one to fabricate small features down to a few nanometers in diameter.[54] The scaling behavior of polymeric and biopolymeric nanostructures fabricated by surface initiated polymerization has recently been studied by Lee et al. [55] Patterns ranging in lateral size from 100 nm to 4 µm were studied. In our study, the enzymatic growth of DNA-*b*-PPO micelles extended the range of patterns sizes down to the scale of tens of nanometers.

3.3.1 Control by adding dTTP mononucleotides

In order to achieve this purpose, an experimental procedure had to be developed that did not inhibit the activity of TdT and which allowed the stable imaging of PPO-*b*-DNA micelles. I found that the following procedure fulfilled the above requirements: A drop of 20 µl of the reaction mixture was deposited onto freshly cleaved mica. The droplet contained 1 µl of 1.8 mg/L DNA-*b*-PPO, 2 µl of 20 U/µl TdT, 4 µl of the 5× enzyme reaction buffer, and 13 µl of the imaging buffer. The final concentration of DNA-*b*-PPO and TdT was 90 µg/L and 2 U/µl, respectively.

After an incubation time of 10 min on the mica surface, the sample was diluted with 150 µl of imaging buffer, by carefully pouring the buffer solution over the mica onto a piece of filter paper without allowing the mica surface to dry. The mica was then covered with 50 µl of the imaging buffer. Afterwards, the mica sheet was mounted in the AFM. The measurements were carried out in an O-ring sealed glass liquid cell, which was filled with buffer solution.

The sample was heated from 22 °C to 37 °C at a rate of 1.6 °C/min. The topography of the mica surface was investigated after temperature adjustment (Fig.3.8 A). AFM images were recorded in soft tapping mode. Globular structures were observed, showing a small variation in height and size. I found that the structures did not change with time and therefore constituted a defined starting point.

I collected the height data of approx. 300 surface features for the image recorded at T = 0 min and plotted them in a histogram (Fig. 3.8 B). The histogram is composed of two peaks, which were fitted by Gaussian distributions. One peak was at 3.0 ± 0.5 nm, and the other was at 4.5 ± 1.3 nm. I hypothesized that one peak was attributed to TdT, and the other was caused by DNA-*b*-PPO micelles.
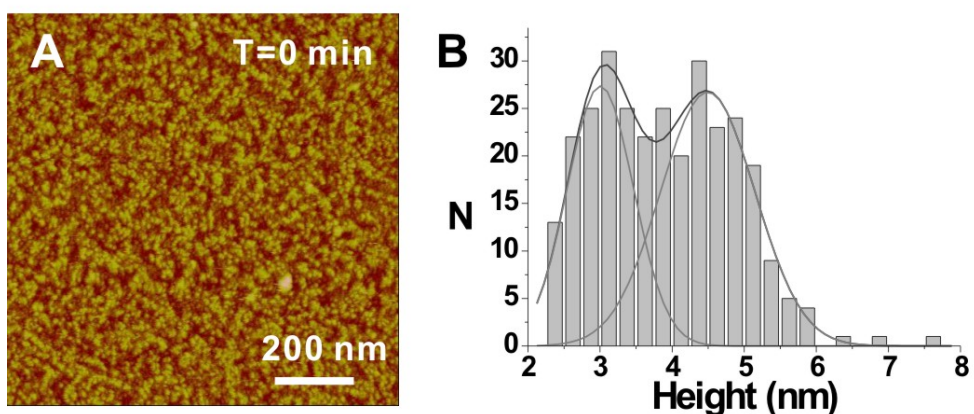
Figure 3.8 (A) *AFM image of the reaction mixture before the injection of dTTP to the liquid cell at 37 °C and (B) the height distribution of the surface structures. The lateral scale is 200 nm and the height scale is 15 nm. The histogram was fitted by two Gaussian distributions.*

As both TdT and DNA-*b*-PPO micelles have similar sizes at the beginning, two control experiments with either only TdT or DNA-*b*-PPO micelles in buffer solution were performed (Fig. 3.9 A and B). This separate analysis of TdT and DNA-*b*-PPO micelles allowed us to obtain a more precise size distribution of both constituents. The histogram of the analyzed heights of the TdT enzymes revealed a maximum at 3.2 ± 1.2 nm (Fig. 3.9 C). In contrast to the TdT enzyme, I determined an average height of the DNA-*b*-PPO micelles of 4.3 ± 2.0 nm (Fig. 3.9 D). These results agree with our above hypothesis about the peaks.
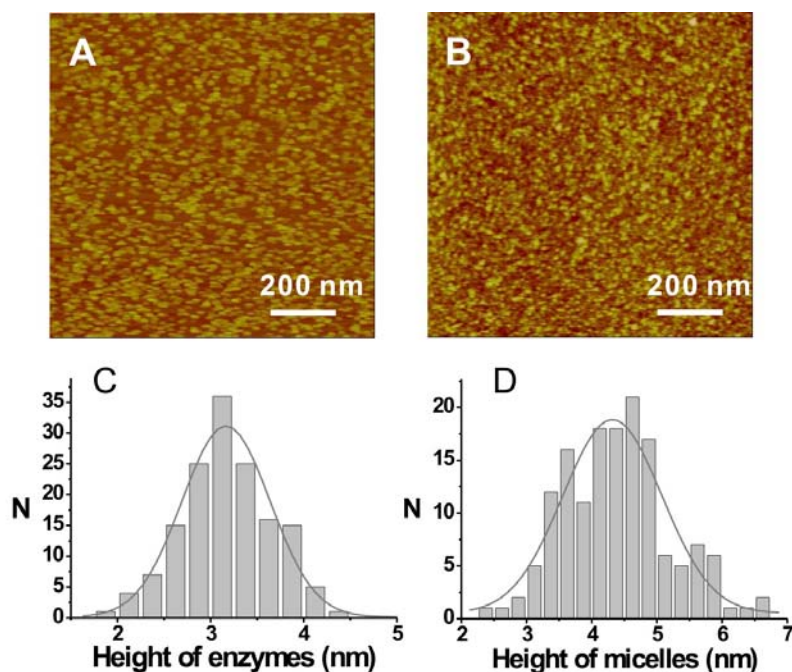
Figure 3.9 *Pure TdT and DNA-b-PPO diblockcoplymer micelles imaged by tapping mode AFM in buffer and their distributions of height. (A) TdT at a concentration of 0.2 U/µl in the imaging buffer solution. (B) DNA-b-PPO at a concentration of 180 µg/L in the imaging buffer solution. In both cases, the substrate was freshly cleaved mica and the height scale is 15 nm. (C) Histogram of the height of TdT obtained from (A). (D) Histogram of the height of the DNA-b-PPO micelles obtained from (B). The histograms were fitted by a Gaussian distribution.*

In the in-situ experiment, I injected 2 µl of 10 mM dTTP mononucleotide into the fluid cell, which defined T = 0 min for the enzymatic reaction. Afterwards, successive AFM images were captured, while all parameters were kept constant. In order to analyze the growth process in more detail, I collected the height data of approx. 300 surface features for images recorded at T = 20, 40, 134, 540 min and plotted them in histograms (Fig. 3.10). Each histogram is composed of two peaks, which were fitted by Gaussian distributions. The position and the shape of the first peak around 3 nm remained uniform after the injection of dTTP (T = 20 min: 2.7 ± 0.4 nm; T = 40 min: 2.8 ± 0.5 nm; T = 134 min: 2.9 ± 0.4 nm, and T = 540 min: 2.7 ± 0.5 nm). Therefore, this phenomenon confirmed that this peak was resulted from TdT enzymes on the

surface. The second peak shifted from 4.5 ± 1.3 nm at T = 0 min, to 5.0 ± 2.3 nm at T = 20 min, to 5.7 ± 2.7 nm at T = 40 min and to 6.3 ± 2.9 nm at T = 134 min, respectively. As this increase indicates the growth of structures, the second peak was assigned to DNA-*b*-PPO micelles participating in the enzymatic reaction. The histograms obtained after 134 min reaction time did not show a further shift in the peak position, i.e. the mean height of the DNA-*b*-PPO micelles.
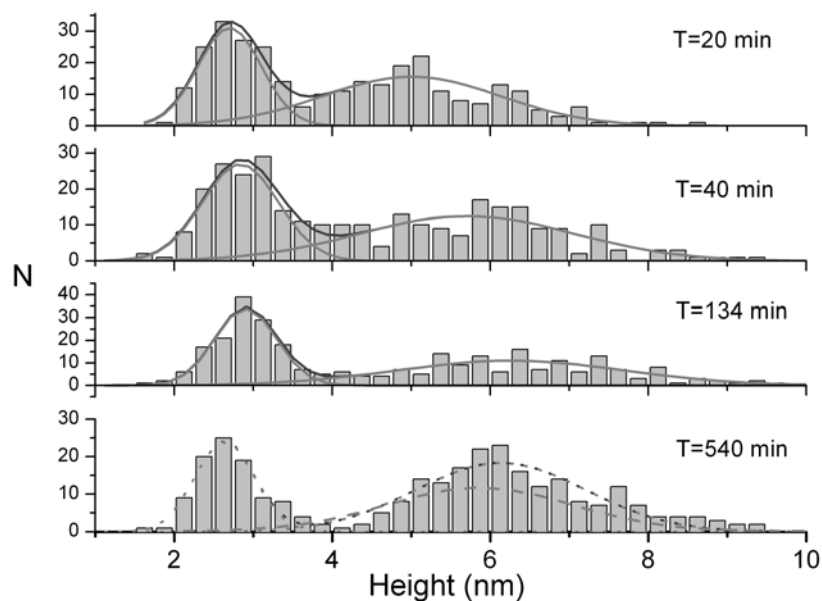

Figure 3.10 *Histograms of height of globular structures obtained from AFM measurements after the injection of dTTP to the liquid cell at 37 °C. Each histogram was fitted by two Gaussian distributions.*

The integral value of the Gaussian fits for TdT enzymes and DNA-*b*-PPO micelles were found to be independent of the time of enzymatic reaction. This indicates that the number of structures observed remained constant and that they did not desorb from the surface or were not moved by the scanning process to the edge of the scan area. Furthermore, the development of the two peaks, as seen from our statistical analysis, showed that most micelles participated in the enzymatic reactions.

The mean height data that were determined by the Gaussian peak of the fitted histograms of the DNA-*b*-PPO micelles are plotted in Fig. 3.11 (filled circles). The height of the micelles reached a plateau after about 1 hour. This result is consistent with the observation from measurements on surface-initiated polymerization of grafted DNA chains.[50]
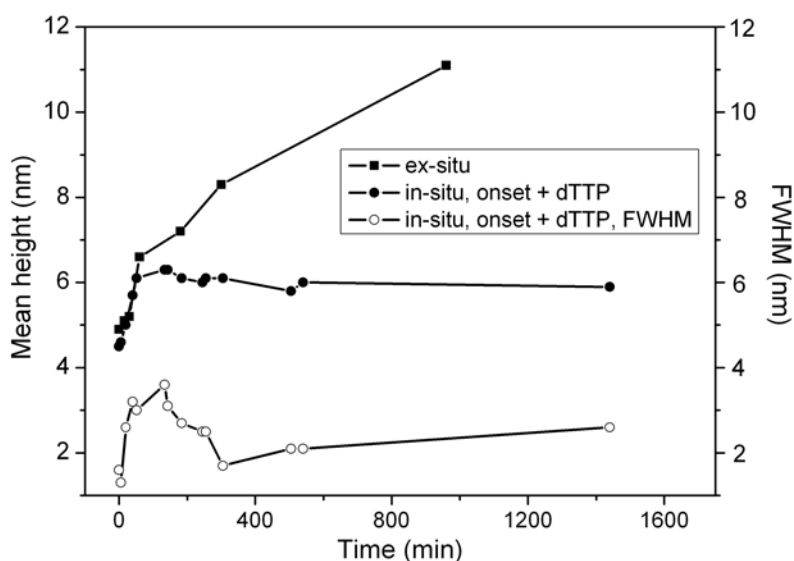

Figure 3.11 *Variations of the mean height of DNA-b-PPO micelles and the full width of the histogram at half maximum height (FWHM) as a function of the reaction time for the in-situ and ex-situ measurements. "Onset + dTTP" stands for starting of the enzymatic reaction by adding monomers. Filled symbols correspond to mean height axis shown left and open symbols correspond to full width half maxima (FWHM) given on the right side.*

Interestingly, some micelles seemed to grow faster than others, a result seen from the change in the width of the Gaussian distribution. I defined FWHM as the full width of the histogram at half maximum height. FWHM increased in the beginning of the reaction from 1.6 ± 0.2 nm to 3.6 ± 0.4 nm 134 min after the injection of the dTTP

mononucleotide. This value was then found to decrease to 2.1 ± 0.3 nm at a time of 505 min after the injection. The reduction in the width of the Gaussian distribution indicates that the enzymatic reaction was slowed down or was disabled after a certain length of DNA was reached, while at the same time, shorter DNA strands could be still extended by TdT.

In order to confirm that the size distribution of micelles was representative, two reference experiments were performed at T = 540 min and T = 1440 min. First, I varied the surface area, which was investigated by AFM (dotted line Fig. 3.10). Second, I changed the AFM tip, in order to exclude artifacts from the tip shape (dashed line of Fig. 3.10). Both reference experiments did not show any significant variation on the reported data.

To elucidate the size of DNA-*b*-PPO micelle nanostructures independent of the influence of a surface, I compared the *in-situ* growth with the *ex-situ* growth which showed no saturation effect (Fig. 3.11, filled squares).[12] In particular, the growth in both experiments showed the same slope of 0.03 nm/min for reaction times <60 min. Thus I conclude that the surface must play the major role in saturation of growth.

I next would like to consider the reason for the termination of the TdT-catalysis of micelle nanostructures on the surface. In order to exclude a reduction of monomer access or a change in TdT catalytic behavior over time, I performed a control experiment with a DNA-*b*-PPO polymer exhibiting a significantly longer DNA segment composed of 42 bases (Fig. 3.12).
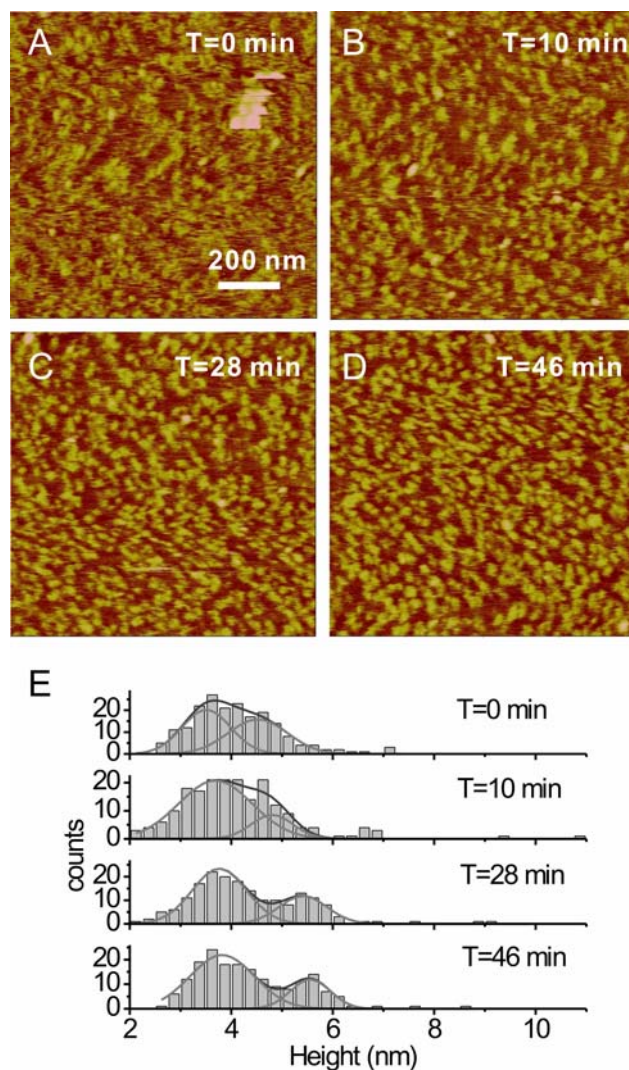
Figure 3.12 *In-situ observation of the enzymatic reaction of 42mer DNA-b-PPO micelles and height distribution of surface structures. (A) Before injection of dTTP. (B) 10 min (C) 28 min (D) 46 min after injection of dTTP. The lateral scale is 200 nm and the height scale is 10 nm for all images. (E) Histograms of height of globular structures obtained from AFM measurements. Each histogram was fitted by two Gaussian distributions.*

I found that the saturation in growth was reached 28 min after the initiation of the reaction, which was about 30 min earlier than that in the experiment with the 22 mer DNA-*b*-PPO micelles (Fig. 3.13). Thus a reduction of monomer access and changes in catalytic behavior played a minor role. It also suggested that DNA-*b*-PPO

interacted with the mica surface in a way that significant further growth could not be observed after the ssDNA segment had reached a certain length.
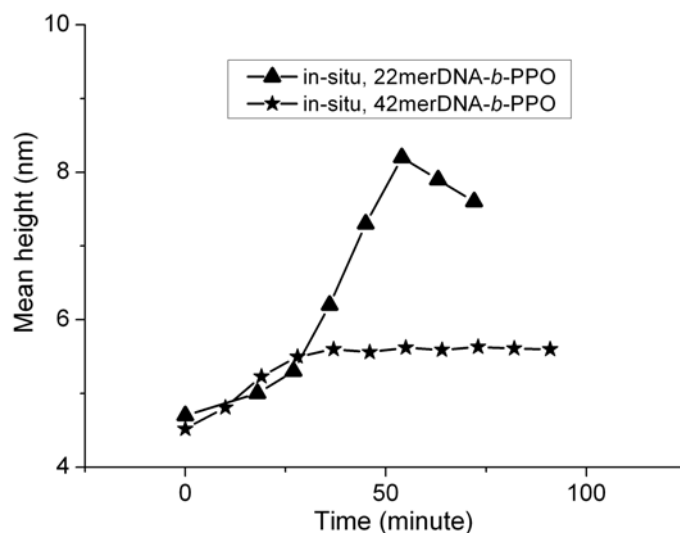

Figure 3.13 *Variations of the mean height of DNA-b-PPO micelles as a function of the reaction time for the in-situ measurements with 22merDNA-b-PPO micelles and 42merDNA-b-PPO micelles. Both enzymatic reactions were controlled by temperature (37°C).*

In the *ex-situ* reaction, growth in the size of the micelles in solution might be mediated by exchange of DNA-*b*-PPO molecules of micelles with single molecules in solution.[56, 57] As reported, the residence time of the block copolymer molecules in the micelles could be on the order of hours, [58] which fits to the time scale of our experiments. FCCS measurements of the micelles could also support this hypothesis. By analyzing the cross correlation function ($G_{cross\ corr}$ (t=0)) in dependence of time (Fig. 3.14), we found a decrease in the amplitude of the cross correlation function, which was attributed to the saturation of the exchange of labeled dsDNA-*b*-PPO molecules within the solution.
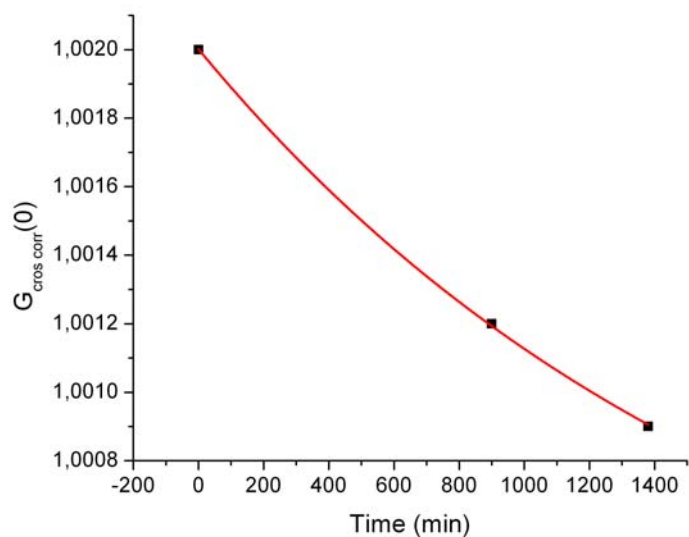
Figure 3.14 *The dependence of the cross correlation function on time.*

The exchange of molecules can also be noticed by the size distribution of micelles recorded after 60 minutes of *ex-situ* reaction compared to the one recorded in the *in-situ* reaction (Fig. 3.15).
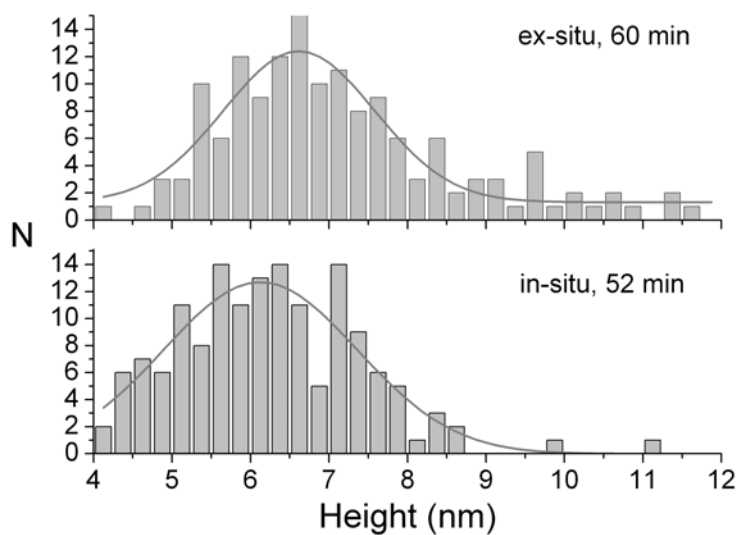

Figure 3.15 *Histograms of height of micelles after ex-situ enzymatic reaction of 60 min and in-situ enzymatic reaction of 52 min. The histograms were fitted by Gaussian equation.*

For the *ex-situ* reaction, I determined a FWHM, which was 2.2 ± 0.2 nm (Fig. 3.15). This width was smaller than that one of the *in-situ* experiment of the micelles for a time of 52 minutes (FWHM = 3.0 ± 0.3 nm). In solution, all DNA-*b*-PPO molecules have the same probability to react with dTTP in the presence of TdT. Exchange of DNA-*b*-PPO molecules in micelles and in solution take place and lead to a more even distribution of the length of DNA-*b*-PPO molecules in micelles. However, for DNA-*b*-PPO molecules of immobilized micelles on the mica surface, both exchange processes were reduced, especially for the exchange of DNA-*b*-PPO molecules in micelles with single molecules in solution.

Another effect leading to the termination of the TdT-catalysis of immobilized micelles composed of DNA-*b*-PPO molecules could be that after reaching a certain length, the ssDNA segments fold back into the DNA corona and block the catalytic site (Fig. 3.16).
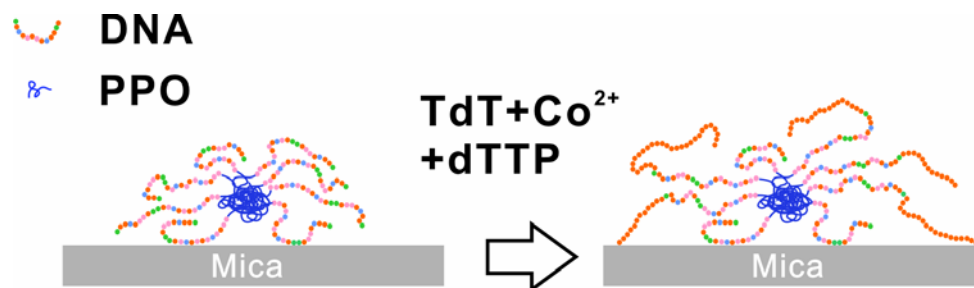
Figure 3.16 *Diagram showing the growth of the DNA-b-PPO diblockcopolymer micelles on mica in a buffer solution in the presence of TdT, Co^{2+}, and dTTP.*

The persistence length of a single-stranded DNA is 0.75 ~ 1.3 nm.[59-61] It is shorter than the length of the DNA segment in micelles before enzymatic reaction (3.3 nm). In micelles, DNA-*b*-PPO molecules are ordered and the length upon which significant back folding can occur could increase. In addition, we must consider that as the DNA

segment becomes longer, the surface interaction could also result in prevention of catalysis. In the case that the latter effect was the dominant contribution, the enzymatic growth would be terminated only at the edges of patterns composed of self-assembled oligonucleotide monolayers on gold.[50]

3.3.2 Continuous monitoring of selected micelles

The catalytic reaction can also be initiated solely by controlling the reaction temperature to the temperature optimum of TdT. In this way, the drift of the surface relative to the AFM-tip, which may be induced by the injection of dTTP, can be avoided.

I therefore prepared 20 µl of the reaction mixture, which contained all the components for the enzymatic reaction, and controlled the onset of the reaction by increasing the temperature to 37 °C. The reaction mixture contained 1 µl of 1.8 mg/L PPO-*b*-DNA, 2 µl of 20 U/µl TdT, 2 µl of 10 mM dTTP, 4 µl of 5× enzyme reaction buffer, and 11 µl of imaging buffer. The final respective concentration of PPO-*b*-DNA, TdT and dTTP were 90 µg/L, 2 U/µl, and 1 mM in a Ni^{2+} containing 1× reaction buffer.
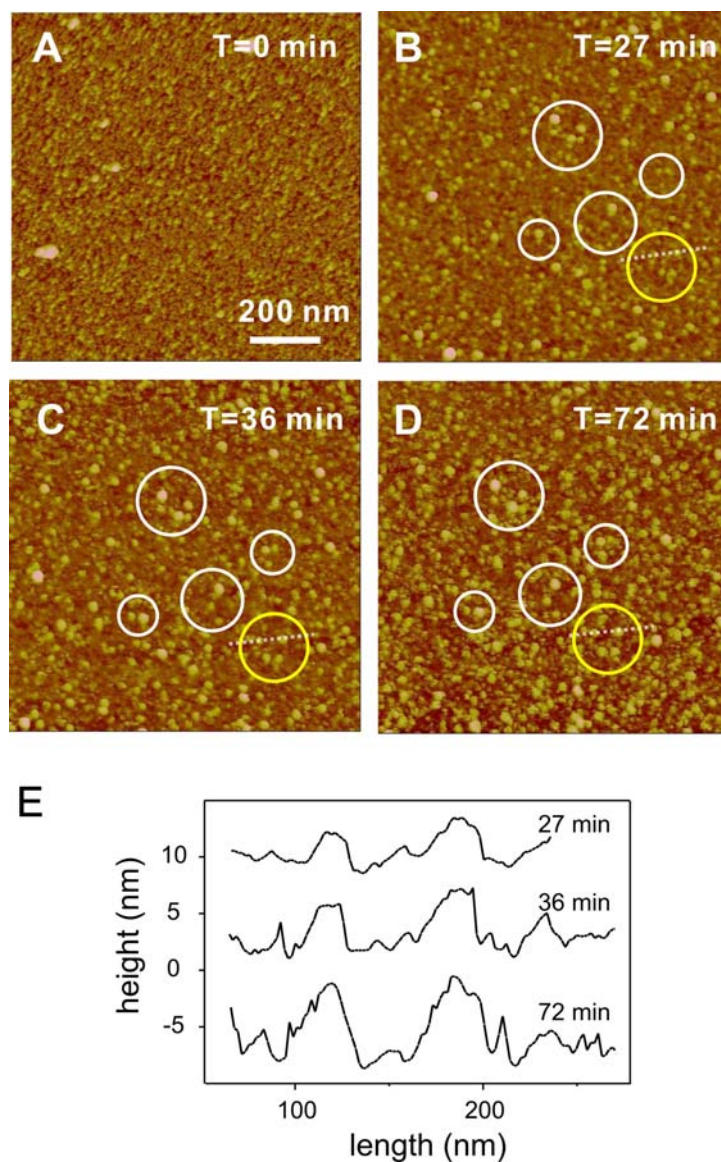
Figure 3.17 *Selected time-lapse AFM images of the reaction mixture before and after the temperature was increased to 37 °C. Lateral scale bar: 200 nm. The height scale is 15 nm. (A) Before heating. (B) 27 min after 37 °C was reached. (C) 36 min after 37 °C was reached. (D) 72 min after 37 °C was reached. (E) Height profiles along the line in Fig. 3.9 B-D.*

Fig. 3.17 A shows the image recorded at room temperature (23 °C) and corresponds to the reaction time T = 0 min. The temperature of the mixture was increased to 37 °C at a rate of 1.6 °C/min, in order to start the reaction. The surface was imaged again 18 minutes after reaching 37 °C (Fig. 3.17 B). The AFM image shows that the height of

some globular structures increased. I continued to image the surface at 37 °C and kept all scanning parameters constant (Fig. 3.17 C and D). In this way, I was able to follow the size and arrangement of individual structures on the surface, e.g. the features marked by the circles could be recognized and compared in different images.

I made topographical profiles (Fig. 3.17 E) of the two structures inside the yellow circle at T = 27, 36 and 72 min along the dotted line which is indicated in the figures. The left structure increased its height by 86 % from 3.5 nm to 6.5 nm and the right one by 89 % from 3.6 nm to 6.8 nm. From this I concluded that these structures were DNA-b-PPO micelles, which grew both vertically and laterally in the presence of TdT. However, some structures in the topography remained unchanged, as observed in the above results when the control was achieved by adding dTTP mononucleotide. These features might be the TdT. Alternatively; they might be micelles that did not grow owing to the spatial hindrance that resulted in the inaccessibility of the free 3' hydroxyl ends of the DNA segments to TdT.

In order to obtain a better statistic of the structures undergoing changes, I collected the height data of 300 surface features at T = 0, 27, 36 and 72 min and plotted them in histograms (Fig. 3.18). The increase in the mean height of the micelles, determined from the Gaussian fits, can be seen from Fig. 3.13 (filled triangles). In the temperature controlled experiment, the mean height of the micelles stopped increasing after about 1 h. This time is similar to the time observed for the TdT-reaction initiated by the mononucleotide addition.
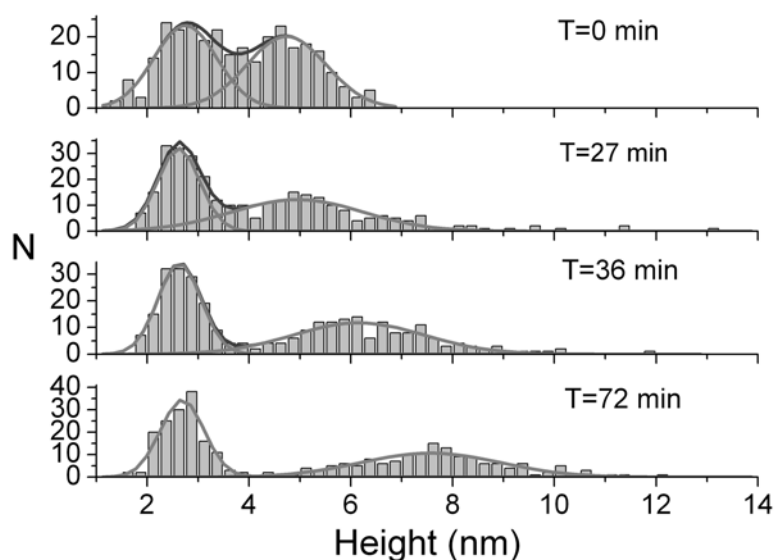
Figure 3.18 *Histograms of height of globular structures obtained from the images shown in Figure 3.9. Each histogram was fitted by two Gaussian distributions. Both the peak of TdT and the peak of DNA-b-PPO micelles could be distinguished clearly. The peak of TdT remained constant at approx. 3 nm for all images analyzed. The peak of DNA-b-PPO shifted from 4.7 nm at 23 °C to 7.6 nm 72 min after 37 °C was reached.*

3.3.3 Calculation of the number of T-bases added to DNA-*b*-PPO

The average height and radius of the DNA-*b*-PPO micelles could be correlated to the average number of mononucleotides added to DNA-*b*-PPO molecules. Here, I assumed that the DNA segments were freely jointed chains, and the length of a DNA-*b*-PPO molecule in the micelle was

$$L = \sqrt{N_{base}} \cdot l_{base} + R_{PPO} \tag{3.2}$$

where N_{base} was the number of bases, l_{base} was the length per base, and R_{PPO} was the gyration radius of PPO.[62] In this equation R_{PPO} was not doubled as in equation 3.1,

because micelles deformed to adsorb to the substrate owing to electrostatic interactions. Before the enzymatic reaction, N_{base} was 22. I assumed 0.7 nm/base for single-stranded DNA considering results determined using different approaches.[59, 63, 64] In this way, the length of the DNA segment in micelles was calculated to be 3.3 nm from equation 3.2, and the length of the DNA-*b*-PPO molecule was $L = 5.3$ nm before the enzymatic process at T=0 min.

Next, I used a simple geometrical model, in order to estimate the number of bases added (Fig. 3.19). The tip could be modeled as a cone with a spherical end (radius of curvature R_{tip}). In our experiment, the radius of the micelle was similar to the radius of the tip. I could therefore determine $R_{micelle}$ using the Pythagoream theorem.

$$(R_{tip} + R_{micelle} - h)^2 + R_{SFM}^2 = (R_{tip} + R_{micelle})^2 \qquad (3.3)$$

In this equation, R_{tip} was the tip radius of curvature, $R_{micelle}$ was the radius of the micelle, h was the measured height of the micelle, and R_{AFM} was the measured radius of the micelle. R_{AFM} and h could be obtained using the statistical analysis of the AFM images.
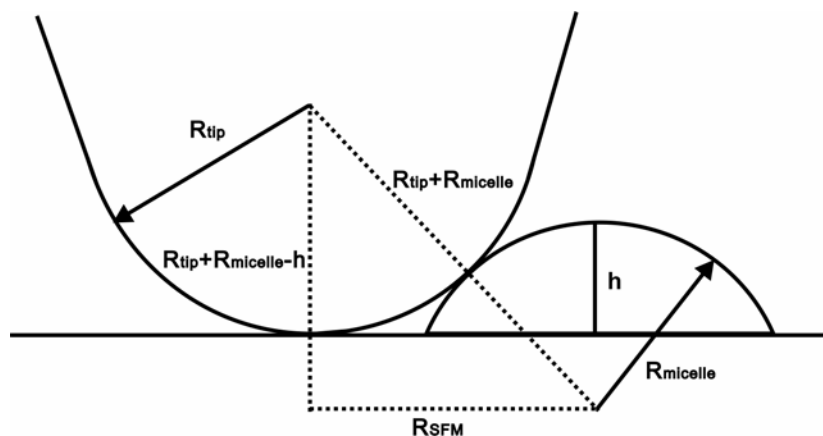
Figure 3.19 *Diagram showing the model of imaging a DNA-b-PPO micelle with an AFM tip. R_{tip} was the tip radius of curvature, $R_{micelle}$ was the radius of the micelle, h was the measured height of the micelle, and R_{AFM} was the measured radius of the micelle.*

In the initial case, before the enzymatic reaction, R_{AFM} = 10.2 nm, and h = 4.7 nm. The tip radius of curvature R_{tip} was 8 nm (Fig. 3.20). The radius of the micelle $R_{micelle}$ could therefore be calculated to be $R_{micelle}$ = 5.4 nm.
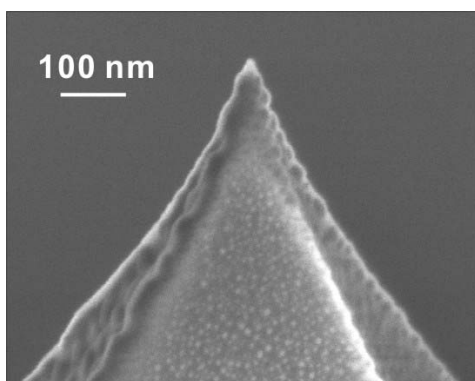

Figure 3.20 *Scanning electron microscope image of a tip after an in-situ measurement. The radius of curvature of this tip was 8 nm.*

I assumed that the length of the DNA-*b*-PPO molecule was equal to $R_{micelle}$, and then the number of bases in the DNA-*b*-PPO molecule must be 24 according to equation

3.2, which was a value that was 9.1% different than the actual number of bases (22) before the enzymatic reaction.

I also imaged 42mer DNA-*b*-PPO micelles using scanning force microscopy, and measured the radius and height of the micelles. The values were 14.0 nm and 4.5 nm, respectively. The tip radius of curvature was 17 nm (Fig. 3.21). In this case, the number of bases was calculated using equation 3.2 and 3.3 to be 52. Here there was a difference of 23.8% compared with the actual number of bases (42).
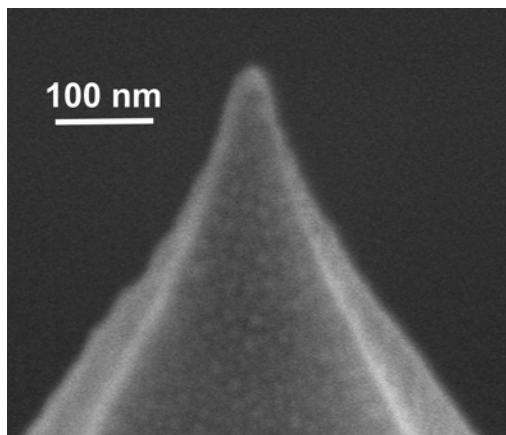

Figure 3.21 *Scanning electron microscope image of the tip after a measurement with DNA(42mer)-b-PPO micelles. The radius of curvature of this tip is 17 nm.*

After an enzymatic reaction time of 72 min, I obtained a radius of micelle R_{AFM} of 13.4 nm and a mean height h of 7.6 nm from the AFM measurement. According to equation 3.3, I could obtain the radius of the micelle $R_{micelle}$ to be 7.6 nm. I assumed that the length of the DNA-*b*-PPO molecule was equal to $R_{micelle}$ ($L = R_{micelle} = 7.6$ nm), then I calculated the number of bases N_{base} from equation 3.2 to be 64. The number of added bases to DNA-*b*-PPO within a micelle was in average $\Delta N_{base} = 64 - 22 = 42$, after 72 min of enzymatic reaction. Based on the above discussed estimation, I calculated the extension of DNA-*b*-PPO molecules within micelles for all AFM images obtained from the reaction initiated by temperature (Fig 3. 22).
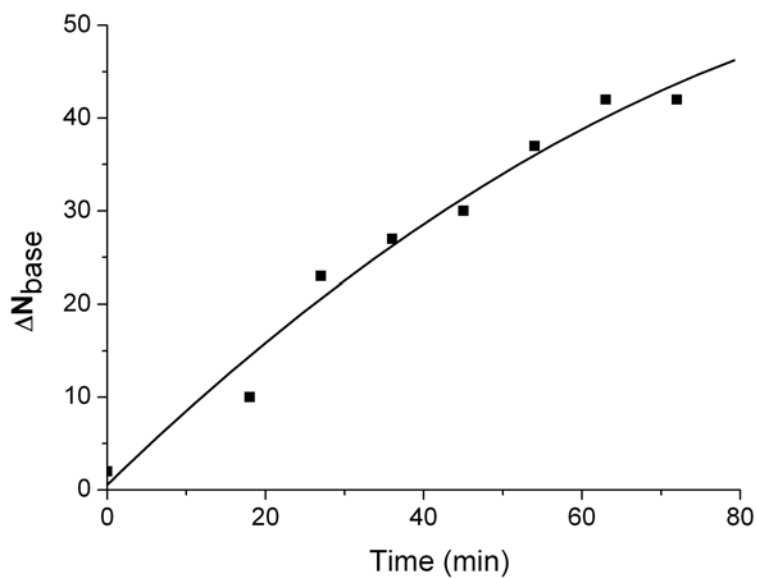
Figure 3.22 *The plot of the number of extended T-bases versus reaction time for the in-situ experiment, when the reaction was controlled by temperature.*

The height of micelles measured by AFM and the number of added T segment in both ex-situ and in-situ enzymatic reactions were summarized in Table 3.2. Generally speaking, in in-situ measurement, the number of added T segment was larger than that in ex-situ measurement. This phenomenon could be resulted from the higher amount of TdT enzyme in in-situ experiment, which was 1000 times more than that in ex-situ experiment.

Ex-situ			In-situ		
t (min)	h_{max} [a] (nm)	T segment added[b]	t (min)	h_{max} [c] (nm)	T segment added[d]
0	4.9 ± 1.1	-	0	4.7 ± 0.8	2
15	5.1 ± 1.4	6 ± 4	18	5 ± 1.3	10
30	5.2 ± 1.3	11 ± 3	27	5.3 ± 1.3	23
60	6.6 ± 1.4	22 ± 5	36	6.2 ± 1.3	27
180	7.2 ± 1.5	35 ± 8	45	7.3 ± 1.1	30
300	8.3 ± 1.6	43 ± 7	54	8.2 ± 1.5	37
960	11.2 ± 1.9	62 ± 11	63	7.9 ± 1.2	42

Table 3.2 *The height of micelles and the number of added T segment in ex-situ and in-situ enzymatic reactions. [a] derived from ex-situ AFM measurements, [b] determined by PAGE, [c] derived from in-situ AFM measurements, [d] estimated from the geometrical model.*

Chapter 4

Building a macroscopic DNA machine

4.1 Properties of DNA-*b*-PPO monolayer

4.1.1 The shape of the isotherm

Pressure-area (π-A) isotherms of 2 nmol DNA(11mer)-*b*-PPO molecules dissolved in 10 mL dichloromethane situated at the air-water interface were recorded with a compression/expansion rate of 17.5 cm^2/min at 20.0 °C (Fig. 4.1).
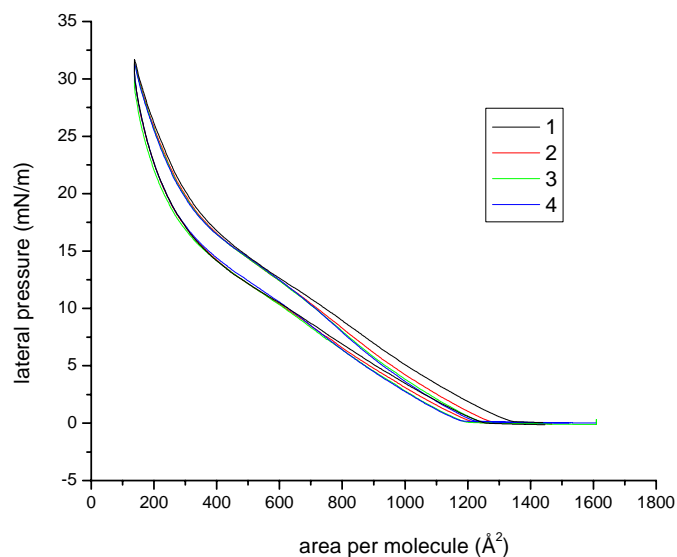

Figure 4.1 *Isotherms of the DNA-b-PPO monolayer recorded in four continuous compressing and expanding circles.*

For the first isotherm (black line), I observed a takeoff area of 1346 Å^2 in the compression curve. This value corresponds approximately to the circular sectional area of the of the PPO block (1225 Å^2) which was calculated from the gyration radius (19.7 Å) of PPO with a molecular weight of 6800 g/mol. [52] As Mortensen did, I assumed that PPO had the monomer length l of the order of 2 Å similar with PEO. The gyration radius was calculated using equation 4.1

$$R_g = \sqrt{\frac{Nlb}{6}} \qquad\qquad (4.1)$$

where the number of monomer N was 117, and the Kuhn segment length b was of the order of 10 Å.[65, 66]

For ssDNA, the persistence length corresponds to 3 bases, i.e. approximately 1 nm. [59-61, 67] For an 11 mer ssDNA, the gyration radius is about 8.3 Å, [68] giving an area of 216 Å^2, which is smaller than the area of PPO. Therefore, at the takeoff area, the PPO blocks began to touch each other.

If all DNA-b-PPO molecules would be located at the air-water interface at this moment and intersect with each other, they would occupy a total area of 147 cm^2, which was 91.3% of the actual area (161 cm^2) between the barriers at that moment. Thus a major part of DNA-b-PPO was situated at the air-water interface instead of being dissolved in water.

Upon further compressing the monolayer, the lateral pressure increased to 31.7 mN/m when the barriers compressed to the minimum area the trough could achieve. A tilted plateau can be seen at around 520 Å^2, indicative of a liquid expanded to liquid condensed phase transition. If 6 nmol DNA-b-PPO molecules were spread onto the air-water interface, a collapse pressure of 38.5 mN/m was observed.

During the first compressing and expanding circle, a hysteresis is observed. The takeoff area decreased to 1252 $Å^2$ in the expanding curve. The monolayer was compressed and expanded for three times more to test the stability and repeatability. The isotherms repeated themselves quite well, showing that the monolayer was stable. The maximum lateral pressure and the onsets of phase transition (640 $Å^2$) kept almost constant, while the takeoff area moved slightly to lower area per molecule region after each cycle. This can be attributed to the aggregation of DNA-*b*-PPO that remained from the previous compression.

4.1.2 Compression/expansion rate dependence of the isotherm

As the characteristics of an isotherm might also depends on the rate of compressing and expanding,[69, 70] the rate dependence of the isotherms of 1 nmol DNA-*b*-PPO was also studied. Different rates varied from 8.75 cm^2/min to 140 cm^2/min were applied during the compressing and expanding of the same monolayer (Fig. 4.2). The isotherms were quite similar to each other, so in this range of rate, the shape of the isotherms was rate independent.
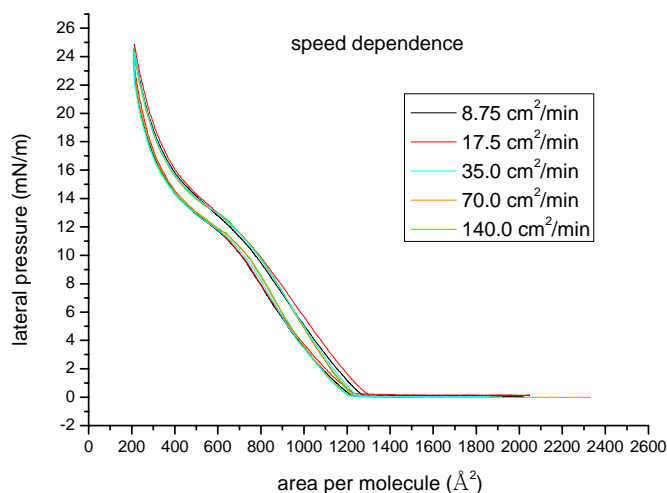

Figure 4.2 *Isotherms of the DNA-b-PPO monolayer recorded at different compressing and expanding rates.*

4.1.3 Concentration dependence of isotherms

The dependences of the takeoff area and the maximum pressure of the isotherms on the amount of DNA-*b*-PPO were summarized in Fig. 4.3.
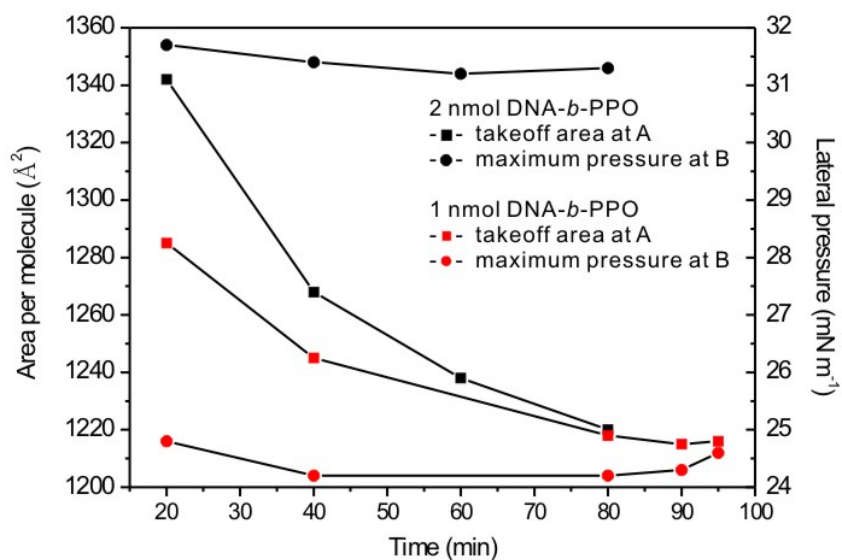
Figure 4.3 *Plots of the takeoff area and maximum pressure versus time for continuously recorded isotherms of 2 nmol and 1 nmol DNA-b-PPO. For 1 nmol DNA-b-PPO, different compression/expansion rates were used.*

For 2 nmol DNA-*b*-PPO, as an average, the takeoff area was 1267 ± 54 Å^2, and the maximum pressure was 31.4 ± 0.2 mN/m. For 1 nmol DNA-*b*-PPO, the takeoff area was 1236 ± 30 Å^2, and the maximum pressure was 24.4 ± 0.3 mN/m.

4.1.4 Stability of the monolayer at different pressures

The stability of the monolayer at different pressures was tested by monitoring the change of lateral pressure with time when the monolayer was compressed at a certain pressure. I recorded the curves at three states, at the maximum area, at the takeoff area, and at the minimum area. While recording the lateral pressure, the positions of the barriers were kept constant.

Figure 4.4 *The plot of lateral pressure versus time when the monolayer was completely expanded.*

At the maximum area, i.e., when the monolayer was completely expanded, the lateral pressure fluctuated randomly with a general trend of decreasing with time (Fig. 4.4). After 36 seconds, the lateral pressure decreased 0.033 mN/m. The decrease of lateral pressure could be caused by evaporation of water during this process. The lateral pressure could drop ~1 mN/m overnight in the closed chamber.
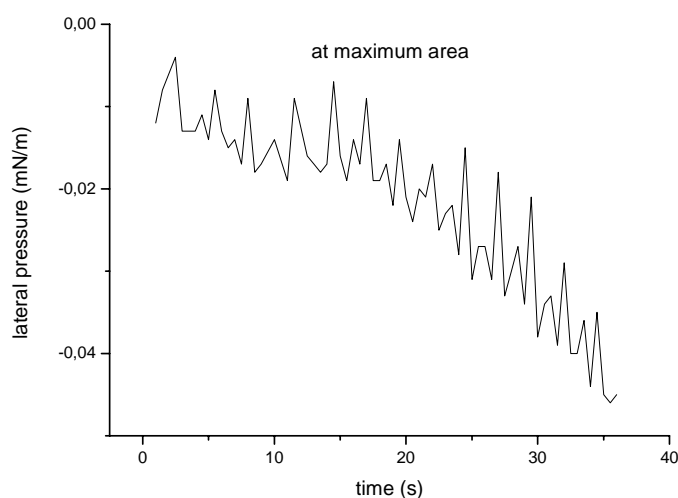
74
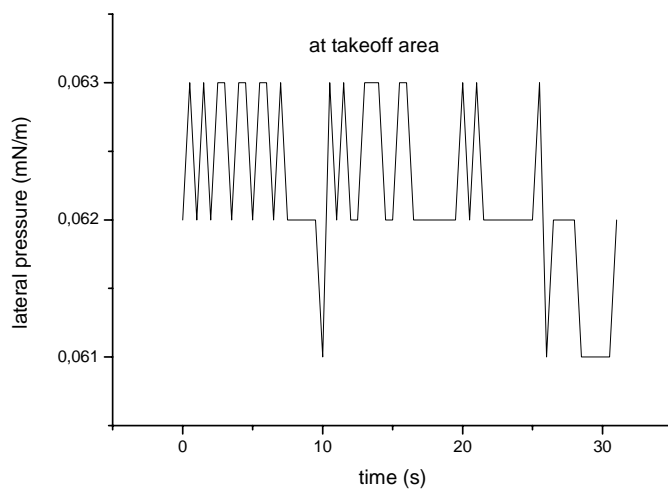
Figure 4.5 *The plot of lateral pressure versus time when the monolayer was compressed to the takeoff area.*

When the monolayer was compressed to the takeoff area, the lateral pressure fluctuated with amplitude of 0.001 mN/m in 31 seconds without a significant trend of pressure decreasing (Fig. 4.5). It implies that the lateral pressure was quite stable when the monolayer was compressed to the takeoff area. The reason could be that during this period water vapor in the closed chamber saturated, so that the water level in the trough kept constant.
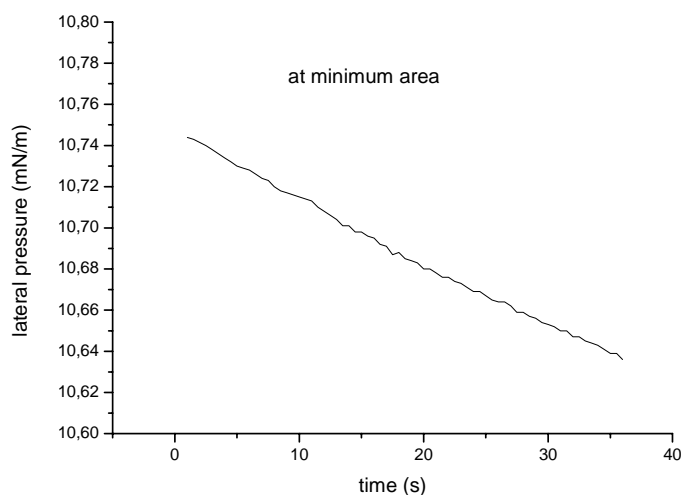
Figure 4.6 *The plot of lateral pressure versus time when the monolayer was compressed to the minimum area.*

At the minimum area, the monolayer was compressed to the maximum pressure. The lateral pressure decreased 0.107 mN/m after 36 seconds (Fig. 4.6). The decrease of pressure was more significant than that of a completely expanded monolayer. It means that such a compressed state was not stable. One possible reason is that some of the DNA-*b*-PPO molecules dived into the subphase when they were compressed at such a lateral pressure.

4.2 In-situ hybridization

In order to carry out in-situ hybridization, I reduced the amount of DNA-*b*-PPO to 0.5 nmol in the following experiments if not specially noted, so that the molecules could have enough space to hybridize. In these experiments, 0.5 nmol DNA-*b*-PPO was dissolved in 2.5 mL dichloromethane and spreaded on saline sodium citrate buffer solution to form a monolayer. I examined the hybridization processes when the monolayer was compressed to different states.

4.2.1 Hybridization at the maximum area

The isotherm of the DNA-*b*-PPO monolayer during the compressing and expanding process before hybridization was recorded (Fig. 4.7, black curve). The takeoff area appeared at 1100 Å^2. It was close to the area of the PPO segment (1256 Å^2). When the monolayer was compressed further, the lateral pressure increased as observed before.
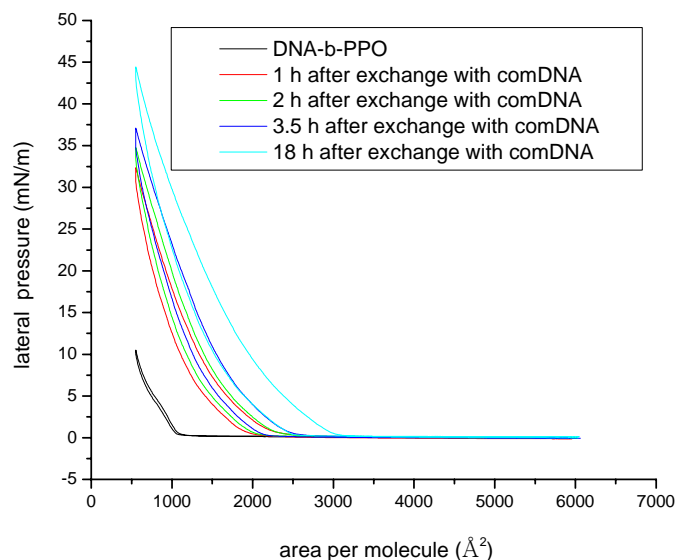
Figure 4.7 *Isotherms of the DNA-b-PPO monolayer before and after in-situ hybridization with complementary DNA at the fully expanded state.*

When the monolayer was expanded fully, comDNA strands were introduced into the trough via the subphase exchange process as described in chapter 2.3.2 and 2.3.3. This subphase exchange process took 45 min. ComDNA molecules in the subphase had to diffuse to reach DNA-*b*-PPO at the air-water interface and then hybridization could occur. Thus I recorded pressure-area isotherms after different durations (Fig. 4.7).

The maximum pressure when the monolayer was compressed to the minimum area increased. At the same time, the takeoff area moved to the high area/molecule region (3051 Å^2 after 18 h). This phenomenon was caused by the enlarged area of DNA-b-PPO after hybridization. If an ssDNA segment of DNA-b-PPO hybridizes with its complementary strand, a dsDNA segment is formed. As the persistence length of dsDNA is about 100 base pairs,[71, 72] this dsDNA is rigid and rod-like. Its length is 36.3 Å, taking 3.3 Å as the one pitch of the double helix, and the diameter of its cross section is 22-26 Å.[73] Since the takeoff area became larger than both the cross section area of dsDNA and the circular sectional area of PPO, dsDNA segments were not perpendicular to the air-water interface at the takeoff area. They must be but tilted, so that the takeoff area depended on the length of dsDNA. If we took 3051 Å^2 from the measurement as the circular sectional area of one molecule, a radius of 31.2 Å was calculated. This value was only slightly smaller than the length of dsDNA.

We found that the maximum pressure of the isotherm could increase after introducing comDNA into the subphase. However, as the barriers were at the ends of the trough, the barriers could not be driven further by hybridization. Therefore, I carried out in-situ hybridization at the minimum area and the takeoff area.

4.2.2 Hybridization at the minimum area

In order to check if hybridization could still occur when the monolayer was highly compressed, I monitored the change of lateral pressure caused by the introduction of comDNA strands into the trough while the monolayer was compressed to the minimum area (Fig. 4.8). Before subphase exchange, the pressure dropped as we observed in the stability measurement of a monolayer (Fig. 4.6).
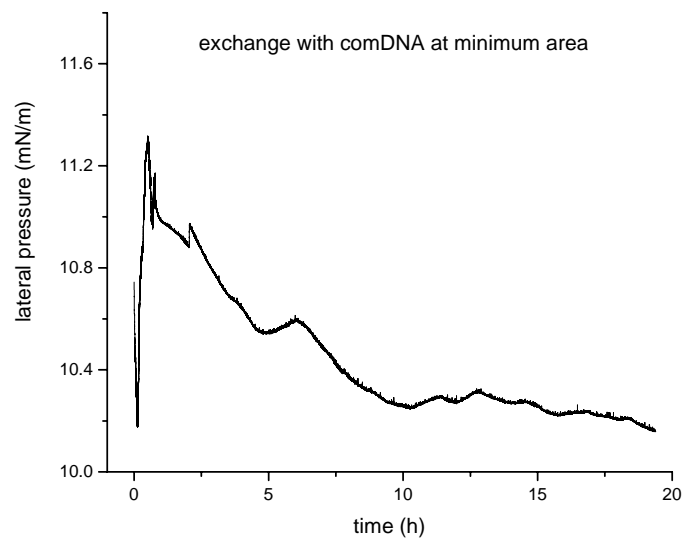
Figure 4.8 *The curve of lateral pressure versus time during and after subphase exchange with comDNA when the monolayer was compressed to minimum area.*

Even after 18 h no significant change in pressure (> 0.3 mN/m) could be observed. Thus I concluded that hybridization in a monolayer kept at lateral pressure of ~ 10 mN/m could not take place.
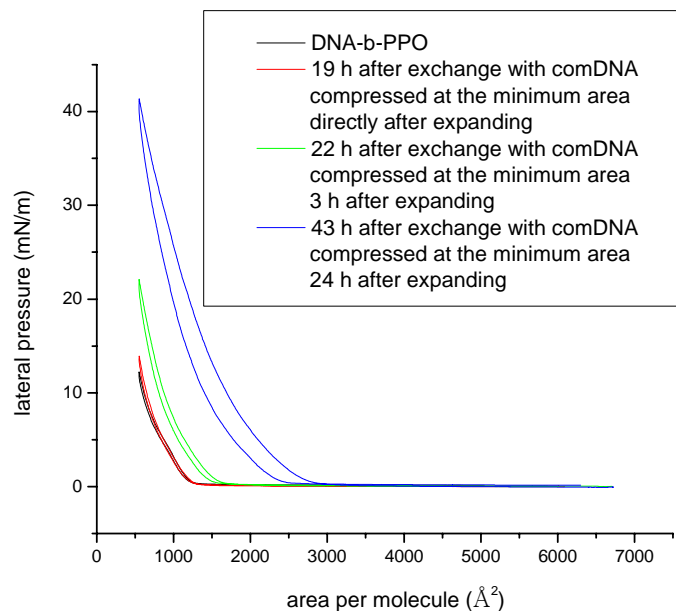
Figure 4.9 *Isotherms of the DNA-b-PPO monolayer before and after subphase exchange with comDNA containing buffer solution when the monolayer was compressed to minimum area.*

This conclusion was further supported by the isotherm recorded directly after fully expanding (Fig. 4.9, red curve), which changed little compared to the isotherm of DNA-*b*-PPO before subphase exchange (Fig. 4.9, black curve). Interestingly, the takeoff area was found to remain constant even though we assumed that some molecules dived into water when the monolayer was compressed to the minimum area. The reason could be that the molecules could go to the interface again when the monolayer was expanded.

After 3 h (Fig. 4.9, green curve) and 24 h (Fig. 4.9, blue curve), the lateral pressure increased significantly. There was no significant different in change of pressure, compared to that in Fig. 4.7. This experiment showed that hybridization was hindered when the monolayer was compressed to 10 mN/m, but occured when the monolayer was expanded subsequently.

4.2.3 Hybridization at the takeoff area

As a third experiment, I recorded the change of lateral pressure during and after subphase exchange with comDNA containing buffer when the monolayer was compressed to the takeoff area (Fig. 4.10 and Fig. 4.11).

Figure 4.10 *The curve of lateral pressure versus time in the first 450 s of subphase exchange with comDNA containing buffer solution when the monolayer was compressed to the takeoff area.*

Before subphase exchange, the monolayer was compressed to the takeoff area, when the lateral pressure already increased slightly (Fig. 4.10). The barriers were stopped there, and the onset of subphase exchange appeared as a spike in the pressure-time curve. As comDNA strands had to be pumped to the subphase in order to reach the monolayer, we found a pump time of about 200 s. In this experiment, the lateral pressure started to increase at 400 s.
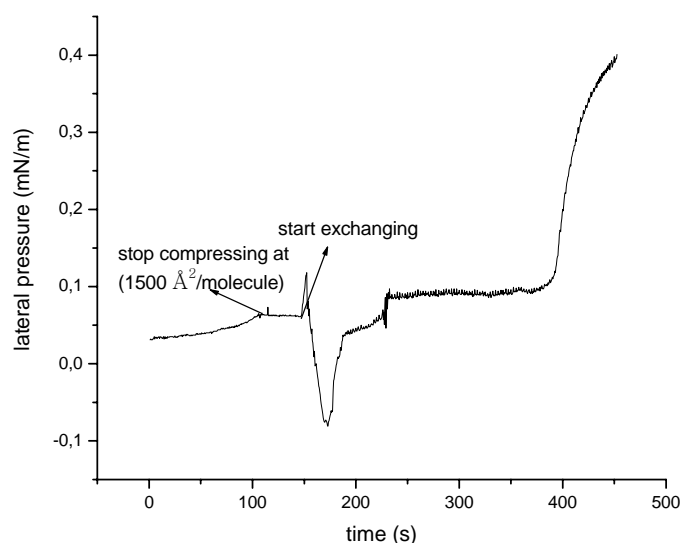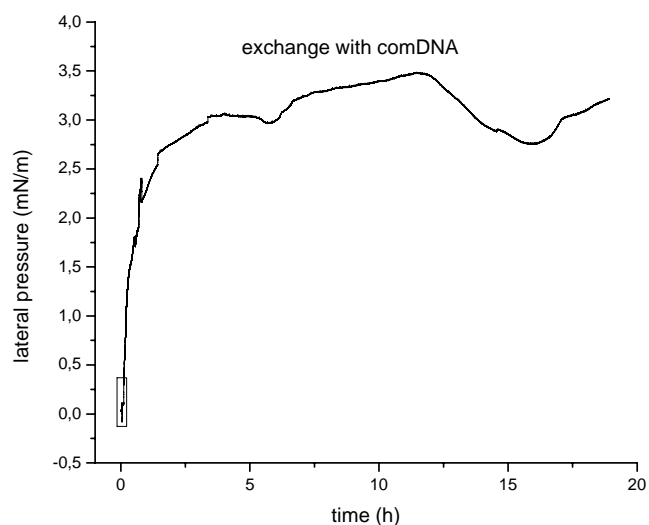
Figure 4.11 *The curve of lateral pressure versus time during and after subphase exchange with comDNA containing buffer solution when the monolayer was compressed to the takeoff area. The exchange process took the first 45 min as shown in the box.*

After 19 h, the lateral pressure increased to 3.2 mN/m (Fig. 4.11). The fluctuation of pressure in this curve was attributed to water evaporation.

The lateral pressure increased 2.9 mN/m after the first 3 h. This increase in pressure was close to that at the takeoff area 3 h after introducing comDNA into the subphase when the monolayer was compressed to 10 mN/m (3.7 mN/m, Fig. 4.9). However, when comDNA sequences were introduced while the monolayer was completely expanded, the lateral pressure increased 18.2 mN/m.
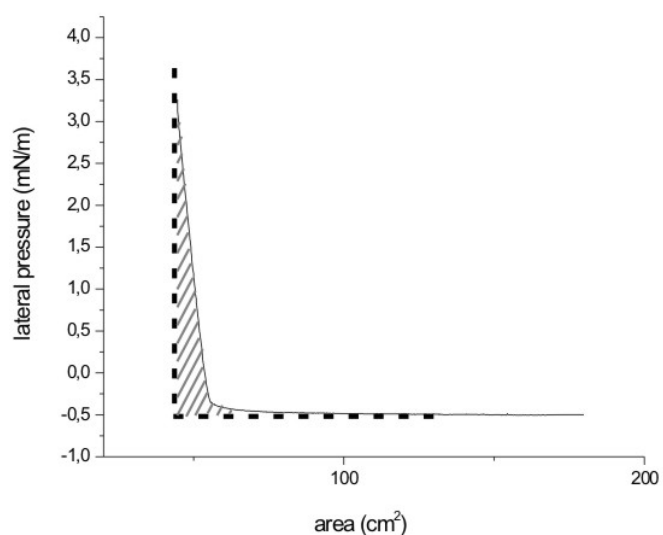
Figure 4.12 *The curve of lateral pressure versus area in the expanding process after subphase exchange.*

After following the lateral pressure for ~19 h, the monolayer was expanded completely. The curve of lateral pressure versus area was recorded (Fig. 4.12). The work the monolayer did to the barriers in the expanding process was calculated as 2.07×10^{-6} J by integrating the area below the curve and above the baseline in Fig. 4.12 with equation 4.2,

$$W = \int \pi l \, ds = \int \pi \, dA \qquad (4.2)$$

where π is the lateral pressure, l is the length of the barriers, s is the distance the barriers moved, and A is the area between the barriers. After subtracting the work the barriers did to the monolayer in the compressing process before subphase exchange from Fig. 3.18, which was 3.47×10^{-7} J, the work the monolayer did owing to hybridization was 1.72×10^{-6} J.

The average free-energy change associated with the hybridization of a complementary base pair is -78 meV (-1.8 kcal mol^{-1}) at 20 °C.[20] If we consider all the ssDNA segments in the monolayer hybridized with comDNA strands perfectly in the subphase, the energy released is 4.16×10^{-5} J. Thus, the stored energy after hybridization is 4.13% of total free energy.

As the lateral pressure increased after hybridization, the monolayer could induce a mechanical motion of the barriers. To observe barrier movements the feedback system of the Langmuir film balance was set to maintain a lateral pressure of 0.2 mN /m during the subphase exchange process for a monolayer composed of 0.6 nmol DNA-*b*-PPO (Fig. 4.13).
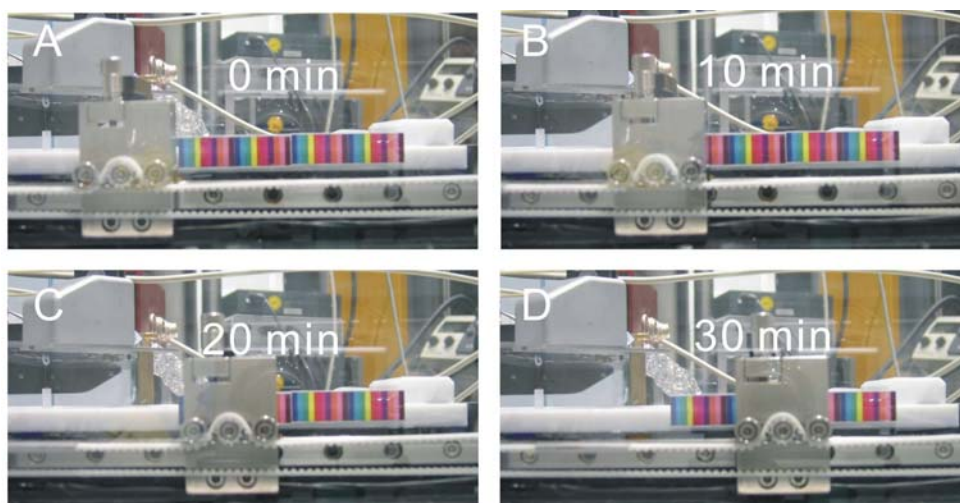
Figure 4.13 *Photographs showing the movement of barriers during the process of introducing comDNA into the subphase (from 0 min to 30 min).*

Upon exchanging the subphase with comDNA, each barrier moved 56 mm after 30 min. The work the monolayer did to the barriers was (0.2 mN m^{-1}) (lateral pressure) × (56 mm × 77 mm) (area) × 2 = 1.73×10^{-6} J. If we consider all the 0.6 nmol DNA-*b*-PPO hybridized with comDNA, the work the monolayer did in 30 min is 3.47% of the total released free energy. This value is close to the stored energy after

hybridization as determined before. It proves that the idea of realizing a DNA machine driven by hybridization of DNA-*b*-PPO in langmuir trough is feasible.
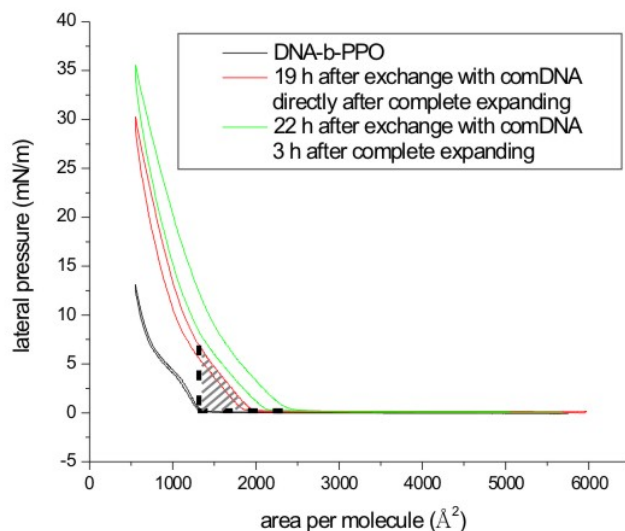
Figure 4.14 *Isotherms of the DNA-b-PPO monolayer before and after in-situ hybridization with comDNA when the monolayer was compressed to the takeoff area.*

Directly after fully expanding, the monolayer was compressed and expanded again. At the same time, the isotherm was recorded (Fig. 4.14, red curve). The maximum pressure was 30 mN/m. Afterwards, the monolayer was kept in the fully expanded state for 3 h, until the next isotherm was measured (Fig. 4.14, green curve). The maximum pressure increased to 36 mN/m. The shadowed area in Fig. 4.14 indicated the extra work the barriers did in order to compress the monolayer to the first takeoff area for each molecule. In our case, the work the barriers did per cm^2 was 3.6×10^{-8} J/cm^{-2}.

4.2.4 Comparison with hybridization of DNA coupled to lipid

As mentioned in the introduction and motivation, researchers studied lipid-DNA complexes with Langmuir film balance (Fig. 1.4). Sastry et al. also observed the increase of lateral pressure after introducing comDNA into the subphase by injection (Fig. 4.15).[74] As shown in Fig. 4.15, curves 1 and 2 were π-A isotherms recorded 1 and 12 h after spreading ODA on the ssDNA containing subphase respectively. Curve 3 was the π-A isotherm recorded 12 h after introduction of comDNA sequences into the subphase. Curve 4 was the π-A isotherm recorded 12 h after introduction of ethidium bromide intercalator into the subphase.

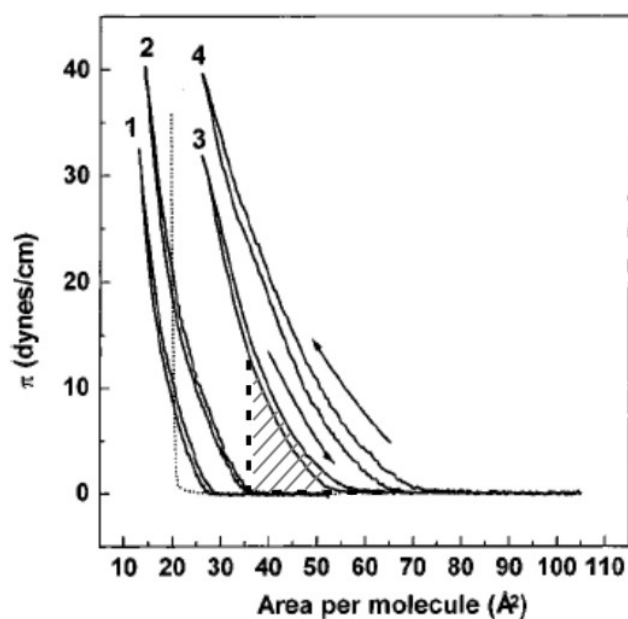**Figure 4.15** *π-A isotherms recorded from an ODA monolayer at various times after introduction of DNA/intercalator molecules into the subphase. The dotted line corresponds to the π-A isotherm recorded from an ODA monolayer on a 10^{-8} M solution of ethidium bromide in deionized water as the subphase.[74]*

We can calculate the work the barriers did per cm^2 in this experiment, which was 1.4

$\times 10^{-9}$ J/cm^{-2}. It was 3.9% of the work derived from our experiment. It means that the hybridization in our experiment was 26 times more efficient than that in an experiment with ODA monolayer-DNA complex, because DNA-*b*-PPO molecules directly located at the air-water interface and the density of ssDNA segments increased.

4.2.5 Interaction with noncomDNA

As a control experiment, a fresh monolayer was prepared, and compressed to the takeoff area. NoncomDNA strands were introduced into the trough via subphase exchange. The curve of the lateral pressure versus time was recorded during and after this subphase exchange process (Fig. 4.16). After ~19 h, the lateral pressure did not increase, but decreased slightly, which could be attributed to the evaporation of water.
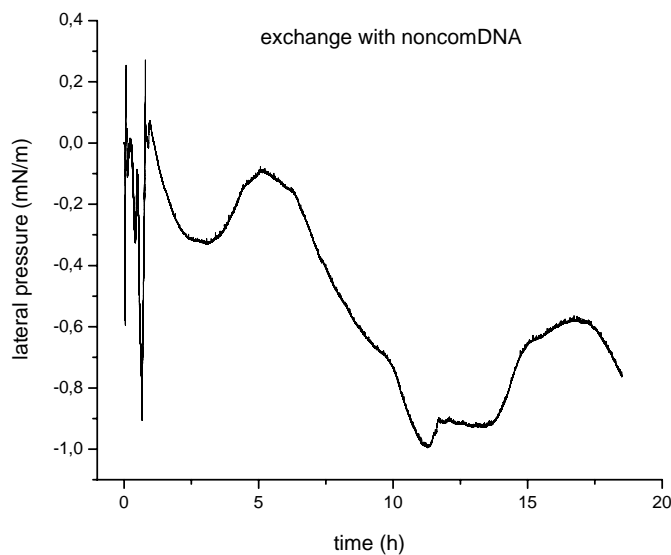
Figure 4.16 *The curve of lateral pressure versus time during and after subphase exchange with noncomDNA containing buffer solution when the monolayer was compressed to the first kink.*

An isotherm was recorded directly after this expanding process (Fig. 4.17, red curve), and the maximum pressure increased to 25 mN/m. After the monolayer was fully expanded for 3 h, another isotherm was recorded, showing a maximum pressure of 27 mN/m (Fig. 4.17, green curve).
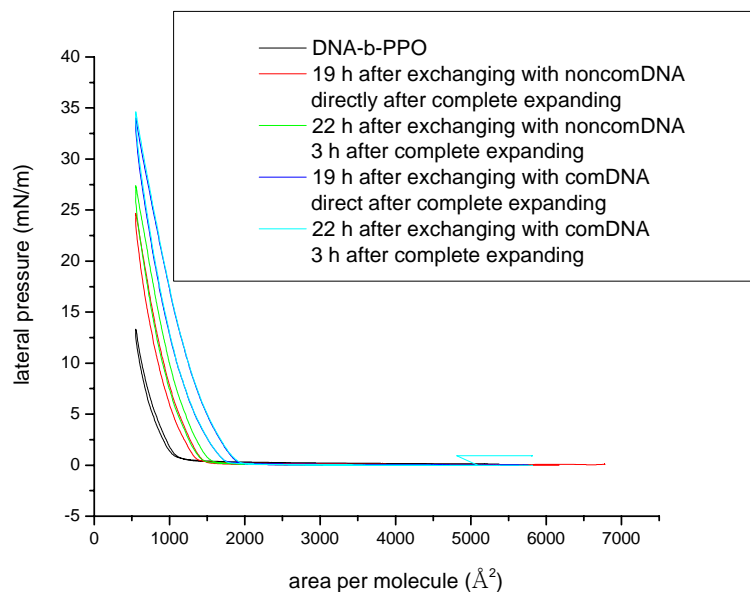
Figure 4.17 *Isotherms of the DNA-b-PPO monolayer before and after subphase exchange with noncomplementary and subsequent comDNA containing buffer solution when the monolayer was compressed to the takeoff area.*

Although the lateral pressure did not increase after subphase exchange when the monolayer was compressed to the takeoff area, the maximum pressure increased after fully expanding. There are two possible reasons for the increase in maximum pressure. Firstly, noncomDNA strands might also interact with the monolayer (Fig. 4.18). The complementarity in continuous is less than 3 base pairs, and at maximum 4 discontinuous base pairs could form. When the monolayer was compressed, it was difficult for the interaction to occur. But when the monolayer was expanded, there

was enough space for the interaction, so that the area one molecule occupied was enlarged, and the maximum pressure increased. Secondly, the influence of charges might also result in the change in shape of isotherms. As the ratio of the concentration of charges induced by noncomDNA to that induced by salts in buffer solution was 6: 10^4, the change of concentration of charges might not significantly influence the shape of isotherms. According to above argument, interaction of noncomDNA strands with the monolayer could be a possible reason that caused the increase of lateral pressure.
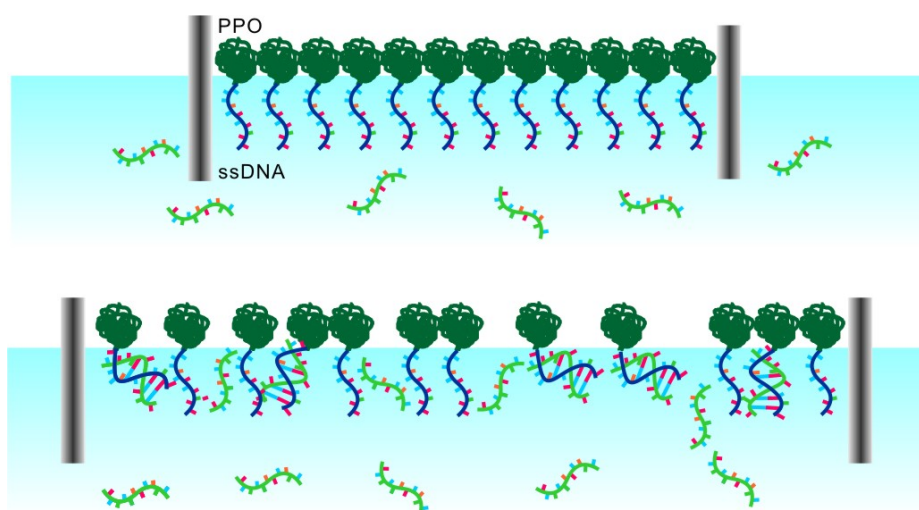
Figure 4.18 *Schematic illustration of the attachment of noncomDNA to DNA-b-PPO molecules at the air-water interface.*

In order to check if hybridization with comDNA could continue to occur in the presence of noncomDNA, comDNA strands were introduced into the trough while the monolayer was compressed to the takeoff area (1606 Å^2) after recording the isotherms (red and green curves in Fig. 4.17). The pressure increased 1.5 mN/m after ~19 h (Fig. 4.19). During the fully expanding process, the work the monolayer did to the barriers after hybridization was 2.51×10^{-7} J, which was 14.6% of the work the monolayer could do when the subphase was exchanged with only comDNA containing buffer solution. It means that although hybridization could still occur, a part of DNA-*b*-PPO

molecules had interaction with noncomDNA, and the percent of free DNA-*b*-PPO for hybridization was reduced.
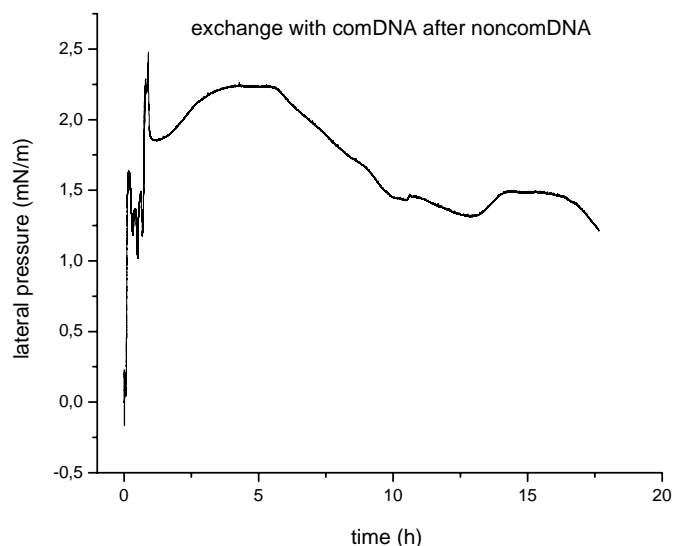
Figure 4.19 *The curve of lateral pressure versus time during and after subphase exchange with comDNA after exchange with noncomDNA when the monolayer was compressed to the first kink.*

Isotherms were recorded directly after fully expanding (Fig. 4.17, blue curve), and also 3 h later (Fig. 4.17, light blue curve). The maximum pressure increased, and the takeoff moved to high area per molecule region (1986 $Å^2$) as usual, because comDNA strands could replace the position of attached noncomDNA strands remaining in the monolayer, or hybridize with ssDNA-*b*-PPO directly.

4.2.6 Hybridization with 2 nmol DNA-*b*-PPO

The amount of DNA-*b*-PPO was increased to 2 nmol in following experiments, in order to give a relative complete overview of the isotherm of DNA-*b*-PPO after

introducing noncomDNA and comDNA into the subphase.

Figure 4.20 *Isotherms of the DNA-b-PPO monolayer before and after subphase exchange with noncomDNA containing buffer solution, and after subphase exchange with pure buffer solution.*

NoncomDNA strands were introduced into the trough via subphase exchange when the barriers were near the ends of the trough and the lateral pressure was 0 mN/m. Directly after this subphase exchange process, the lateral pressure increased to 4.5 mN/m before compressing, so the takeoff area could not be observed in this curve (Fig. 4.20). The maximum pressure increased to 50 mN/m when the monolayer was compressed to the minimum area. This increase of lateral pressure was observed as in the experiment with low amount of DNA-*b*-PPO (0.5 nmol). 20 h later, the lateral pressure increased slightly as shown by the isotherm.

After that, the subphase was exchanged with buffer solution, in order to wash away noncomDNA strands in the trough. An isotherm was measured directly after this exchange process, and the isotherm shifted little. It proves that the increase of lateral pressure was actually caused by the interaction of noncomDNA strands with the monolayer, and this interaction was stable when the subphase was exchanged with buffer solution.
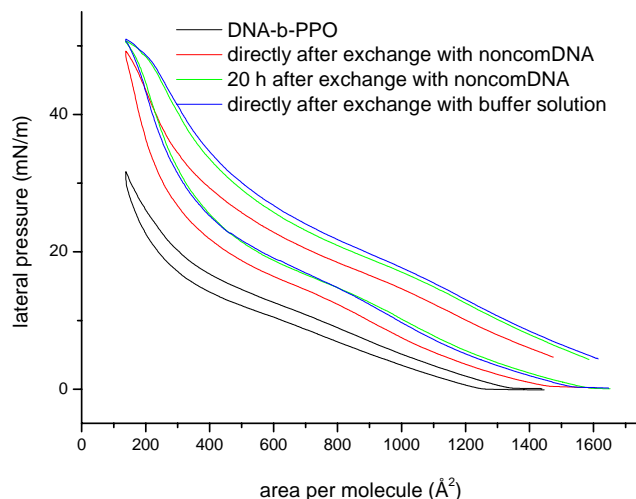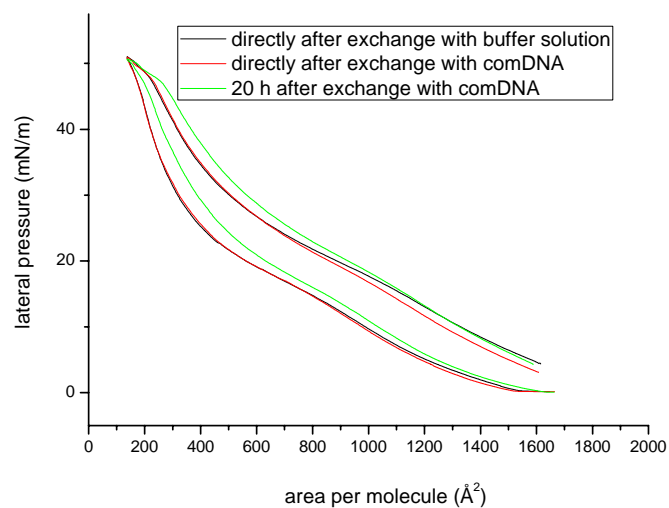
Figure 4.21 *Isotherms of the DNA-b-PPO monolayer before and after subphase exchange with comDNA containing buffer solution after subphase exchange with noncomDNA containing buffer solution and subsequent pure buffer solution.*
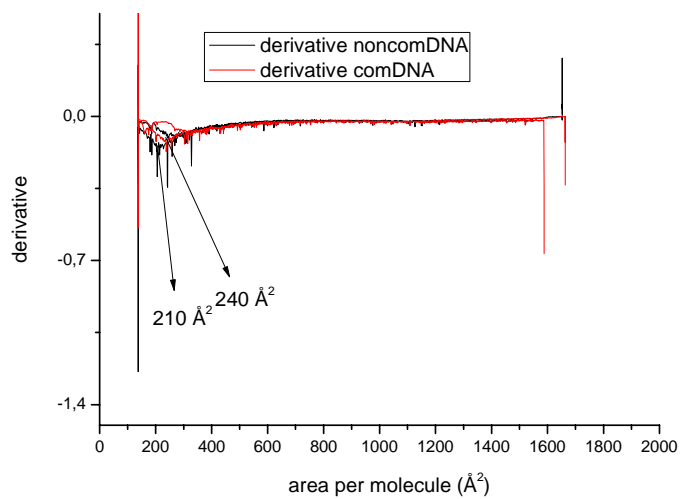
Figure 4.22 *Derivative of the isotherms after introducing noncomDNA (black curve, corresponds to green curve in Fig. 4.20) and comDNA (red curve, corresponds to green curve in Fig. 4.21) into the subphase.*

ComDNA strands were introduced into the trough afterwards. Isotherms were recorded directly after subphase exchange and 20 h later. In both cases, the maximum lateral pressure did not change. In the compressing isotherms recorded after subphase exchange with both noncomDNA and comDNA (Fig. 4.20 and Fig. 4.21), we can observe the appearance of a kink around 47.5 mN/m. The kink was at 210 $Å^2$ 20 h after introducing of noncomDNA into the trough, which was close to the circular area of ssDNA. and moved to 240 $Å^2$ 20 h after introducing of comDNA (Fig. 4.22). The appearance of these kinks could be caused by the formation of multilayers at a high lateral pressure (Fig. 4.23). As comDNA strands could hybridize with the DNA segments of DNA-*b*-PPO to form double helixes, the enlargement of size was more significant, and the kink moved to higher area/molecule region.
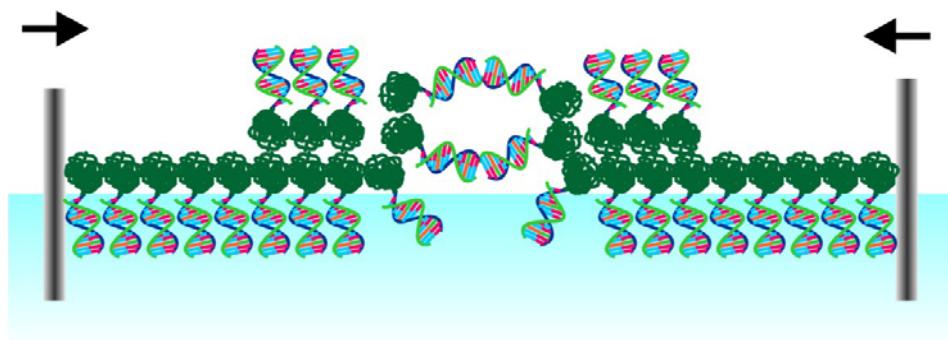
Figure 4.23 *Schematic illustration of the formation of multilayers at the air-water interface whent the lateral pressure was high enough.*

4.2.7 In-situ hybridization by injection of DNA solution

As the size of the langmuir trough I used in above experiments was small, and the gaseous state could not be observed (Fig. 4.20 and Fig. 4.21), I tried to use a bigger trough (1155 cm×64 cm). This trough was not equipped with subphase exchange system, but it was still possible to carry out in-situ hybridization by injection of DNA solution into the subphase. The gap between the barriers and the bottom of the trough

was wide enough that the needle of a syringe could be inserted from the pure subphase area to the subphase covered by the monolayer (Fig. 4.24).
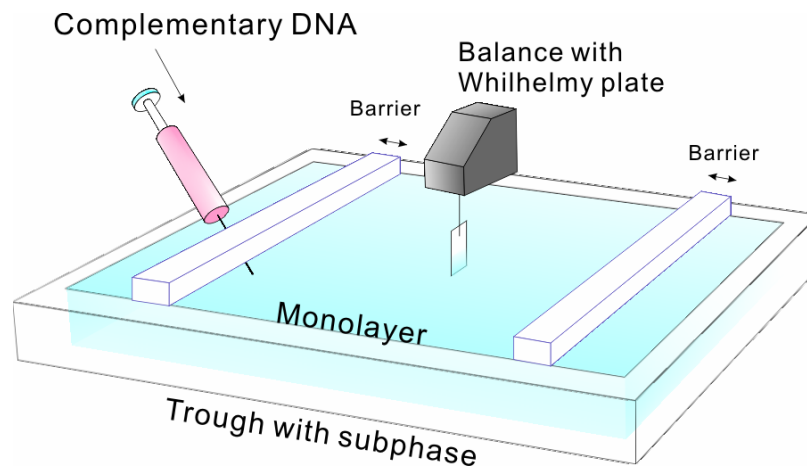
Figure 4.24 Cartoon of the *setup of a Langmuir film balance for in-situ hybridization by injection of DNA solution.*

1 nmol DNA-*b*-PPO was spreaded onto 1 mM NaCl solution in the same way as described before. The isotherm during the compressing process was determined (Fig. 4.25, black curve). 500 nmol noncomDNA was dissolved in 5 mL 1 mM NaCl solution. After removing 5 mL subphase from the pure subphase area (the area out of the barriers), noncomDNA solution was injected into the subphase covered by the monolayer (the area between the barriers). After expanding the monolayer completely, compressing isotherms were recorded some hours later (Fig. 4.25). Similarly, comDNA was injected into the subphase, and compressing isotherms were measured (Fig. 4.25).
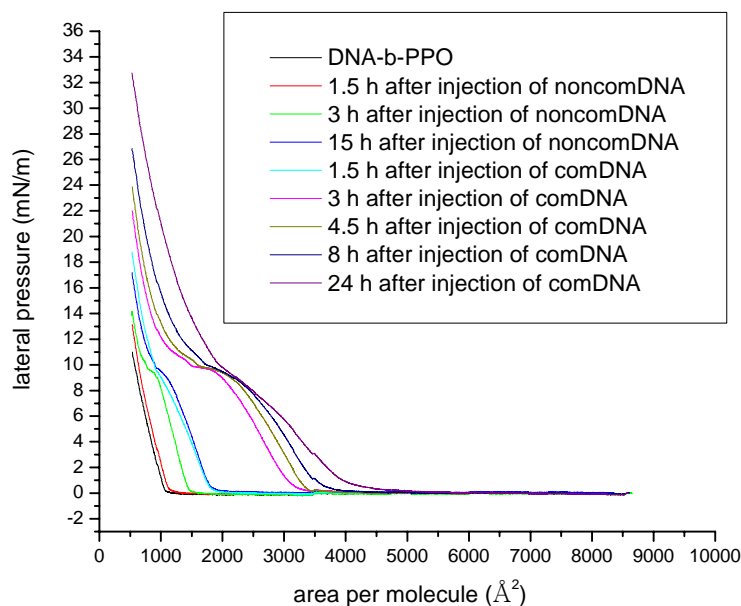
Figure 4.25 *Compressing isotherms of the DNA-b-PPO monolayer before and after injection of noncomDNA and comDNA containing buffer solution.*

Similar to the experiments carried out with subphase exchange, the lateral pressure increased after introducing of noncomDNA and comDNA into the subphase. The takeoff area also moved to the larger area per molecule region correspondingly. However, after the injection of comDNA, the takeoff area moved to much higher area per molecule than that in the experiment with subphase exchange. For example, the takeoff area was 2500 Å^2 3.5 h after subphase exchange with comDNA containing buffer, while it was 3400 Å^2 3 h after injection of comDNA into the subphase. The reason is that comDNA strands were injected without the removing of noncomDNA and lost of comDNA during subphase exchange, so that the final concentration of DNA molecules in the trough was higher than that in the trough couples with subphase exchange system. More DNA molecules could attach to DNA-*b*-PPO molecules, so the area at which the molecules began to touch each other increased.

The drawback of in-situ hybridization by injection is that we can not compare the hybridization process with comDNA and noncomDNA for the same monolayer, as they would coexist in the trough with large amounts. Another problem is the change of measured lateral pressure (~ 2 mN/m) caused by the removing of subphase and injection of DNA solution. This change in water level made the observation of change in lateral pressure resulted by hybridization difficult.

4.3 Thin films prepared by LB technique

In addition to the study aggregations and structures of DNA-*b*-PPO in the monolayer, I transferred thin films to different substrates using the Langmuir Blodgett (LB) technique. The morphology of these films were studied with AFM.

4.3.1 Double layers transferred to HOPG

At first, double layers of DNA-*b*-PPO were transferred to freshly cleaved highly ordered pyrolytic graphite (HOPG) at different lateral pressures as shown in Fig. 4.26. In this isotherm, the takeoff area was smaller than 1200 Å^2 as we observed before. The reason could be that the amount of DNA-*b*-PPO molecules was not accurate enough, or the lost of material during spreading was significant.
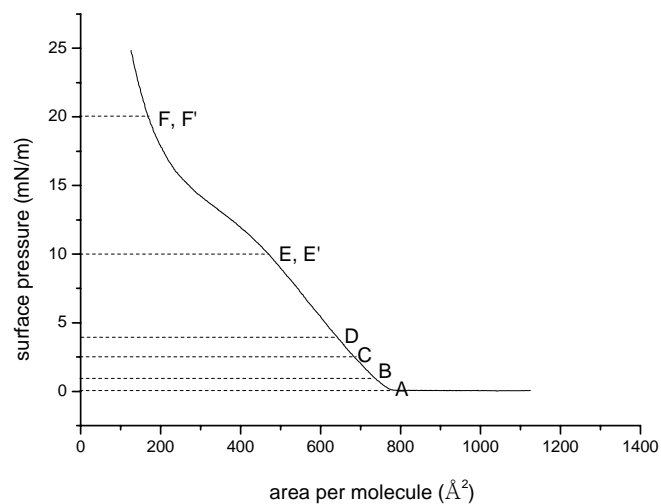
Figure 4.26 *Compressing isotherm of the DNA-b-PPO monolayer showing pressures for double layer transferring.*

The substrate was immersed vertically into the subphase at a constant speed of 2 mm/min, and then withdrawn from the subphase at the same speed (Fig. 2.11). During this process, the lateral pressure was kept constant by moving the barriers automatically. When the substrates were completely dry, they were investigated with AFM in tapping mode under ambient environmental conditions (Fig. 4.27).
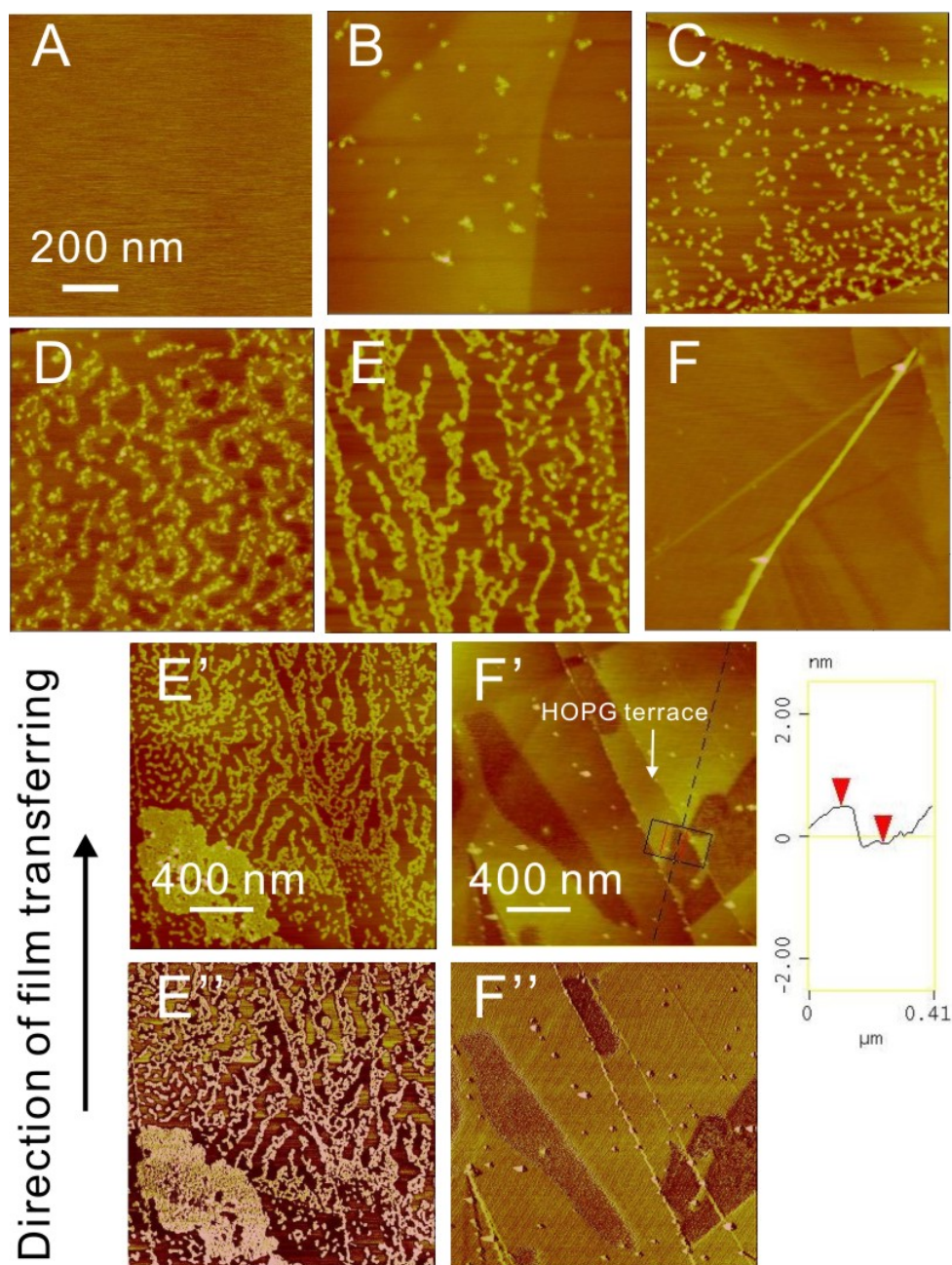
Figure 4.27 *Tapping mode AFM topographical images of the HOPG substrates after double layer transferring at (A) 0 mN/m, (B) 1 mN/m, (C) 2.5 mN/m, (D) 4 mN/m, (E, E') 10 mN/m, and (F, F') 20 mN/m. For (A-F), the lateral scale is 200 nm, and the height scale is indicated with a color bar (5 nm). For (E'-F''), the lateral scale is 400 nm. Phase images of E' and F' are E'' and F'', respectively. The phase scale is also indicated with a color bar (5°). The direction of film transferring is shown by the arrow.*

At 0 mN/m, there is no special structure on the transferred substrate. On the substrate after film transferring at 1 mN/m, sparsely distributed particles or balls are observed. The height of these domains is 1.2 ± 0.4 nm. The observation of these particles is a hint for the formation of aggregations by DNA-*b*-PPO molecules in the former compressing-expanding cycle. For the film transferred at 2.5 mN/m, domains with higher density are observed with a height of 1.3 ± 0.3 nm. When the pressure increased to 4 mN/m, the density of the domains increased further, and some of them connected to each other to form linear structures. The height of these structures is about 1.4 ± 0.3 nm. On the substrate after film transferring at 10 mN/m, fractal structures with a height of 2.2 ± 0.3 nm formed. These fractal structures oriented toward the direction of film transferring. At 20 mN/m, a smooth surface was observed on the substrate.

Three different mechanisms of formation of block copolymer surface aggregates at the air-water interface have been proposed: (i) deposition of micelles in solution; (ii) spontaneous surface aggregation at the onset of deposition of polymer solution; (iii) compression-induced surface aggregation.[75] Since no special structure was observed on the substrate transferred at 0 mN/m, we can preclude the first two possibilities. The structures formed on the substrates at higher pressures were induced by compression. Before compression, the concentration of molecules on the surface was so low that single molecules distributed sparsely on the air-water interface, and no structure was observed on the film transferred at 0 mN/m. When the monolayer was compressed to a certain extent that DNA-*b*-PPO molecules began to touch each other, aggregates formed and could be transferred to substrates. It can be proven by the AFM images, in which the shape and size of domains were nearly unchangeable in the range of lateral pressures from 1 to 4 mN/m, while the coverage of the domains increased from 1.2% to 17.7%. Aggregates formed during this range of lateral pressure, and their concentration increased with lateral pressure.

The height of aggregates was about 1.3 nm, even smaller than the theoretical length of a ssDNA-*b*-PPO (5.7 nm). The reason could be that at such low lateral pressures, the aggregates were not closely packed on the air-water interface, and they lay on the substrate during transferring. In addition, drying in air and the force applied on the domains during AFM imaging could also reduce the measured height. On the film transferred at 10 mN/m, the height of domains increased to 2.2 nm, because the monolayer was more closely packed. The coverage of the fractal structure was 29.6%. For the film transferred at 20 mN/m, I propose that a compact layer formed on the substrate.
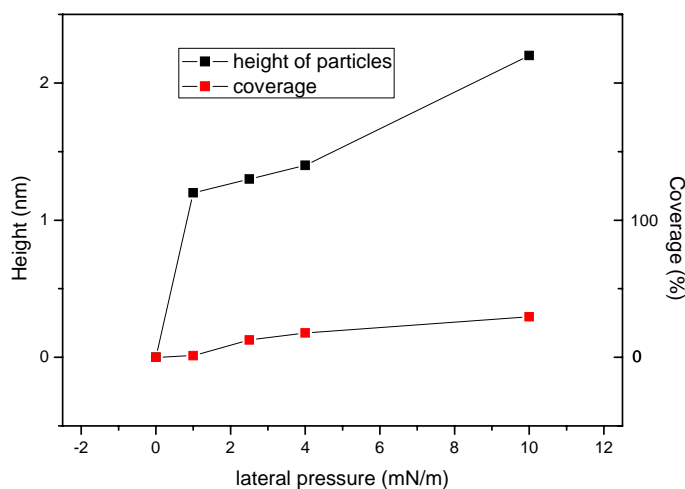
Figure 4.28 *The plots of height of particles and coverage of the transferred films versus lateral pressure.*

As we know, the phase image records changes of the oscillator phase delay relative to the excitation signal,[76] so that the phase contrast corresponds to differences in stiffness, viscoelasticity, or chemical composition. For thin films with nanoscale thickness, the surface height difference should have little effect on the phase lag. When the phase image is obtained by soft tapping mode and the phase contrast is high, the phase image of the thin film can reflect the difference of surface properties. [77] Thus, the origin of the phase lag should be mainly due to the interaction between the

sample and the tip, such as adhesion, dissipation, and indentation.[78-81] On another AFM image obtained from the film transferred at 20 mN/m (Fig. 4.27 F'), we could find some areas with lower height, which were about 0.6 nm lower than the majority area. On the phase image, these areas show different contrast compared to other areas. It might be a hint that the lower areas were not completely covered by the molecules to form a double layer. At such a lateral pressure, DNA-*b*-PPO molecules were highly stretched, and they might be transferred to HOPG lying on the surface. Combined with the drying effect and the force exerted during scanning, the height of a single layer could be only about 0.6 nm.

The terraces of HOPG were observed in the height topography (Fig. 4.27 F'), with a step height of 0.35 nm, which was consistent with the theoretical value [82]and the reported value measured by AFM.[83] As there is no phase contrast between these terraces, the difference in both height and phase in Fig. 4.27 F' should be caused by difference in deposited material on the surface.

Further evidence for the formation of compact layer comes from Fig. 4.27 E', which shows a densely packed domain with a height of 2.5 nm on the film transferred at 10 mN/m. It means that a compact layer with small sizes already existed in some areas of the film transferred at 10 mN/m. However, at such a pressure, DNA-b-PPO molecules still located at the air-water interface in the form of aggregates. I proposed a model for the LB transferring of DNA-b-PPO molecules to HOPG based on above observations (Fig. 4.29).
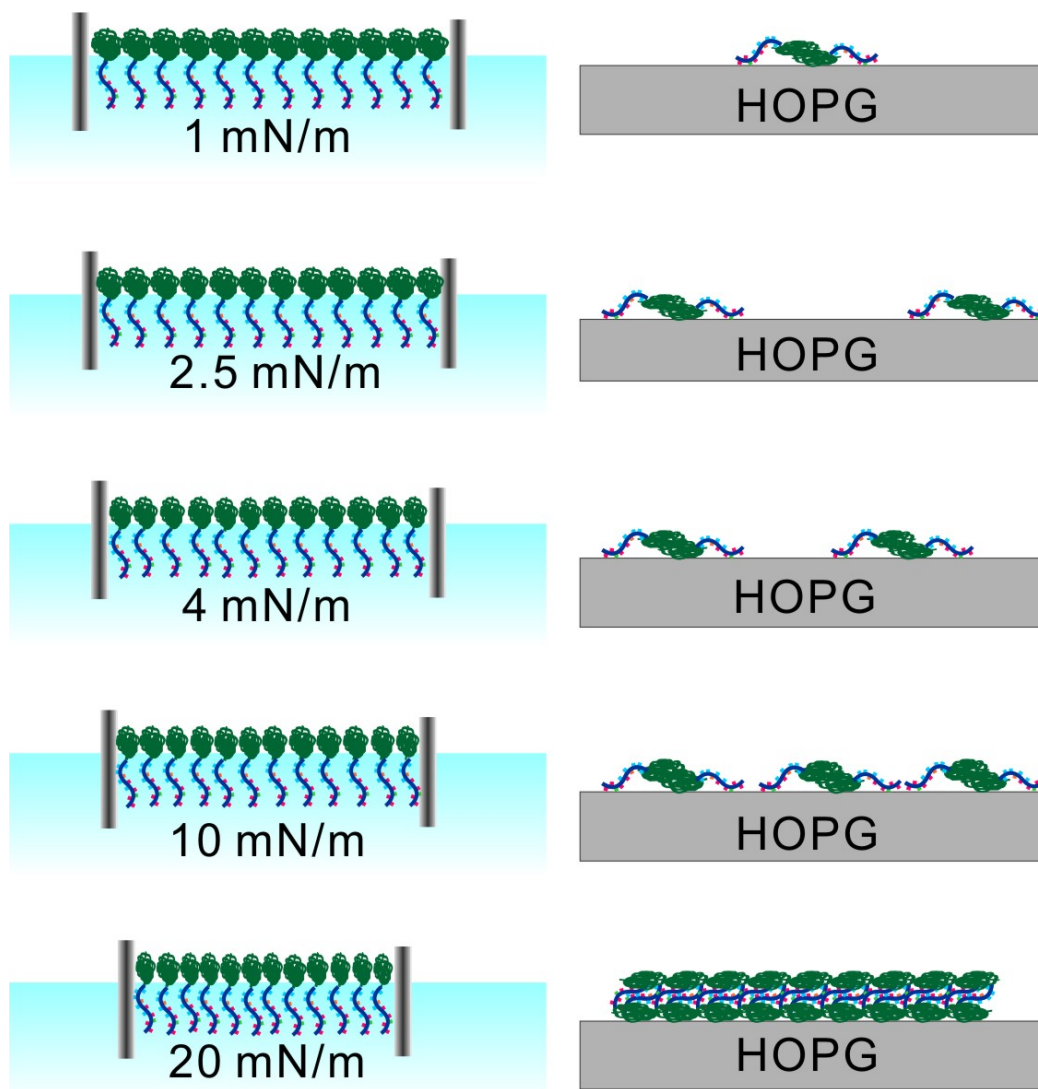
Figure 4.29 *Cartoon of the organisation of DNA-b-PPO molecules at the air-water interface and on HOPG substrates after double layer transferring.*

4.3.2 Single layers transferred to HOPG

The films mentioned above were transferred in such a way that a double layer of molecules was expected to form. In order to check the thickness of a monolayer, I immersed a HOPG substrate into the subphase covered by DNA-*b*-PPO molecules at a pressure of 2.5 mN/m with a speed of 2 mm/min. Afterwards, the molecules were

sucked away from the interface by a tube connected to an external pump, while fresh Milli-Q water was added to the bare subphase at the same time. In this way, DNA-*b*-PPO molecules were removed completely, and then the HOPG substrate was withdrawn from the subphase.
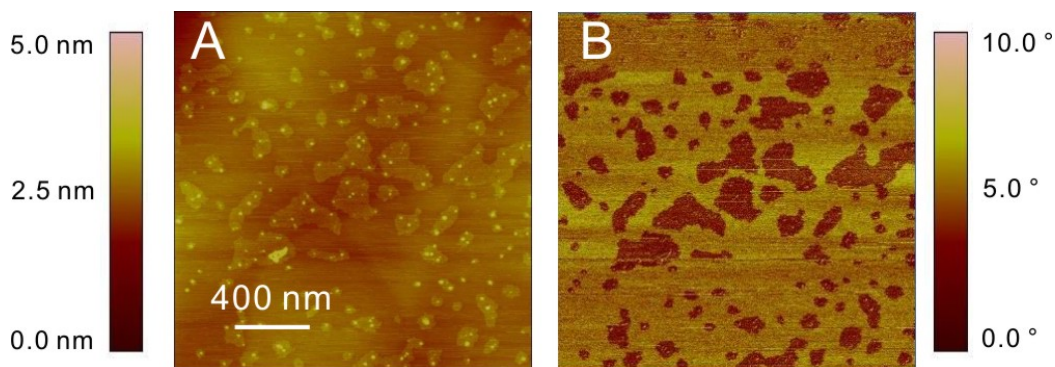
Figure 4.30 *Tapping mode AFM topographical (A) and phase (B) images of the HOPG substrates after single layer transferring at 2.5 mN/m. The lateral scale is 400 nm.   The height scale is 5 nm, and the phase scale is 10°.*

The monolayer was then imaged by AFM after drying in ambient conditions overnight (Fig. 4.30). Islands with a height of about 0.5 nm were observed. There were higher regions located on the islands with a height of 1.6 nm. I suggest that the islands were monolayers of molecules, whose height was close to that of the absent monolayer in Fig. 4.27 F'. The monolayer was hydrophilic, so it showed phase contrast with respect to HOPG substrate. The higher regions might correspond to double layers formed in the process of withdrawing because not all DNA-*b*-PPO molecules could sucked away.

4.3.3 Double layers transferred to HOPG after in-situ hybridization

After hybridization with comDNA in 1 mM NaCl containing subphase, double layers were transferred to HOPG substrates at different pressures (Fig. 4.31), and investigated with AFM in tapping mode as illustrated in Fig. 4.33.
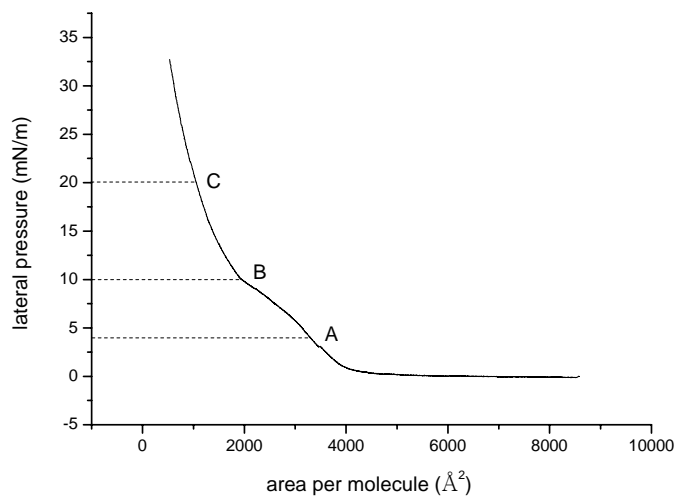
Figure 4.31 *Compressing isotherm of the DNA-b-PPO monolayer after in-situ hybridization showing pressures for double layer transferring.*

For the film transferred at 4 mN/m, the height of the fractal structures was about 0.6 nm, and the height of the bright border was about 1.2 nm. The coverage of these structures was 62.4%. For the film transferred at 10 mN/m, the height of the bright islands was about 1.8 nm, and the height of the relative dark part in the islands was about 1 nm. The coverage of the islands was 16.4%. At 20 mN/m, we can observe network structure with a height of 1.7 nm. The size of the holes was about 100 nm, and the coverage of the network structures was 62.8%.
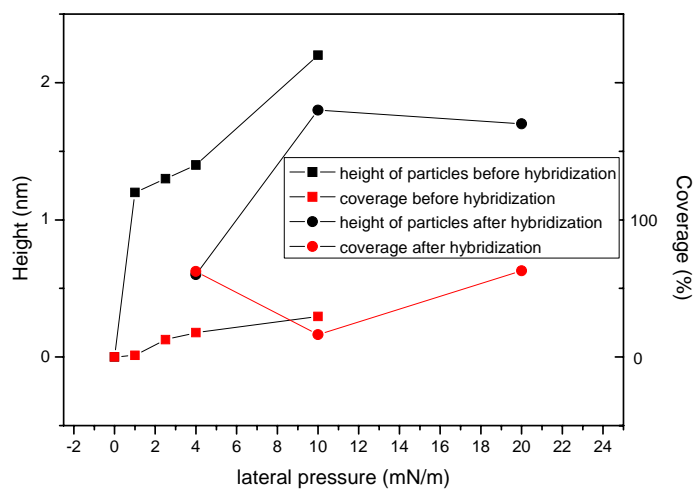
Figure 4.32 *The plots of height of particles and coverage of the transferred films versus lateral pressure before and after in-situ hybridization.*
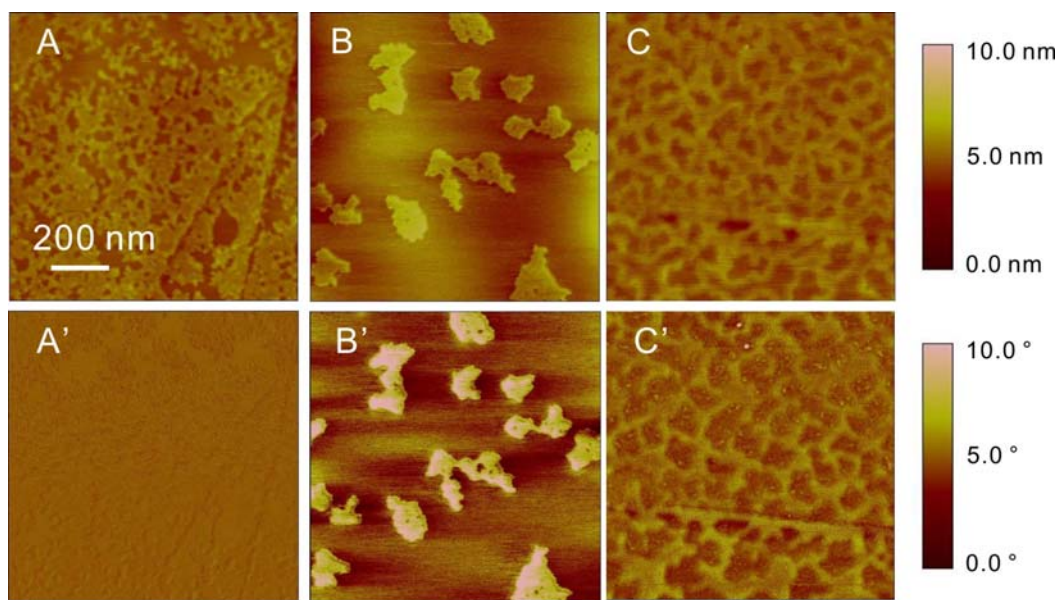
Figure 4.33 *Tapping mode AFM topographical images (A-C) and phase images (A'-C') of the transferred double layers to HOPG substrates after in situ hybridization at (A) 4 mN/m, (B) 10 mN/m, and (C) 20 mN/m. The lateral scale is 200 nm. The height and phase scales are indicated with color bars.*

Obviously, the structures formed on HOPG substrates after in situ hybridization were different from those formed before hybridization. At 4 mN/m, instead of particles, fractal structures with much higher coverage aggregated on the surface. The height of the fractal structure was close to the height of a monolayer before hybridization. At the border of these fractal structures, the height doubled, indicating of a double layer. There are two possible reasons for the formation of fractal structures instead of micelles. Firstly, after hybridization, the molecules had larger size, which made them closer to each other and therefore interact with each other. Secondly, the electrostatic repulsion between DNA segments could be screened by charges of NaCl. For the film transferred at 10 mN/m, the height of surface aggregates increased, while the coverage reduced. It means that under this pressure, the formation of double layer during transferring was preferred. When the pressure increased to 20 mN/m, the density of molecules in the air-water interface was so high that the islands coalescenced to form networks. The phase contrasts in Fig. 4.33 A'-C' also implied the formation of a monolayer at 4 mN/m, and the formation of a double layer at 10 mN/m and 20 mN/m. A proposed model for the LB transferring of DNA-*b*-PPO to HOPG after in-situ hybridization is shown in Fig. 4.34.

Figure 4.34 *Cartoon of the organisation of DNA-b-PPO molecules at the air-water interface after in-situ hybridization and on HOPG substrates after double layer transferring.*

4.3.4 Single layers transferred to mica after in-situ hybridization

In addition to hydrophobic HOPG substrates, I also transferred films to freshly cleaved mica sheets. Since mica sheets are hydrophilic, I immersed them vertically into the subphase at 0 mN/m before compressing, and then removed them at a constant lateral pressure with a speed of 2 mm/min. In this way, a monolayer was expected to form on the surface.
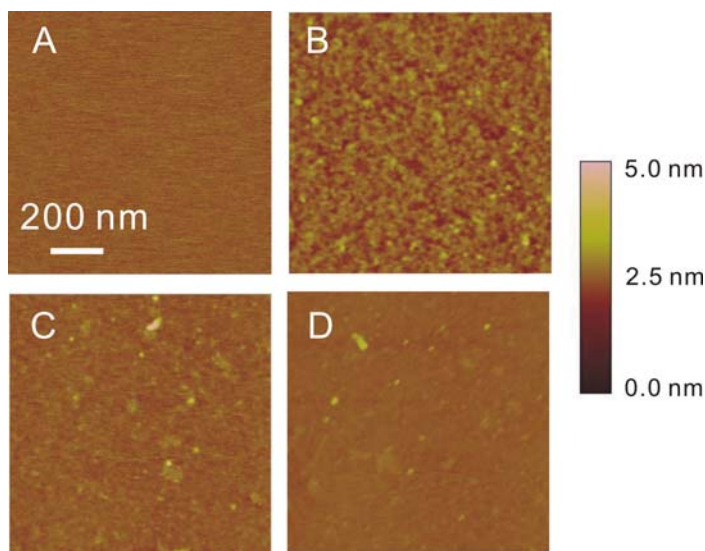
Figure 4.35 *Tapping mode AFM topographical images of the films transferred to mica at (A) 0 mN/m, (B) 4 mN/m, (C) 10 mN/m,, and (D) 20 mN/m. The lateral scale is 200 nm, and the height scale is indicated with a color bar (5 nm).*

On the substrate after transferring at 0 mN/m, no structure was observed, similar to the phenomenon observed with the HOPG substrate. For the film transferred at 4 mN/m, felt-like structures covered the surface with a height of 0.7 ± 0.2 nm. The roughness of the image was 0.24 nm. At 10 mN/m, the transferred film seemed to cover the substrate completely, with a roughness of 0.17 nm. When the pressure increased to 20 mN/m, a smoother surface was observed with a roughness of 0.16 nm. Compared to the films transferred to HOPG, the films on mica covered the substrates at relatively lower pressure, and gave rise to more homogenous surfaces. This difference is presumably due to the better wettablity of mica for aqueous solution.

The thicknesses of the films transferred at 10 mN/m and 20 mN/m were measured by making scratches on the surface. The scratches were made by disabling the slow scan axis during AFM imaging and enabling interleave mode (lift). Fig. 4.36 shows the measured thickness when different lift height was used.
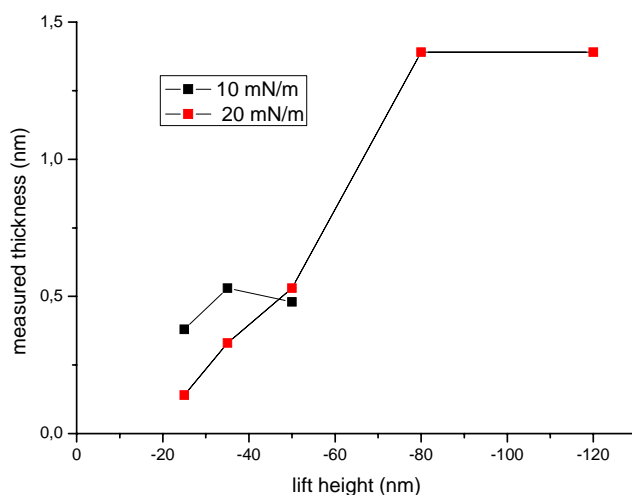
Figure 4.36 *The dependence of the measured thickness on the lift height for making scratches on the films transferred at 10 mN/m (black square) and 20 mN/m (red square).*

For the film transferred at 10 mN/m, the thickness was around 0.5 nm. This value was consistent with the thickness of the monolayer observed on HOPG substrates. In the same way, I measured the thickness of the film transferred to mica at 20 mN/m. The thickness was 1.4 nm. This increase in thickness was resulted from the more vertical alignment of the molecules at the air-water interface at higher lateral pressure. Interestingly, the depth of the scratch achieved by setting the same lift height was less than that achieved with the film transferred at 10 mN/m. It implies that the film was more compactly formed at higher lateral pressure, so that the formed film had higher stiffness. Similarly, a model of LB transferring to mica is shown in Fig. 4.37.
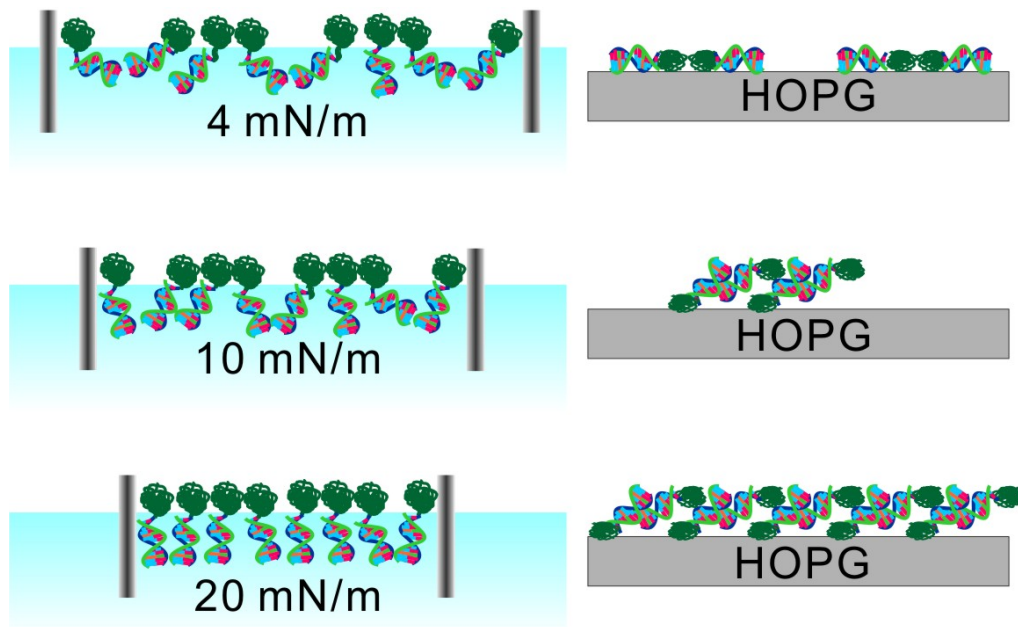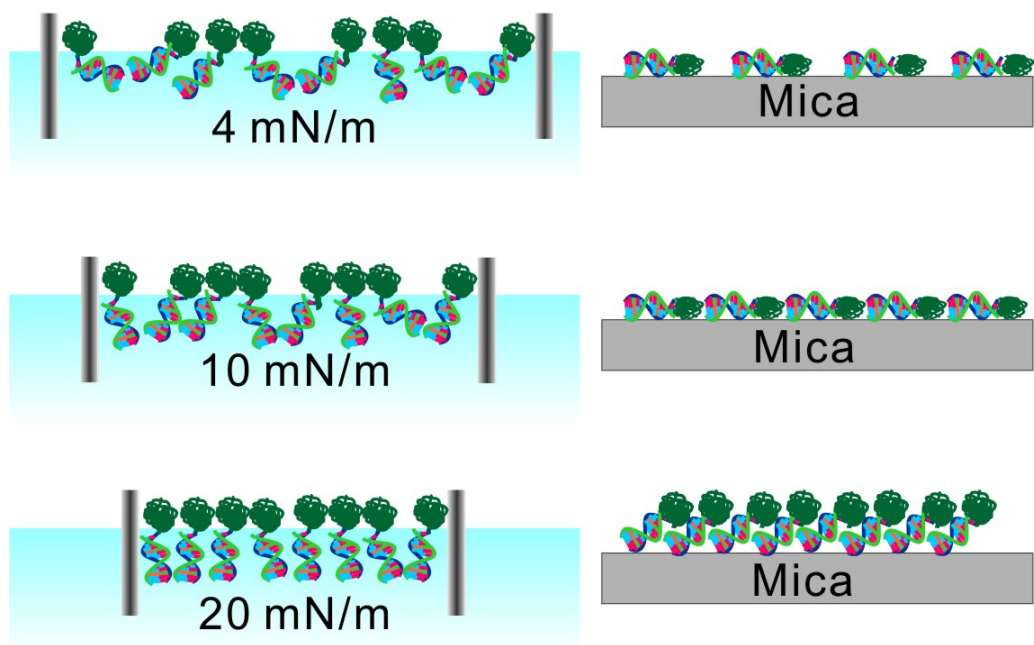
Figure 4.37 *Cartoon of the organisation of DNA-b-PPO molecules at the air-water interface after in-situ hybridization and on mica substrates after single layer transferring.*

Based on above observations and arguments, we found that AFM measurements of the films transferred by LB techniques could help us to understand the organisation of molecules at different lateral pressures. At the same time, the pressure-area isotherms could provide important information about the distribution of molecules before transferring.

Chapter 5

New molecules, new morphologies

5.1 DNA multiblock copolymer synthesized by PCR

By employing ssDNA entities as building blocks, linear double stranded triblock architectures were assembled by hybridization. Although this method provided complex well-defined block copolymer topologies, a synthetic limitation remains regarding the nucleic acid segments. The ODNs were generated by solid-phase synthesis therefore the lengths of these segments were limited to several tenths of nucleotides. This is rather small in comparison to naturally occurring polynucleotides like genomic or plasmid DNA. Fikri E. Alemdaroglu in MPIP overcomed this synthetic limitation by employing the polymerase chain reaction (PCR) for the preparation of high molecular weight DNA multiblock copolymer architectures with extended dsDNA segments.

The triblock copolymer primer was synthesized using a DNA synthesizer with a bisphosphoramidite PEG polymer as the key intermediate. Onto the central PEG domain (Mn = 2000 g/mol, PDI = 1.1) two identical ss ODNs were attached (22mer, sequence: 5'-CCTCGCTCTGCTAATCCTGTTA-3', Mw: 6670 g/mol). Employing the triblock copolymer primer as backward primer, conventional ODNs as forward primers, the plasmid (pBR322) as the template in the PCR process resulted in triblock copolymers of type dsDNA-*b*-PEG-*b*-dsDNA exhibiting nucleic acid units with lengths of 225 and 500 base pairs (bp).
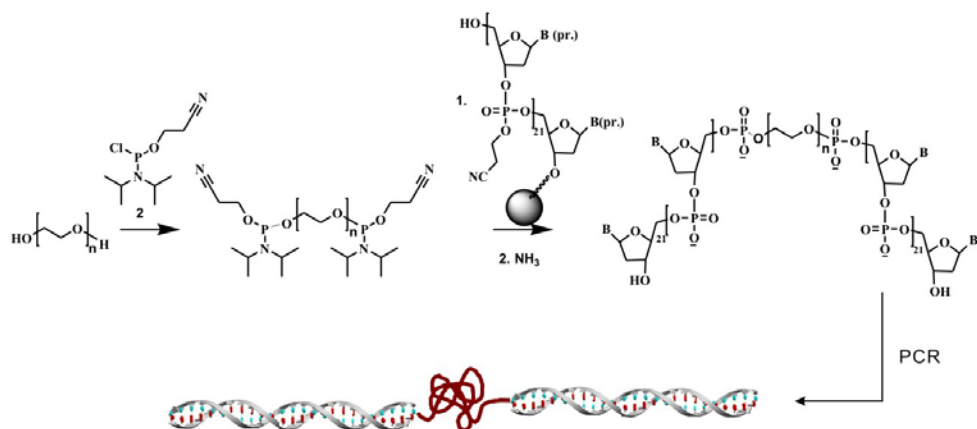
Figure 5.1 *Schematic representation of the generation of DNA triblock copolymer by polymerase chain reaction.*

Significant extension of the nucleic acid segments allows direct visualization of single block copolymers by atomic force microscopy.[84] The following images were obtained in buffer solution by AFM in soft tapping mode.
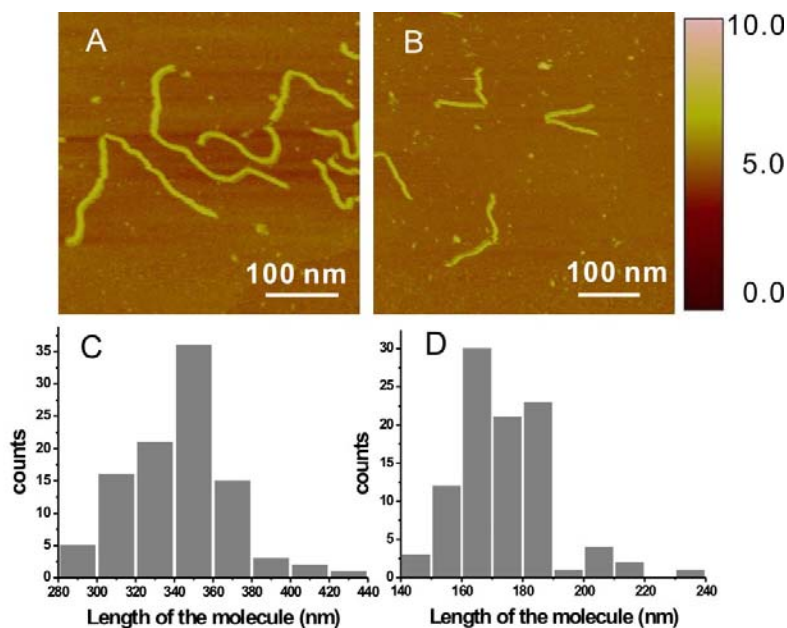
Figure 5.2 *Structural properties of DNA (500 bp)-b-PEG-b-DNA (500 bp) (A, C) and DNA (225 bp)-b-PEG-b-DNA (225 bp) (B, D) molecules investigated by AFM. (A, B) Tapping mode AFM topographical images in buffer. The height is indicated with a color scale bar on the right. The z-scale of the images is 10 nm. (C, D) Histograms of contour length distribution.*

A mean contour length of 344 ± 22 nm was measured for DNA(500 bp)-*b*-PEG(2K)-*b*-DNA(500 bp) as an average from 100 polymer molecules. This yields a rise per bp of 0.34 ± 0.02 nm which is in good agreement with the expected value for dsDNA measured by crystallography.[85] Frequently a kink of the polymer chain is observed at half contour length, which can be explained by the presence of a short flexible polymer bridging the equally sized DNA blocks. In the case of triblock copolymers with a nucleic acid block of 225 bp a mean length of 171 ± 13 nm was calculated which results in a rise per bp of 0.35 ± 0.03 nm. The height of the molecules was ~2 nm and was in agreement with the diameter of ds DNA. The width was 6~8 nm, larger than the diameter of dsDNA. The broadened width is attributed to the broadening effect of the AFM tip.[86]
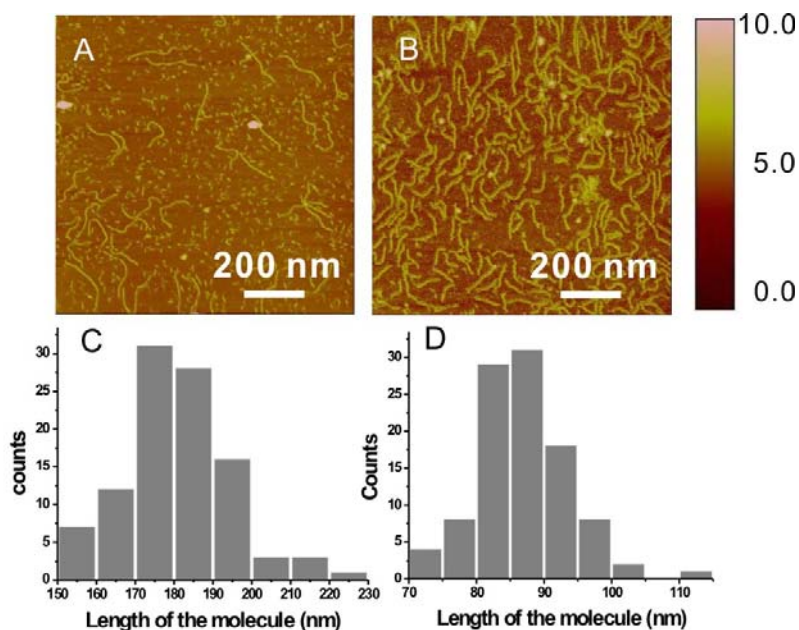
Figure 5.3 *Structural properties of 500 bp-DNA (A, C) and 225 bp-DNA (B, D) fragments investigated by AFM. (A, B) Tapping mode AFM topographical images in buffer. The height is indicated with a color scale bar on the right. The z-scale of the images is 10 nm. (C, D) Histograms of contour length distribution.*

Control experiments with pristine dsDNA of 225 bp and 500 bp showed only single DNA fragments of stretched polymer chains as expected for a semiflexible polymer with a persistence length of 50 nm.[87] Kinks within these structures were not observed. A mean length of 180.1 ± 11.1 nm was measured for the 500-bp fragments, yielding a rise of 0.36 ± 0.02 nm per bp, and a mean length of 86.3 ± 5.7 nm was measured for the 225-bp fragments, yielding a rise of 0.38 ± 0.03 nm.

Besides the broadening effect produced by the AFM tip, thermal drift may also be a reason for the elongation of molecules in the images, because images were usually recorded soon after sample preparation and drift or piezo hysteresis may introduce errors in topography analysis.

5.2 Net-like DNA block copolymer

Sascha Keller and coworkers in University of Konstanz constructed three-dimensional DNA-based networks that could be generated and amplified by the PCR for the first time. The approach was based on the combination of covalently connected branched Y-motifs that act as primer strands in PCR (Fig. 5.4).[88]
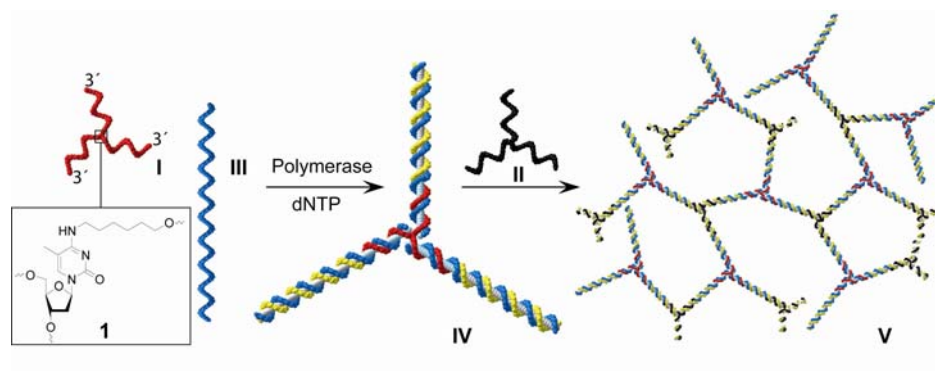
Figure 5.4 *Schematic representation of the generation of DNA network by polymerase chain reaction.*

The approach to develop PCR-amplifiable three-dimensional DNA networks was based on branched sense (I) and reversed primer (II) strands and suitable templates that were designed to be used by both primers for amplification (Fig. 5.4). The branch primer strands were synthesized using the branch point 1 and phosphoramidites for standard 3'→5' synthesis as well as those for 5'→3' synthesis allowing all branches to have the same sequence and to terminate with a free 3'-OH required for processing by DNA polymerases. In the first step of the approach, the branched primer I was expected to anneal with the template III and being extended by a DNA polymerase in the presence of all four dNTPs to an enlarged Y-motif IV (Fig. 5.4). IV harbors binding sites for the second branched primer II required for amplifications by PCR. At the beginning of the next PCR cycle, the denaturing step separateed IV and opened a

location for I and II to anneal. At this step, all ends beard branched primers that allow the formation and growth of DNA networks V by the PCR.
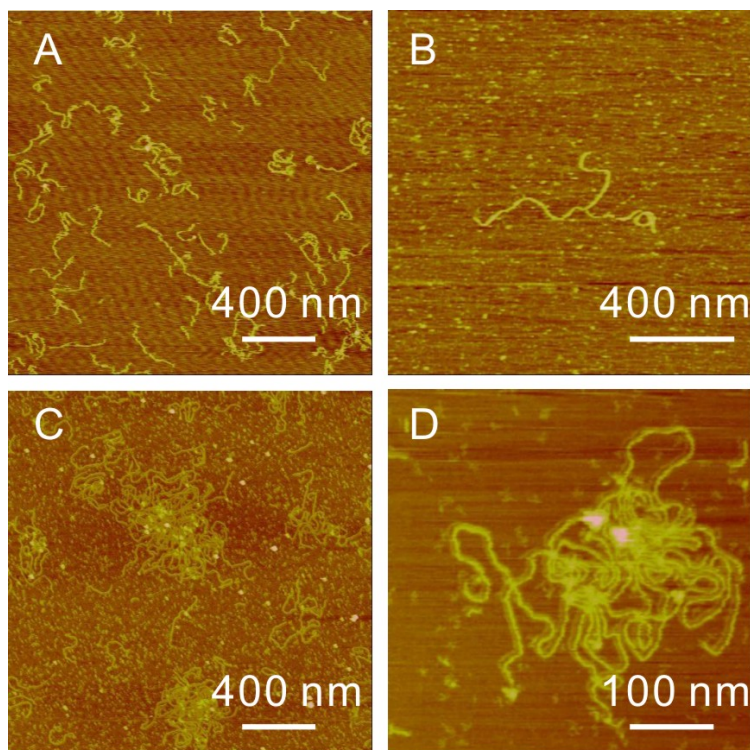
Figure 5.5 *AFM analysis of DNA structures. (A) Structures occurring resulting from non-branched primers; (B) first cycle-reaction product using Ib and IIb; (C) DNA networks generated after 40 PCR cycles; (D)DNA-networks at higher resolution. The lateral scales of the images are indicated in the pictures, and the height scale for each image is 5 nm.*

I imaged the primers and networks in liquid on a mica surface by AFM operated in soft tapping mode. As a control, standard linear primer strands used in PCR were investigated (Fig. 5.5 A). Linear primer strands are considerably flexible resulting in linear or coiled structures having a height ranging from 1.3-1.8 nm and having a width of about 15 nm. The deviation in height compared to the theoretic diameter of dsDNA (2 nm) is attributed to the force of the scanning tip and the surface resulting in flattened object. [89] The increased width is given by the broadening effect of the finite

size of the AFM tip.[90] For branched primer strands I and II, I found extended branched primer strands that were formed after the first cycle of amplification, confirming the formation of the DNA structure IV during the formation of DNA networks (Fig. 5.5 B). The lengths of each of the three DNA branches are consistent with the expected value which is approximately 370 nm. Finally, further AFM investigations show the formation of DNA networks in variable shapes. These irregular shapes may be caused by the collapse of the three-dimensional structure resulted from the interaction with the mica surface. Nevertheless, the AFM visualization of DNA networks on the mica surface verified the capability of the developed method.

Chapter 6

Summary and outlook

The enzymatic reaction of DNA-*b*-PPO micelles with TdT enzymes and dTTP mononucleotides were carried out in both ex-situ and in-situ experiments. AFM, FCS, and PAGE measurements were performed to analyze the size of micelles in ex-situ experiments, and all of these techniques proved the growth of micelles.   After 16 h of reaction, the height of micelles increased from 4.9 ± 1.1 nm to 11.2 ± 1.9 nm, determined from statistical analysis of micelles measured by AFM. By comparing with DNA-*b*-PPO molecular weight standards, on average 62 ± 11 dTTP mononucleotides were added to each molecule.

Then the enzymatic growth of micelles was investigated in-situ with AFM. It was revealed that the growth of micelles could be initiated by adding dTTP mononucleotides to the reaction solution or by adjusting the reaction temperature to 37 °C. The arrangements, heights, and lateral sizes of individual micelles were also followed upon growth. Statistical analysis revealed that in both cases the height of micelles saturated (6-8 nm) after about 1 h. In contrast, micelles that were grown in solution, i.e., in the absence of a mica surface, showed no saturation effect within the same reaction time. The comparison between ex-situ and in-situ growth behavior of the same micelle system allowed us to attribute the saturation effect to the DNA-surface interaction and the reduced exchange of DNA-b-PPO molecules within the micelles and in the buffer solution. A geometrical model that considered the tip radius of curvature was developed in order to extract the number of nucleotides added by the catalytic reaction. In addition, the study of enzymatic growth of DNA-*b*-PPO micelles on mica extended the limit of enzymatic fabrication of DNA nanostructures from 100 nm[50] down to a structural size of 10 nm. My studies supported the

observation of the trend that the growth and height of DNA structures were determined by lateral size of DNA objects.[50]

The structural properties of the micelles in both ex-situ and in-situ enzymatic reactions obtained from different methods were summarized in Table. 6.1. Clearly, the enzymatic reaction of DNA-*b*-PPO micelles with TdT enzymes and dTTP mononucleotides allowed precise controlling the size of micelles.

Ex-situ				In-situ		
t (min)	h_{max} [a] (nm)	T segment added[b]	diameter [c] (nm)	t (min)	h_{max} [d] (nm)	T segment added[e]
0	4.9 ± 1.1	-	9.6 ± 0.9	0	4.7 ± 0.8	2
15	5.1 ± 1.4	6 ± 4	9.9 ± 1.1	18	5 ± 1.3	10
30	5.2 ± 1.3	11 ± 3	10.8 ± 1.6	27	5.3 ± 1.3	23
60	6.6 ± 1.4	22 ± 5	12.4 ± 0.8	36	6.2 ± 1.3	27
180	7.2 ± 1.5	35 ± 8	13.7 ± 1.3	45	7.3 ± 1.1	30
300	8.3 ± 1.6	43 ± 7	17.5 ± 1.4	54	8.2 ± 1.5	37
960	11.2 ± 1.9	62 ± 11	23.0 ± 0.8	63	7.9 ± 1.2	42

Table 6.1 *The height of micelles, diameter of micelles, and the number of added T segment in ex-situ and in-situ enzymatic reactions. [a] derived from ex-situ AFM measurements, [b] determined by PAGE, [c] measured from FCS experiments, [d] derived from in-situ AFM measurements, [e] estimated from the geometrical model*

Based on the amphiphilic property of DNA-*b*-PPO, I investigated a macroscopic DNA machine which could convert the free energy released during hybridization to linear mechanical motion at a centimeter magnitude. The hybridization occurred between DNA-*b*-PPO and comDNA strands at the air-water interface of a film

balance (Langmuir trough). For introducing comDNA strands into the Langmuir trough, a subphase exchange system was used. I demonstrated that the hybridization of DNA-*b*-PPO with complementary sequences induced a change (3.7 mN/m after 19 h) in the lateral pressure. The work the monolayer did to the barriers in the expanding process was estimated to be 4.13% of the energy released because of hybridization, if all DNA segments in the monolayer hybridized with comDNA strands. The work transduced by the monolayer was directly visualized by setting the feedback system of the Langmuir film balance to maintain a lateral pressure of 0.2 mN/m during the subphase exchange process. Each barrier moved 56 mm after 30 min.

Control experiments revealed that the concept of a macroscopic DNA machine based on hybridization was feasible when the monolayer was compressed to the takeoff area. In this case, introducing of comDNA sequences into the subphase resulted in a significant increase of lateral pressure, whereas introducing of noncomDNA did not induce a lateral pressure change.

According to above findings, the idea of a reversible macroscopic DNA motor might be realized in the future. The principle of such a motor is shown in Fig. 6.2.
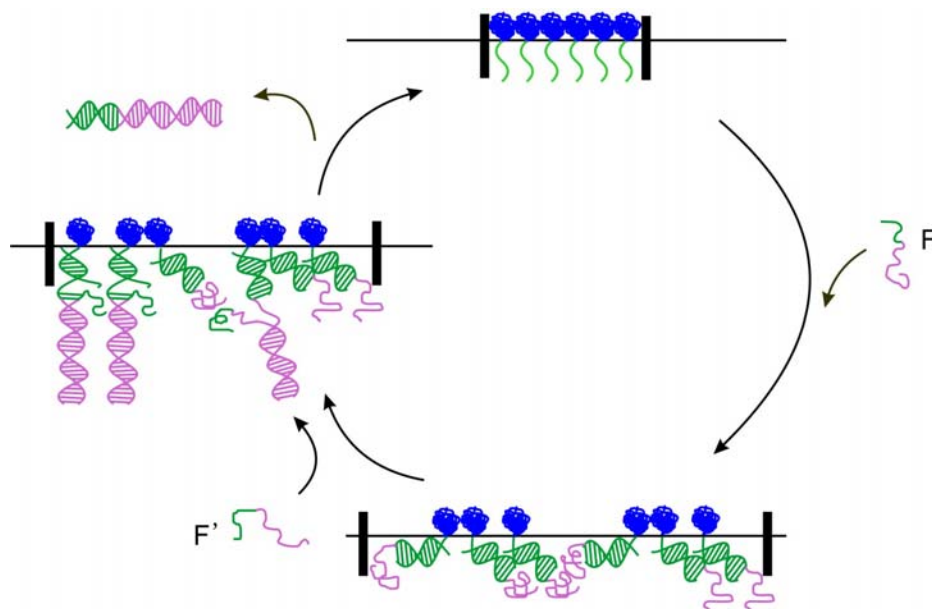
Figure 6.2 *The schematic cartoon of a reversible macroscopic DNA motor. Fuel strands* **F** *hybridize with ssDNA segments of DNA-b-PPO at the air-water interface in the Langmuir trough.* *F' strands hybridize with the overhang section of* **F** *to remove* **F** *from the monolayer, so that the original state of the motor can be recovered.*

List of publications

- **J. Wang**, F. E. Alemdaroglu, A. Herrmann, R. Berger. Enzymatic Control of DNA-*b*-PPO Diblockcopolymer Micelles Directly Observed by Atomic Force Microscopy. *Macromolecules*, 2008, 41, 2914-2919.

- **J. Wang**, F. E. Alemdaroglu, M. Kwak, A. Herrmann, R. Berger. A Macroscopic DNA Machine Made of DNA Block Copolymer. In preparation.

- F. E. Alemdaroglu, **J. Wang**, M. Börsch , R. Berger, A. Herrmann. Controlling the Size of Nanoparticles by Enzymatic Reaction. *Angew. Chem. Int. Ed.*, 2008, 47, 974-976.

- S. Keller, **J. Wang**, M. Chandra, R. Berger, A. Marx. DNA polymerase catalyzed DNA network growth. *J. Am. Chem. Soc.*, accepted.

- F. E. Alemdaroglu, S. Meryem, **J. Wang**, R. Berger, A. Herrmann. DNA Multiblock Copolymers. *Chem. Commun.*, 2007, 1359, 1358-1359.

- F. E. Alemdaroglu, W. Zhuang, L. Zöphel, **J. Wang**, R. Berger, J. P. Rabe, A. Herrmann. Generation of Multiblock Copolymers by PCR: Synthesis, Visualization and Nanomechanical Properties. *Nano Lett.*, accepted.

References

1.   Jeong, J. H.; Park, T. G., Novel polymer-DNA hybrid polymeric micelles composed of hydrophobic poly(D,L-lactic-co-glycolic acid) and hydrophilic oligonucleotides. *Bioconjugate Chem.* **2001,** 12, 917-923.

2.   Jeong, J. H.; Kim, S. W.; Park, T. G., Novel intracellular delivery system of antisense oligonucleotide by self-assembled hybrid micelles composed of DNA/PEG conjugate and cationic fusogenic peptide. *Bioconjugate Chem.* **2003,** 14, 473-479.

3.   Costioli, M. D.; Fisch, I.; Garret-Flaudy, F.; Hilbrig, F.; Freitag, R., DNA purification by triple-helix affinity precipitation. *Biotechnol. Bioeng.* **2003,** 81, 535-545.

4.   Li, Z.; Zhang, Y.; Fullhart, P.; Mirkin, C. A., Reversible and chemically programmable micelle assembly with DNA block-copolymer amphiphiles. *Nano Lett.* **2004,** 4, 1055-1058.

5.   Alemdaroglu, F. E.; Ding, K.; Berger, R.; Herrmann, A., DNA-templated synthesis in three dimensions: Introducing a micellar scaffold for organic reactions. *Angew. Chem. Int. Ed.* **2006,** 45, 4206-4210.

6.   Alemdaroglu, F. E.; Herrmann, A., DNA meets synthetic polymer-highly versatile hybrid materials. *Org. Biomol. Chem.* **2007,** 5, 1311-1320.

7.   Miller, D. W.; Batrakova, E. V.; Waltner, T. O.; Alakhov, V. Y.; Kabanov, A. V., Interactions of pluronic block copolymers with brain microvessel endothelial cells: Evidence of two potential pathways for drug absorption. *J. Bioconjugate Chem.* **1997,** 8, 649-657.

8.   Alemdaroglu, F. E.; Alemdaroglu, N. C.; Langguth, P.; Herrmann, A., DNA block copolymer micelles-A combinatorial tool for cancer nanotechnology. *Adv. Mater.* **2008,** 20, 899-902.

9.   Fowler, J. D.; Suo, Z., Biochemical, structural, and physiological characterization of terminal deoxynucleotidyl transferase. *Chem. Rev.* **2006,** 106, 2092-2110.

10. Delarue, M.; Boule, J. B.; Lescar, J.; Expert-Bezancon, N.; Jourdan, N.; Sukumar, N.; Rougeon, F.; Papanicolaou, C., Crystal structures of a template-independent DNA

polymerase: murine termial deoxynucleotidyltransferase. *The EMBO Journal* **2002,** 21, (3), 427-439.

11. Bollum, F. J., *Terminal deoxynucleotidy transferase.* 3rd ed.; Academic Press: New York, 1974; 'Vol.' 10, p 145-171.

12. Alemdaroglu, F. E.; Wang, J.; Börsch, M.; Berger, R.; Herrmann, A., Controlling the size of nanoparticles by enzymatic reaction. *Angw. Chem.Int. Ed.* **2008,** 47, 974-976.

13. Hansma, H. G., Surface biology of DNA by atomic force microscopy. *Annu. Rev. Phys. Chem.* **2001,** 52, 71-92.

14. Pothemund, P. W. K., Folding DNA to create nanoscale shapes and patterns. *Nature* **2006,** 440, 297-302.

15. Severin, N.; Zhuang, W.; Ecker, C.; Kalachev, A. A.; Sokolov, I. M.; Rabe, J. P., Blowing DNA Bubbles. *Nano Lett.* **2006,** 6, 2561-2566.

16. Bezanilla, M.; Drake, B.; Nudler, E.; Kashlev, M.; Hansma, P. K.; Hansma, H. G., Motion and enzymatic degradation of DNA in the atomic force microscope. *Biophys. J.* **1994,** 67, 2454-2459.

17. Kasas, S.; Thomson, N. H.; Smith, B. L.; Hansma, H. G.; Zhu, X.; Guthold, M.; Bustamante, C.; Kool, E. T.; Kashlev, M.; Hansma, P. K., Escherichia coli RNA polymerase activity observed using atomic force microscopy. *Biochemistry* **1997,** 36, 461-468.

18. Ellis, D. J.; Dryden, D. T. F.; Berge, T.; Edwardson, J. M.; Henderson, R. M., Direct observation of DNA translocation and cleavage by the EcoKI endonuclease using atomic force microscopy. *Nat. Struct. Biol.* **1999,** 6, (1), 15-17.

19. Wang, J.; Alemdaroglu, F. E.; Prusty, D. K.; Herrmann, A.; Berger, R., In-situ visualization of the enzymatic growth of surface-immobilized DNA blockcopolymer micelles by atomic force microscopy. *Macromolecules* **2008,** 41, 2914-2919.

20. SantaLucia, J. J., A unified view of polymer, dumbbell, and oligonucleotide DNA nearest neighbor thermodynamics. *Proc. Natl Acad. Sci. USA* **1998,** 95, 1460-1465.

21. Yurke, B.; Turberfild, A. J.; Mills Jr, A. P.; Simmel, F. C.; Neumann, J. L., A DNA-fuelled molecular machine made of DNA. *Nature* **2000,** 406, 605-608.

22. Turberfield, A. J.; Mitchell, J. C.; Yurke, B.; Mills Jr, A. P.; Blakey, M. I.; Simmel, F. C., DNA fuel for free-running nanomachines. *Phys. Rev. Lett.* **2003,** 90, 118102.

23. Yan, H.; Zhang, X.; Shen, Z.; Seeman, N. C., A robust DNA mechanical device controlled by hybridization topology. *Nature* **2002,** 415, 62-65.

24. Sherman, W. B.; Seeman, N. C., A precisely controlled DNA biped walking device. *Nano Lett.* **2004,** 4, 1203-1207.

25. Shin, J. S.; Pierce, N. A., A synthetic DNA walker for molecular transport. *J. Am. Chem. Soc.* **2004,** 126, 10834-10835.

26. Yin, P.; Yan, H.; Daniell, X. G.; Turberfield, A. J.; Reif, J. H., A unidirectional DNA walker that moves autonomously along a track. *Angew. Chem. Int. Ed.* **2004,** 43, 4906-4911.

27. Bath, J.; Green, S. J.; Turberfield, A. J., A free-running DNA motor powered by a nicking enzyme. *Angew. Chem. Int. Ed.* **2005,** 44, 4358-4361.

28. Tian, Y.; He, Y.; Chen, Y.; Yin, P.; Mao, C. D., Molecular devices - A DNAzyme that walks processively and autonomously along a one-dimensional track. *Angew. Chem. Int. Ed.* **2005,** 44, 4355-4358.

29. Ramakrishnan, V.; D'Costa, M.; Ganesh, K. N.; Safak, M., PNA-DNA hybridization at the air-water interface in the presence of octadecylamine Langmuir monolayers. *Langmuir* **2002,** 18, 6307-6311.

30. Ramakrishnan, V.; D'Costa, M.; Ganesh, K. N.; Sastry, M., Effect of salt on the hybridization of DNA by sequential immobiliztion of oligonucleotides at the air-water interface int eh presence of ODA/DOTAP monolayers. *Journal of Colloid and Interface Science* **2004,** 276, 77-84.

31. Erokhina, S.; Berzina, T.; Cristofolini, L.; Konovalov, O.; Erokhin, V.; Fontana, M. P., Interaction of DNA oligomers with cationic lipidic monolayers: compexation and splitting. *Langmuir* **2007,** 23, 4414-4420.

32. Dai, S.; Zhang, X.; Du, Z.; Dang, H., Fabrication of nanopatterned DNA films by Langmuir-Blodegtt technique. *Materials Letters* **2005,** 59, 423-429.

33. Binnig, G.; Rohrer, H.; Gerber, C.; Weible, E., Surface studies by scanning tunneling microscopy. *Phys. Rev. Lett.* **1982,** 49, 57-61.

34. Binnig, G.; Quate, C. F.; C., G., Atomic force microscope. *Phys. Rev. Lett.* **1986,** 56, 930-933.

35. Colton, R. J.; Baselt, D. R.; Dufrene, Y. F.; Green, J. B. D.; Lee, G. U., Scanning probe microscopy. *Current Opinion in Chemical Biology* **1997,** 1, (3), 370-377.

36. Magde, D.; Elson, E. L.; Webb, W. W., Thermodynamic fluctuations in a reacting system: Measurement by fluorescence correlation spectroscopy. *Phys. Rev. Lett.* **1972,** 29, 705-708.

37. Hess, S. T.; Huang, S. H.; Heikal, A. A.; Webb, W. W., Biological and chemical applications of fluorescence correlation spectroscopy: A review. *Biochemistry* **2002,** 41, (3), 697-705.

38. Koynov, K.; Mihov, G.; Mondeshki, M.; Moon, C.; Spiess, H. W.; Muellen, K.; Butt, H.-J., Diffusion and conformation of peptide-functionalized polyphenylene dendrimers studied by fluorescence correlation and ^{13}C NMR Spectroscopy. *Biomacromolecules* **2007,** 8, 1745-1750.

39. Tirado, M. M.; Garcia de la torre, J., Rotational dynamics of rigid, symmetric top macromolecules. Application to circular cylinders. *J. Chem. Phys.* **1980,** 73, 1986-1993.

40. Berland, K. M., Detection of specific DNA sequences using dual-color two-photon fluorescence correlation spectroscopy. *Journal of Biotechnology* **2004,** 108, (2), 127-136.

41. Düser, M. G.; Zarrabi, N.; Bi, Y.; Zimmermann, B.; Dunn, S. D.; Börsch, M., *Proc.SPIE-Int. Soc. Opt. Eng.* **2006,** 6092, 60920H.

42. Borsch, M.; Turina, P.; Eggeling, C.; Fries, J. R.; Seidel, C. A. M.; Labahn, A.; Graber, P., *FEBS Lett.* **1998,** 437, (3), 251-254.

43. Porter, G.; Sadkowski, P. J.; Tredwell, C. J., *Chem. Phys. Lett.* **1977,** 49, (3), 416-420.

44. Roberts, G., *Langmui-Blodgett films*. Plenum Press: New York, 1990.

45. Pockels, A., On the relative contamination of the water-surface by equal quantities of different substances. *Nature* **1892,** 46, (1192), 418-419.

46. Rayleigh, L., Surface Tension. *Nature* **1891,** XLIII, 437-439.

47. Langmuir, I., The constitution and fundamental properties of solids and liquids.II. Liquids. *J. Am. chem. Soc.* **1917,** 39, 1848-1906.

48. Blodgett, K. B., Films built by depositing successive monomolecular layers on a solid surface. *J. Am. Chem. Soc.* **1935,** 57, 1007-1022.

49. Butt, H.-J.; Graf, K.; Kappl, M., *Physics and Chemistry of Interfaces.* Wiley-VCH: Berlin, 2003.

50. Chow, D. C.; Lee, W. K.; Zauscher, S.; Chilkoti, A., Enzymatic fabrication of DNA nanostructures: extension of a self-assembled oligonucleotide monolayer on gold arrays. *J. Am. Chem. Soc.* **2005,** 127, 14122-14123.

51. Mandelkern, M.; Elias, J. G.; Eden, D.; Crothers, D. M., The dimensions of DNA in solution. *J. Mol. Biol.* **1981,** 152, 153-161.

52. Mortensen, K., Structural studies of aqueous solutions of PEO-PPO-PEO triblock copolymers, their micellar aggregates and mesophases; a small-angle neutron scattering study. *J. Phys.* **1996,** A, 103-124.

53. Alemdaroglu, F. E. DNA block copolymers-synthesis, morphologies and applications. Johannes Gutenberg University, Mainz, 2007.

54. Glass, R.; Moller, M.; Spatz, J. P., Block copolymer micelle nanolithography. *Nanotechnology* **2003,** 14, 1153-1160.

55. Lee, W.-K.; Patra, M.; Linse, P.; Zauscher, S., Scaling behavior of nanopatterned polymer brushes. *Small* **2007,** 3, (1), 63-66.

56. Dormidontova, E. E., Micellization kinetics in block copolymer solutions: scaling model. *Macromolecules* **1999,** 32, 7630-7644.

57. Nyrkova, I. A.; Semenov, A. N., On the theory of micellization kinetics. *Macromol. Theory. Simul.* **2005,** 14, 569-585.

58. Malmsten, M.; Lindman, B., Self-assembly in aqueous block copolymer solutions. *Macromolecules* **1992,** 25, 5440-5445.

59. Smith, S. B.; Cui, Y.; Bustamante, C., Overstretching B-DNA: the elastic response of individual double-stranded and single-stranded DNA molecules. *Science* **1996,** 271, 795-799.

60. Rivetti, C.; Walker, C.; Bustamante, C., Polymer chain statistics and conformational analysis of DNA molecules with bends or sections of different flexibility. *J. Mol. Biol.* **1998,** 280, 41-59.

61. Tinland, B.; Pluen, A.; Sturm, J.; Weill, G., Persistence length of single-stranded DNA. *Macromolecules* **1997,** 30, 5763-5765.

62. David, I. B., *An introduction to polymer physics*. 1st ed.; Cambridge University Press: Cambridge, United Kingdom, 2002, p 72-76.

63. Murphy, M. C.; Rasnik, I.; Cheng, W.; Lohman, T. M.; Ha, T., Probing single-stranded DNA conformational flexibility using fluorescence spectroscopy. *Biophys. J.* **2004,** 86, 2530-2537.

64. Olson, W. K., Configurational statistics of polynucleotide chains: a single virtual bond treatment. *Macromolecules* **1975,** 8, 272-275.

65. Aharoni, S. M., On entanglements of flexible and rodlike polymers. *Macromolecules* **1983,** 16, 1722-1728.

66. Pedersen, J. S.; Gerstenberg, M. C., Scattering form factor of block copolymer micelles. *Macromolecules* **1996,** 29, 1363-1365.

67. Wang, J.; Alemdaroglu, F. E.; Prusty, D. K.; Herrmann, A.; Berger, R., In-situ visualization of the enzymatic growth of surface-immobilized DNA block copolymer micelles by scanning force microscopy. *Macromolecules* **2008,** 41, 2914-2919.

68. Zhou, J.; Gregurick, S. K.; Krueger, S.; Schwarz, F. P., Conformational changes in single-strand DNA as a function of temperature by SANS. *Biophys. Ja.* **2006,** 90, 544-551.

69. Lehmler, H. J.; Bummer, P. M., Behavior of 10-(perfluorohexyl)-decanol, a partially fluorinated analog of hexadecanol, at the air–water interface. *Journal of Fluorine Chemsitry* **2002,** 117, (1), 17-22.

70. Constantino, C. J. L.; Dhanabalan, A.; N., O. J. O., Experimental artifacts in the surface pressure measurement for lignin monolayers in Langmuir troughs. *Review of Scientific Instruments* **1999,** 70, 3674-3680.

71. Smith, S. B.; Finzi, L.; Butstamante, C., Direct mechanical measurements of the elasticity of single DNA groups by magnetic beads. *Science* **1992,** 258, 1122-1126.

72. Manning, G. S., A procedure for extracting persistence lengths from light-scattering data on intermediate molecular weight DNA. *Biopolymers* **1981,** 20, 1751-1755.

73. Mandelkern, M.; Elias, J. G.; Eden, D.; Crothers, D. M., The dimensions of DNA in solution. *J. Mol. Biol.* **1981,** 152, 153-161.

74. Sastry, M.; Ramakrishnan, V.; Pattarkine, M.; Gole, A.; Ganesh, K. N., Hybridization of DNA by sequential immobilization of oligonucleotides at the air-water interface. *Langmuir* **2000,** 16, 9142-9146.

75. Cox, J. K.; Yu, K.; Constantine, B.; Eisenberg, A.; Lennox, R. B., Polystyrene-poly(ethylene oxide) diblock copolymers form well-defined surface aggregates at the air/water interface. *Langmuir* **1999,** 15, (22), 7714-7718.

76. Chernoff, D. A., High resolution chemical mapping using tapping mode AFM with phase contrast, in: Proceedings microscopy and microanalysis. **1995**, 888-889.

77. Li, H.; Liu, Q.; Qin, L.; Xu, M.; Lin, X.; Yin, S.; Wu, L.; Su, Z.; Shen, J., Self-assembling structures and thin-film microscopic morhologies of amphilphilic rod-coil block oligomers. *J. Col. Int. Sci.* **2005,** 289, 488-497.

78. Leclere, P.; Lazzaroni, R.; Bredas, J. L.; Yu, J. M.; Dubois, P.; Jerome, R., Microdomain morphology analysis of block copolymers by atomic force microscopy with phase detection imaging. *Langmuir* **1996,** 12, (18), 4317-4320.

79. Tamayo, J.; Garcia, R., Deformation, contact time, and phase contrast in tapping mode scanning force microscopy. *Langmuir* **1996,** 12, (18), 4430-4435.

80. GarciaParajo, M.; Longo, C.; Servat, J.; Gorostiza, P.; Sanz, F., Nanotribological properties of octadecyltrichlorosilane self-assembled ultrathin films studied by atomic force microscopy: Contact and tapping modes. *Langmuir* **1997,** 13, (8), 2333-2339.

81. Kopp-Marsaudon, S.; Leclere, P.; Dubourg, F.; Lazzaroni, R.; Aime, J. P., Quantitative measurement of the mechanical contribution to tapping-mode atomic force microscopy images of soft materials. *Langmuir* **2000,** 16, (22), 8432-8437.

82. Rose, F.; Martin, P.; Fujita, H.; Kawakatsu, H., Adsorption and combing of DN aon HOPG surfaces of bulk crystals and nanosheets: application to the bridging of DNA between HOPG/Si heterostructures. *Nanotechnology* **2006,** 17, 3325-3332.

83. Yang, C. W.; Hwang, I. S.; Chen, Y. F.; Chang, C. S.; Tsai, D. P., Imaging of soft matter with tapping-mode atomic force microscopy and non-contact-mode atomic force microscopy. *Nanotechnology* **2007,** 18, 084009.

84. Alemdaroglu, F. E.; Zhuang, W.; Zoephel, L.; Wang, J.; Berger, R.; Rabe, J. P.; Herrmann, A., Generation of multiblock copolymers by PCR: synthesis, visualization and nanomechanical properties. *Nano Lett.* Accepted.

85. Ulyanov, N. B.; James, T. L., *Methods Enzymol.* **1995,** 261, 90-120.

86. Bustamante, C.; Keller, D.; Yang, G., *Curr. Opin. Struct. Biol.* **1993,** 3, 363-372.

87. Rivetti, C.; Guthold, M.; Bustamante, C., Scanning force microscopy of DNA deposited onto mica: Equilibration versus kinetic trapping studied by statistical polymer chain analysis. *J. Mol. Biol.* **1996,** 264, 919-932.

88. Keller, S.; Wang, J.; Chandra, M.; Berger, R.; Marx, A., DNA polymerase catalyzed DNA network growth. *J. Am. Chem. Soc.* In press.

89. Magonova, S. N.; Elingsa, V.; Whangbo, M.-H., Phase imaging and stiffness in tapping-mode atomic force microscopy. *Surface science* **1997,** 375, L385-L391.

90. Bustamante, C.; Keller, D.; Yang, G., Scanning force microscopy of nucleic acids and nucleoprotein assemblies. *Curr. Opin. Struct. Biol.* **1993,** 3, 363-372.

Curriculum Vitae

Personal Details

First name: Jie

Last name: Wang

Gender: Female

Date of birth: 25. Apr. 1982

Place of birth: Jiangxi, China

Address: Ackermannweg 10, D-55128 Mainz, Germany

E-mail: wangjie@mpip-mainz.mpg.de

Education

- **PhD**   Oct. 2005 – Oct. 2008: "DNA block copolymers-from micelles to machines" under the supervision of Prof. Dr. Hans-Jürgen Butt and Dr. Rüdiger Berger, Max Planck Institute for Polymer Research, Mainz, Germany

- **Master's thesis**   Apr. 2005 - Sep. 2005: "Analysis of dialkyldisulfide monolayers on gold by atomic force microscopy" under the supervision of Prof. Dr. Hans-Jürgen Butt and Dr. Rüdiger Berger, Max Planck Institute for Polymer Research, Mainz, Germany

- **Internship**   Oct. 2004 – Apr. 2005: "Surface nanostructuring on uniaxially stretched and extruded polystyrene by air plasma treatment and swelling" under the supervision of Prof. Dr. Hans-Jürgen Butt and Dr. Karlheinz Graf, Max Planck Institute for Polymer Research, Mainz,

Germany

- **M.Sc. in Chemistry**   Oct. 2003 – Oct. 2004: International Master course in Chemistry-Biology Department of Siegen University, Siegen, Germany

- **B.Sc. in Chemistry**   Sep. 1999-Jul. 2003: Beijing Normal University, Beijing, China